RES TERRAE

Publications in Geosciences, University of Oulu
Oulun yliopiston geotieteiden julkaisuja

Ser. A, No. 54
2026

Marco Arrieta

An integrated geotechnical framework for coarse mine waste dumps - Connecting field-scale gradation, stress-dependent shear-strength, and flow-slide mobility

$$m = \frac{D}{3}$$

Marco Arrieta

An integrated geotechnical framework for coarse mine waste dumps - Connecting field-scale gradation, stress-dependent shear-strength, and flow-slide mobility

Res Terrae, Ser. A, No. 54, OULU, 2026

RES TERRAE - Publications in Geosciences, University of Oulu, Oulun yliopiston geotieteiden julkaisuja

Ser. A, Contributions, Ser. B, Raportteja - Reports, Ser. C, Opetusjulkaisuja - Teaching material

Ser. A	ISSN 0358-2477 (print)
Ser. A	ISSN 2489-7957 (online)
Ser. B	ISSN 0358-2485 (print)
Ser. B	ISSN 2736-9552 (online)
Ser. C	ISSN 0358-2493 (print)
Ser. A, No. 54	ISBN 978-952-62-5024-3 (print)
Ser. A, No. 54	ISBN 978-952-62-5025-0 (online)

Julkaisu ja levitys - Published and distributed by:
Oulu Mining School
P.O. Box 3000, 90014 University of Oulu, Finland

E-mail: kirsi.luolavirta@oulu.fi
www: http://www.oulu.fi/resterr/

Cover Figure:
From particle-size distribution to stress-dependent shear strength.

Marco Arrieta

An integrated geotechnical framework for coarse mine waste dumps - Connecting field-scale gradation, stress-dependent shear-strength, and flow-slide mobility

Academic dissertation to be presented with the assent of the Doctoral Programme Committee of Technology and Natural Sciences of the University of Oulu for public defence in Lecture Hall L5, University of Oulu, on 26 August 2026, at 10:00 am.

UNIVERSITY OF OULU, OULU 2026

Supervised by

Professor Zongxian Zhang,
Oulu Mining School, University of Oulu

Reviewed by

Assistant Professor Lauri Uotinen,
Aalto University

Associate Professor Hossein Masoumi
Monash University

Opponent

Professor David Saiang
Luleå University of Technology

ABSTRACT

Coarse mine waste dumps are governed by a chain of coupled geotechnical problems that spans material-state characterization, pre-failure resistance representation, and post-failure mobility assessment. In current practice, these components are commonly treated separately, weakening the connection between measurable field conditions, defensible shear-strength representation, and failure consequence evaluation. This thesis develops an integrated geotechnical framework for coarse mine waste dumps by connecting field-scale gradation, stress-dependent shear strength, and flow-slide mobility.

1. First, an unmanned aerial vehicle (UAV) based photogrammetric workflow is developed to estimate particle size distribution (PSD) at field scale in coarse waste-rock systems where conventional sieving is impractical. The approach combines aerial image acquisition, Structure-from-Motion reconstruction, area discretization, digital fragmentation analysis, and validation against field measurements, thereby establishing gradation as an operational field-scale descriptor for geotechnical characterization.
2. Second, pre-shear PSD information is used to constrain the curvature of nonlinear stress-dependent shear-strength envelopes within an existing power-law framework. Instead of fitting curvature freely from triaxial data alone, the proposed approach regularizes curvature using PSD scaling and retains only the strength level for calibration, reducing arbitrariness and strengthening the physical interpretability of the resistance model.
3. Third, post-failure mobility of high-end waste dump flow slides is assessed through the coupled influence of basal friction, pore pressure, turbulence, and path geometry. A screening-level mechanics framework is developed by combining sliding-block concepts, Bishop pore-pressure formulation, Voellmy-type dynamic resistance, path confinement, and a Brachistochrone-based frictionless benchmark to interpret runout and velocity.

The results show that field-scale gradation can be obtained with engineering-grade accuracy using UAV photogrammetry, that pre-shear PSD can be elevated from a descriptive variable to a calibration constraint in nonlinear shear-strength modeling, and that high to extreme mobility is governed by the interaction of reduced basal resistance, elevated pore pressure, and confined travel paths.

This thesis does not propose a universal constitutive law or a single end-to-end predictive model. Its contribution is the development of a coherent field-to-consequence framework that links measurable material state, pre-failure shear-strength characterization, and post-failure mobility assessment for coarse mine waste systems.

To the love of my life, without whom everything is grey. The light, the possibilities, and who one can become exist because you are here. The sky is the limit, and all begins with you…Yero!

ACKNOWLEDGEMENTS

I am deeply grateful to all who contributed to this doctoral journey. To the giants on whose shoulders this work stands, Prof. Zong-Xian Zhang and Associate Prof. Adeyemi Aladejare, sincere appreciation is extended for their guidance, mentorship, and continuous support.

Special recognition is given to Prof. Zhang. His belief in the possibility of pursuing a part-time doctoral path alongside a full-time professional role was decisive.

Without that trust, this work would not exist!

His patience, commitment, and steady guidance sustained progress under limited time for writing and research. More than supervision, his ability to spark curiosity, to shape scientific thinking, and to connect ideas into a coherent understanding defined how this work was built.

His mentorship extended beyond technical direction, influencing not only the development of this research, but also the way problems are approached, questioned, and understood.

As *John Archibald Wheeler* framed it, "matter tells spacetime how to curve, and spacetime tells matter how to move." In granular systems, this same reciprocity governs behavior: structure defines how stress is transmitted, and stress reshapes that structure, controlling shear response and mobility.

"All systems follow the same fundamental laws; without that understanding, interpretation remains limited and disconnected from the processes that truly govern behavior"

Use of generative AI. OpenAI ChatGPT was used during preparation and revision of the thesis synopsis for language editing, readability checking, formatting support, and consistency review. The author retained responsibility for the manuscript and verified the scientific content, data selection, analyzes, equations, figures, final text.

NOMENCLATURE AND ABBREVIATIONS

Abbreviations

Abbreviation	Meaning
2D	Two-dimensional
3D	Three-dimensional
DEM	Discrete Element Method
FEM	Finite Element Method
MAE	Mean Absolute Error
MP	Megapixel
PSD	Particle Size Distribution
RGB	Red-Green-Blue
RMSE	Root Mean Square Error
RQ	Research Question
SfM	Structure-from-Motion
UAV	Unmanned Aerial Vehicle
UCS	Uniaxial Compressive Strength
WD	Waste dump

General symbols and statistical terms

Symbol	Meaning	Unit
%	Percentage	%
$Bias$	Mean signed error	MPa, where applied to stress
$Bias_{\tau,fit}$	Bias of the fitted-reference shear-stress route	MPa
$Bias_{\tau,PSD}$	Bias of the PSD-constrained shear-stress route	MPa
$Bias_{\tau,PSD-fit}$	Bias between PSD-constrained and fitted-reference routes	MPa
$\Delta Bias_{\tau}$	Case-wise difference in shear-stress bias	MPa
ΔMAE_{τ}	Case-wise difference in shear-stress MAE	MPa
$\Delta RMSE_{\tau}$	Case-wise difference in shear-stress RMSE	MPa
fit	Subscript denoting the fitted-reference route	---
i	Data-point index	---
N	Number of data points in a fitted case	---
p	Statistical p-value	---
PSD	Subscript denoting the PSD-constrained route	---
ψ	Rank correlation coefficient	---
Std	Standard deviation	variable-dependent

Particle-size, gradation, and material-state symbols

Symbol	Meaning	Unit
d	Particle size used in PSD scaling formulation	mm
d_{10}	Particle size at 10% passing in Section 5 finite-window PSD scaling	mm
d_{90}	Particle size at 90% passing in Section 5 finite-window PSD scaling	mm
d_L	Lower bound of retained PSD fitting window	mm
d_U	Upper bound of retained PSD fitting window	mm
D	Finite-window PSD-scaling descriptor	---
D_{10}	Particle size at 10% passing	mm
D_{30}	Particle size at 30% passing	mm
D_{50}	Median particle size; particle size at 50% passing	mm
D_{60}	Particle size at 60% passing	mm
D_{max}	Maximum particle size	mm
D_S	Triaxial apparatus diameter	mm
DS/D_{max}	Apparatus-to-maximum-particle-size ratio	---
e_i	Initial void ratio	---
Fines	Fines fraction of the material	%
Gravel	Gravel fraction of the material	%
$M \leq d$	Mass finer than particle size d	mass unit
MT	Total mass within the retained PSD window	mass unit
$P \leq d$	Cumulative mass fraction finer than particle size d	---
Sand	Sand fraction of the material	%
s	Fitted log-log PSD slope used to estimate D	---
ρ	Bulk density	kg/m³
σ_c	Intact-rock compressive strength	MPa

Shear-strength resistance symbols

Symbol	Meaning	Unit
A	Generic power-law strength coefficient	variable-dependent
b	Generic power-law curvature exponent	---
$D/3$	Normalized PSD count-scaling descriptor forming the basis of the adopted PSD-to-curvature closure	---
K	Dimensionless strength coefficient in normalized power-law envelope	---
k	Coefficient in referenced fractal-power formulation	variable-dependent
l	Length-scale parameter in referenced fractal-power formulation	variable-dependent
m_{fit}	Fitted curvature exponent	---
m_{PSD}	PSD-assigned curvature exponent	---
p_a	Reference atmospheric pressure used for stress normalization	MPa
R	Equivalent roughness parameter in the Barton-Kjaernsli criterion	---
S	Size-dependent equivalent particle strength in the Barton-Kjaernsli criterion	MPa
S/σ_c	Normalized equivalent particle strength	---
τ	Shear stress	MPa
τ_{fit}	Shear stress from fitted-reference route	MPa
τ_i	Shear stress of data point i	MPa
τ_{PSD}	Shear stress from PSD-constrained route	MPa
φ	Friction angle, general notation	degrees
φ_b	Basic friction angle in the Barton-Kjaernsli criterion	degrees
ϕ_1'	Anchor secant friction angle at reference normal stress σ_n = 10pa	degrees
$\phi_{e=0}'{}'$	Reference friction angle at zero void-ratio	degrees
ϕ	Effective friction angle; use consistently with φ if retained	degrees
ω	Coefficient in the cited anchor-normalized formulation	---
σ_1'	Major effective principal stress	MPa
σ_3'	Minor effective principal stress / effective confining stress	MPa
σ_n	Normal stress	MPa
σ_n'	Effective normal stress	MPa
$\sigma_{n,i}$	Normal stress of data point i	MPa
Δm	Curvature deviation $(m_{PSD} - m_{fit})$	---
$\lvert\Delta m\rvert$	Absolute curvature deviation	---

Error and route-comparison symbols

Symbol	Meaning	Unit
MAE_{fit}	Mean absolute shear-stress error of the fitted-reference route	MPa
$MAE_{\tau,PSD}$	Mean absolute shear-stress error of the PSD-constrained route	MPa
$MAE_{\tau,PSD-fit}$	Mean absolute deviation between PSD-constrained and fitted-reference shear stresses	MPa
$RMSE_{\tau,fit}$	Root mean square shear-stress error of the fitted-reference route	MPa
$RMSE_{\tau,PSD}$	Root mean square shear-stress error of the PSD-constrained route	MPa
$RMSE_{\tau,PSD-fit}$	Root mean square deviation between PSD-constrained and fitted-reference shear stresses	MPa

Flow-slide mobility, pore-pressure, and runout symbols

Symbol	Meaning	Unit
a	Path-confinement coefficient	1/m
B	Bishop pore-pressure coefficient	---
f	Basal friction coefficient	---
H	Fall height or maximum vertical drop	m
L	Runout distance	m
m	Moving mass in sliding-block formulation	kg
r_u	Pore-pressure ratio	---
t	Travel time	s
t_{obs}	Observed travel time	s
t_{opt}	Ideal frictionless reference travel time	s
u	Pore pressure	kPa or MPa
v	Flow velocity	m/s
v_{obs}	Observed flow velocity	m/s
v_{opt}	Ideal frictionless reference velocity	m/s
β	Angle of reach	degrees
δ	Basal-bed slope angle	degrees
η_t	Time ratio	---
η_v	Velocity ratio	---
μ	Pore-pressure	kPa or MPa
ξ	Voellmy-type turbulence coefficient	m/s^2
ρ	Bulk density of moving material	kg/m^3
σ_v	Vertical stress	kPa or MPa
$\Delta\sigma_v$	Vertical stress increment	kPa or MPa
$\Delta\mu$	Pore-pressure increment	kPa or MPa
φ_d	Equivalent dynamic friction angle	degrees

ORIGINAL PUBLICATIONS

1. Paper I: Arrieta, M., and Zhang, Z.-X. (2024). Particle size distribution (PSD) estimation using unmanned aerial vehicle (UAV) photogrammetry for rockfill shear strength characterization. Acta Geotechnica, 19:6239-6258. https://doi.org/10.1007/s11440-024-02315-x.
2. Paper II: Arrieta, M., and Zhang, Z.-X. (2026). Stress-Dependent Shear Strength of Rockfills and Waste-Rock Materials with Curvature Constrained by Particle Size Distribution Scaling. Rock Mechanics and Rock Engineering. Appended manuscript.
3. Paper III: Arrieta, M., and Zhang, Z.-X. (2025). Minimum-Time Path (Brachistochrone) Analysis for Extreme Flow Slide Mobility in High-End Waste Dumps: Integrating Pore Pressure and Dynamic Rheology. https://doi.org/10.1007/s00603-025-05009-2.

Statement of author contribution

This doctoral dissertation is an article-based thesis composed of three appended papers and a thesis synopsis. Marco Arrieta is the first author and principal contributor to all three papers and the sole author of the thesis synopsis. He developed the overarching thesis concept, designed the integrated research framework, carried out the core analyzes, interpreted the results, prepared the figures and tables, and wrote the first complete versions of the manuscripts and the synopsis.

Professor Zong-Xian Zhang contributed through scientific supervision, conceptual discussion, methodological review, validation of the interpretations, and critical revision of the manuscripts.

In Paper I, Marco Arrieta conceived and implemented the UAV-based workflow for field-scale particle-size characterization, carried out the photogrammetric processing and digital fragmentation analysis, performed the validation against field measurements, conducted the geotechnical interpretation using the Barton-Kjaernsli criterion, and drafted the manuscript. Zong-Xian Zhang contributed to scientific guidance, methodological review, interpretation of the results, and manuscript revision.

In Paper II, Marco Arrieta developed the PSD-constrained framework for stress-dependent shear-strength calibration, compiled and structured the literature database, carried out the comparative calibration analysis and error evaluation, interpreted the results, and drafted the manuscript. Zong-Xian Zhang contributed to scientific discussion, review of the analytical framework, and revision of the manuscript.

In Paper III, Marco Arrieta developed the mechanics-based framework for flow-slide mobility assessment, curated and reanalyzed the historical failure database, carried out the analytical derivations, back-calculations, statistical analysis, and visualization, and drafted the manuscript. Zong-Xian Zhang contributed to conceptual refinement, methodological oversight, discussion of the geo-mechanical interpretation, and critical revision of the manuscript.

The thesis-level synthesis that links field-scale gradation, stress-dependent shear strength, and flow-slide mobility was developed by Marco Arrieta for this dissertation.

TABLE OF CONTENTS

LIST OF FIGURES

LIST OF TABLES

1. INTRODUCTION

1.1. ENGINEERING CONTEXT AND THESIS MOTIVATION

Coarse mine waste hazard is governed by a chain of coupled geotechnical problems. The chain begins with measurable material state, continues through pre-failure resistance, and ends in post-failure consequence once resistance is reduced or lost. In coarse mine waste dumps, this chain develops within large anthropogenic landforms composed of blasted, excavated, and transported rock fragments. Unlike fine-grained storage systems, these dumps behave as very coarse granular systems whose response depends on particle interaction, breakage, segregation, stress increase during placement, and basal-foundation conditions. Their geotechnical performance is therefore governed jointly by material properties and placement/loading conditions (Valenzuela et al. 2008; Hawley and Cunning 2017; Gao et al. 2017).

From a geotechnical perspective, coarse mine waste dumps share key mechanical features with rockfill structures. Their stability and deformation are controlled by the stress-dependent behavior of coarse granular materials across a wide particle-size range, from fines to cobbles, boulders, and oversize blocks. The shear response of these materials is governed not by a single variable, but by the interaction of gradation, particle shape, surface roughness, intrinsic particle strength, density or porosity, and confining stress. A defining consequence is that shear strength becomes nonlinear with increasing confinement, making constant-friction-angle representations inadequate for many engineering problems (Indraratna 1994).

Within this response, gradation, usually expressed through particle-size distribution (PSD), is not a secondary descriptive variable. PSD affects packing, contact density, crushing susceptibility, permeability, and load transfer within granular assemblies, and it interacts with particle shape and particle strength. Changes in particle size are therefore not mechanically neutral. For coarse mine waste dumps, PSD is part of the measurable material state that governs pre-failure resistance (Yang et al. 2019; Ovalle and Dano 2020; Deiminiat et al. 2020; Carrasco et al. 2022).

The engineering problem does not end at pre-failure stability. Once resistance is reduced or lost, some failures may evolve into highly mobile flow slides capable of traveling long distances and affecting mine infrastructure, haul roads, downstream facilities, and surrounding terrain. Classical mobility descriptors such as angle of reach remain useful for screening, but high-mobility failures in mine waste and landslide systems show that basal friction reduction, pore-pressure generation, and path geometry can control runout in ways that simple geometric indices do not capture. This is especially important where waste dumps are founded on weak, saturated, or liquefaction-prone materials under rapid undrained loading (Heim 1932; Scheidegger 1973; Corominas 1996; Legros 2002; McDougall 2017). These controls are especially relevant for mine waste dumps founded on weak, saturated, or liquefaction-prone materials, where rapid undrained loading may reduce effective stress and trigger extreme runout behavior (Bishop 1973; Dawson et al. 1998).

The geotechnical challenge is therefore broader than a single stability calculation. It requires a continuous engineering logic that begins with field-scale characterization of coarse dump material, continues through the translation of that state into a defensible representation of pre-failure resistance, and ends with consequence assessment once resistance is overcome. This thesis is motivated by the fact that, in current practice, these stages are still too often treated separately.

1.2. Problem definition: The state-resistance-consequence discontinuity

The first problem, in coarse mine waste assessment, is the definition of material state at operational scale. Conventional sieve-based PSD determination is appropriate for many engineering aggregates, but it becomes difficult or impractical for coarse waste-rock and rockfill systems containing particles that range from gravel to meter-scale blocks. Full-scale field gradation is labor-intensive, time-consuming, and may expose personnel to unsafe conditions on active dump faces and inaccessible slopes. In practice, coarse waste dumps are therefore often characterized through visual estimates or limited local measurements that do not capture dump-scale heterogeneity or segregation (Marschi et al. 1972; Kemeny 1994; Sanchidrián et al. 2006).

A second problem follows directly from this measurement difficulty. When field-scale characterization is weak or incomplete, laboratory testing commonly relies on scaled-down gradations produced by scalping or parallel grading. These procedures are operationally convenient because they allow coarse materials to fit within available testing devices, but they also modify the original material system. Changes in particle size can alter particle strength, particle shape, breakage behavior, and contact structure, so the measured response of the scaled specimen does not necessarily represent the field material, especially at low to intermediate stress levels. The result is a persistent disconnect between the dump that governs the hazard and the specimen that governs the calibration (Ovalle and Dano 2020; Deiminiat et al. 2020; Deiminiat and Li 2022; Carrasco et al. 2022).

A third problem lies in the representation of pre-failure resistance. The field already contains several nonlinear formulations for rockfill and coarse granular materials, and these have long been useful in engineering interpretation and design. The weakness is not the absence of envelope forms. It is that their calibration still depends strongly on the available triaxial window and on fitted parameters whose link to field-measurable state remains weak. Even where stress-dependent behavior is recognized correctly, the route from measurable dump material state to defensible pre-failure shear-strength representation is still underdeveloped (Charles and Watts 1980; Barton and Kjaernsli 1981; Indraratna et al. 1993; Indraratna 1994; Ovalle et al. 2014).

A fourth problem emerges after failure initiation. Once resistance is reduced or lost, the controlling engineering question becomes post-failure consequence: how far the failed mass may travel, how rapidly it may move, and which conditions sustain that motion. Available approaches range from empirical runout correlations to frictional and Voellmy-type formulations (Dawson 1994; Golder Associates and Hungr 1995; Hungr 1995; Hungr et al. 2002; Aaron and McDougall 2019). These are useful, but they typically depend on basal friction, pore-pressure ratio, and turbulence parameters that are uncertain, back-calculated, or strongly site-specific. In high-end waste dumps, where undrained loading or basal liquefaction can sharply reduce effective stress, mobility may be amplified further by confinement and path geometry. Consequence assessment therefore remains difficult to anchor within one continuous geotechnical workflow (Bishop 1973; Nicoletti and Sorriso-Valvo 1991; Dawson 1994; Dawson et al. 1998; Aaron and McDougall 2019).

The problem addressed in this thesis is not the absence of characterization methods, nonlinear strength criteria, or mobility models in isolation. It is the lack of continuity between three linked domains that are still too often treated separately: field-scale material state, pre-failure resistance, and post-failure consequence. This dissertation addresses that discontinuity as a state-resistance-consequence problem rather than as three disconnected technical tasks.

1.3. Thesis gap and position

The literature already contains strong contributions within the three domains relevant to this thesis. In rockfill mechanics, decades of research have established that coarse granular materials exhibit nonlinear, stress-dependent shear behavior influenced by gradation, confinement, and particle properties (Marsal 1967; Leps 1970; Charles and Watts 1980; Barton and Kjaernsli 1981; Indraratna et al. 1993; Indraratna 1994; Ovalle et al. 2014). In field characterization, image analysis and, more recently, Structure-from-Motion and UAV photogrammetry have expanded the practical possibility of measuring coarse particle systems over large areas and inaccessible slopes (Kemeny 1994; Sanchidrián et al. 2006, 2009; Westoby et al. 2012; Colomina and Molina 2014; Bar et al. 2020). In mobility analysis, empirical and mechanics-based approaches have improved understanding of landslide and waste-dump runout, particularly in relation to basal friction reduction, liquefaction, and geomorphic confinement (Heim 1932; Scheidegger 1973; Corominas 1996; Dawson et al. 1998; Legros 2002; McDougall 2017; Aaron and McDougall 2019).

These advances remain structurally separated. Characterization studies usually stop at measurement or description and do not constrain nonlinear resistance representation. Shear-strength studies provide useful envelope forms but often rely on laboratory calibration that is only weakly tied to field-scale material-state descriptors. Mobility studies address the consequence of failure but typically treat basal properties and rheological parameters as assumed or back-calculated inputs rather than as part of one field-to-consequence geotechnical chain. In mine waste engineering, this separation is intensified by material heterogeneity and segregation, which can vary significantly across dump faces and along slopes (Qiu and Pabst 2023).

The thesis gap is therefore structural, not informational. The missing piece is not another descriptor, another envelope form, or another runout model in isolation. It is a coherent field-to-consequence framework for coarse mine waste dumps that begins with measurable dump-scale gradation, uses that state to inform stress-dependent shear-strength representation, and then carries the analysis into post-failure mobility under reduced basal resistance.

1.4. AIM AND OBJECTIVES

The aim of this thesis is to develop an integrated field-to-consequence geotechnical framework for coarse mine waste dumps by connecting field-scale gradation, pre-failure resistance, and flow-slide mobility.

To achieve this aim, the thesis pursues four objectives:

1. To establish a practical method for characterizing exposed field-scale gradation in coarse mine waste dumps where conventional sieving and full-scale manual gradation are impractical.
2. To determine how pre-shear gradation information can be used as a bounded curvature constraint in nonlinear stress-dependent shear-strength representation for rockfills and waste-rock materials.

3. To determine how reduced basal resistance, pore pressure, turbulence, and path geometry govern the post-failure mobility of high-end waste-dump flow slides.
4. To integrate these components into a defensible field-to-consequence engineering workflow for coarse mine waste assessment.

1.5. Central hypothesis and research questions

The central hypothesis of this thesis is that field-measurable pre-failure gradation descriptors can provide bounded state information for constraining stress-dependent shear-strength representation and for strengthening the analytical continuity between pre-failure characterization and post-failure consequence assessment when used within mechanics-based workflows rather than as isolated empirical variables.

This central hypothesis is examined through the following research questions:

RQ1. How can the gradation of coarse mine waste dumps be characterized reliably at operational field scale?

RQ2. How can pre-shear gradation information be used to constrain curvature in stress-dependent shear-strength representation?

RQ3. Once basal resistance is reduced or lost, how do pore pressure, basal friction, turbulence, and path geometry govern post-failure flow-slide mobility?

RQ4. How can these three levels be integrated into a defensible field-to-consequence geotechnical workflow for coarse mine waste assessment?

Together, these questions define the thesis chain from material state to pre-failure resistance, to post-failure consequence. That chain is the backbone of the dissertation.

1.6. Scope and claim boundary

This thesis claims integration, not universality. It focuses on coarse mine waste dumps and their associated rockfill and waste-rock materials, with emphasis on coarse granular systems in which gradation, particle characteristics, and stress-dependent response govern engineering behavior. It does not attempt to cover the full range of mine waste systems, and it does not generalize directly to all granular geomaterials.

The thesis is deliberately scoped across three linked domains.

1. In the field-characterization domain, the focus is on dump-scale visible material state, especially PSD estimation from aerial photogrammetry. This does not constitute direct reconstruction of the internal gradation of the full dump mass.
2. In the resistance domain, the focus is on stress-dependent pre-failure resistance representation and on the use of pre-shear gradation as a calibration constraint. It does not claim a universal constitutive law for all rockfills, waste-rock materials, or loading paths.
3. In the consequence domain, the analysis is screening-level and mechanics-based, aimed at interpreting high-end waste-dump flow slides through basal friction, pore pressure, turbulence, and path geometry. It is not a fully coupled site-specific hydro-mechanical simulation.

Accordingly, this thesis does not claim:

I. a universal constitutive law for coarse mine waste materials.
II. a single end-to-end predictive simulator from PSD to runout.
III. that PSD alone explains shear strength or flow-slide mobility.

Instead, it claims that PSD is a field-measurable state descriptor with sufficient engineering relevance to connect characterization, pre-failure resistance representation, and post-failure consequence assessment within one bounded framework.

1.7. THESIS CONTRIBUTION

The primary contribution of this thesis is the development of an integrated field-to-consequence geotechnical framework for coarse mine waste dumps. That thesis-level contribution is supported by three component advances.

1. The thesis advances the operational characterization of coarse mine waste gradation at field scale by showing how UAV photogrammetry can be used to estimate PSD in large, heterogeneous dump systems where traditional field gradation is impractical.
2. The thesis elevates pre-shear gradation from a descriptive variable to a calibration constraint in the representation of nonlinear stress-dependent shear strength. Gradation is therefore not treated as background information only, but as part of the logic used to discipline resistance calibration.

3. The thesis contributes a screening-level mechanics framework for flow-slide mobility in high-end waste dumps by analyzing the interaction of basal friction, pore pressure, turbulence, and path geometry, and by using a frictionless benchmark as a reference comparator for extreme mobility.
4. These three component advances support the main thesis-level contribution: a coherent framework that links measurable material state, pre-failure resistance representation, and post-failure consequence in one geotechnical chain.

1.8. Dissertation structure

This dissertation is organized as an article-based thesis consisting of a synopsis and three appended papers. Each Section performs one distinct task in the state-to-resistance-to-consequence chain.

1. Section 1 defines the engineering problem, thesis gap, aims, hypothesis, research questions, and claim boundary.
2. Section 2 establishes the scientific basis of the thesis chain and defines the formal thesis gap.
3. Section 3 converts that gap into a research design, evidence structure, and field-to-consequence workflow.
4. Section 4 resolves material state through field-scale PSD characterization and first-order shear-strength screening.
5. Section 5 resolves pre-failure resistance through PSD-constrained curvature in stress-dependent shear-strength representation.
6. Section 6 resolves post-failure consequence through the mechanics of flow-slide mobility in high-end waste dumps.
7. Section 7 integrates Sections 4 to 6 into one field-to-consequence geotechnical framework.
8. Section 8 defines the operational scope, methodological limits, and priority research needs of the integrated framework.
9. Section 9 answers the research questions and states the final thesis conclusion.
10. Section 10 presents the references.

The structure is cumulative rather than parallel. Section 4 establishes the measurable material state by showing that field-scale PSD can be obtained from UAV-based surface characterization and translated into first-order resistance screening. Section 5 carries that state concept into pre-failure resistance by evaluating finite-window pre-shear PSD scaling as a bounded curvature constraint in an existing stress-dependent power-law calibration route. Section 6 then crosses the failure boundary and interprets post-failure mobility through pore pressure, basal resistance, dynamic resistance, and path geometry. Section 7 connects these outputs into the state-resistance-consequence workflow, while Sections 8 and 9 define the operating limits and final answers to the research questions.

The sequence is therefore measurement, resistance representation, consequence assessment, and thesis-level synthesis.

2. MATERIAL STATE, PRE-FAILURE RESISTANCE, AND POST-FAILURE CONSEQUENCE: SCIENTIFIC BASIS AND THESIS GAP

This section establishes the scientific basis of the thesis chain: material state, pre-failure resistance, and post-failure consequence. It is not a general literature review. Section 2.1, Section 2.2 and Section 2.3 summarize the literature foundations needed for the thesis. Section 2.4 then provides the critical review by identifying the structural discontinuities that remain across those foundations and by defining the formal thesis gap.

2.1. MATERIAL STATE: GRADATION AND THE CHALLENGE OF FIELD-SCALE CHARACTERIZATION

Coarse mine waste dumps are granular systems whose response is governed by the coupled influence of gradation, particle morphology, particle strength, breakage, and confinement. Foundational rockfill research established that these variables jointly control shear resistance and that the strength envelope is stress-dependent rather than adequately represented by a single friction angle (Marsal 1967; Leps 1970; Charles and Watts 1980; Indraratna et al. 1993; Ovalle et al. 2014). More recent work has reinforced the role of gradation in contact transmission and critical-state response, confirming that gradation is a material-state descriptor with direct mechanical significance rather than a descriptive index (Yan and Dong 2011; Li et al. 2015; Yang et al. 2019).

For coarse mine waste, the mechanical significance of gradation depends on its interaction with particle angularity, roughness, size-dependent strength, and segregation during placement. Particle-shape effects influence force transfer and shear resistance, size-strength and size-shape correlations affect crushing and steady-shear behavior, and dump construction processes generate lateral and vertical heterogeneity in the visible material fabric (Shin and Santamarina 2013; Ovalle et al. 2014; Ovalle and Dano 2020; Carrasco et al. 2023; Qiu and Pabst 2023). Consequently, gradation cannot be treated as an isolated descriptor. Its value lies in capturing a measurable part of a broader material state.

In engineering practice, gradation is quantified through PSD. For coarse mine waste dumps, however, PSD characterization is constrained by particle scale, spatial variability, and field access. Standard sieve analysis remains suitable for fines and moderate particle sizes but becomes operationally inefficient for oversize fragments and unrealistic for dump-scale surveys. Manual field measurement and visual gradation preserve direct contact with the in-situ material, but they are slow, difficult to standardize, and weak in spatial representativeness on active dump faces and inaccessible slopes (Marschi et al. 1972; Breitenbach 2012).

The principal routes for PSD characterization in coarse mine waste are summarized in Table 1. Scaling-down techniques are intentionally excluded from the table because they are not characterization methods; they are representation methods used to adapt prototype material to laboratory devices.

Their relevance remains fundamental because they expose a second source of uncertainty: once the original material is reduced through scalping or parallel grading, the specimen no longer preserves the original size-strength and size-shape relations with certainty. This limitation is especially important at low to intermediate stress levels, where scale effects remain pronounced (Ovalle and Dano 2020; Deiminiat et al. 2020; Deiminiat and Li 2022).

The methodological development of PSD characterization has moved from direct measurement toward digital surface analysis. Early image-based approaches improved speed and repeatability relative to manual surveys, but their performance remained sensitive to scale calibration, particle overlap, shadowing, and fines obscuration. Later 3D and photogrammetric workflows reduced part of these limitations and extended characterization beyond isolated photographs. The most relevant advance for mine waste dumps is UAV-enabled Structure-from-Motion photogrammetry, which combines large-area coverage with three-dimensional reconstruction of unsafe or inaccessible slopes.

Table 1. Principal PSD characterization methods for coarse mine waste

Method	Typical scale	Primary PSD output	Main advantage	Principal limitation
Conventional sieve analysis	Sample scale	Direct PSD of recoverable fractions	Standardized direct measurement for fines to moderate particle sizes	Impractical for oversize particles and unsuitable for dump-scale surveys
Manual field measurement and visual gradation	Local exposure or bench scale	Approximate PSD or characteristic particle sizes	Direct observation of in situ coarse material	Time-intensive, operator-dependent, and weak in spatial representativeness
2D image analysis	Local surface scale	Surface-visible PSD from photographs	Faster than manual surveys and more repeatable under controlled imaging conditions	Sensitive to scale definition, occlusion, overlap, shadowing, and fines masking
3D image-based fragmentation	Local to slope scale	Surface PSD with geometric reconstruction	Improves particle delineation relative to 2D-only workflows	Still constrained by resolution, segmentation, and local coverage
UAV-SfM photogrammetry	Slope to dump scale	Spatially distributed, surface-visible PSD and characteristic sizes such as D_{50}	Large area coverage, three-dimensional reconstruction, and access to unsafe or inaccessible slopes	Surface only characterization, accuracy depends on flight design, control, resolution, and segmentation quality

Even with this progress, the characterization problem is not fully resolved. Image-based methods quantify the exposed surface state rather than the internal dump mass. Their accuracy depends on image resolution, flight geometry, ground control, and segmentation quality, while visible slopes may already be affected by segregation and local sorting (Abellan et al. 2016; Kong et al. 2021; Qiu and Pabst 2023). The literature therefore supports one bounded conclusion: field-scale PSD characterization in coarse mine waste is now technically feasible, and its geotechnical value depends on whether the measured state can be translated into a defensible representation of shear resistance.

This unresolved translation problem defines the transition to the next section. Once gradation is treated as a measurable material-state descriptor, the next question is how that state enters the representation of stress-dependent shear resistance in rockfill and waste-rock materials.

2.2. PRE-FAILURE RESISTANCE: STRESS-DEPENDENT BEHAVIOR IN ROCKFILL AND WASTE-ROCK MATERIALS

Once gradation is treated as a measurable material-state descriptor, the next issue is how that state enters pre-failure resistance representation. Rockfill and waste-rock materials do not exhibit a unique stress-independent friction angle. Large-scale testing established early that their resistance varies with confinement, and later studies confirmed that coarse granular response is governed by stress-dependent friction, dilation, and particle breakage. As confining stress increases, particle rearrangement and crushing become more pronounced, the apparent friction angle decreases, and the failure envelope becomes nonlinear (Newland and Allely 1957; Leps 1970; Charles and Watts 1980; Indraratna et al. 1993; Indraratna 1994; Ovalle et al. 2014).

This literature produced several families of shear-strength criteria for coarse granular materials. Early curved-envelope formulations linked resistance to particle sliding and deviation from the imposed shear direction (Newland and Allely 1957). Empirical power-law forms were later introduced for rockfill and embankment materials, with shear stress or principal stress expressed as a nonlinear function of normal or confining stress (De Mello 1977; Charles and Watts 1980; Charles 1990; Indraratna et al. 1993; Indraratna 1994). Size-effect studies reached the same conclusion from another direction: particle size influences not only geometry, but also particle strength and crushing susceptibility, which means that changing gradation can alter the resistance mechanism itself (Frossard et al. 2012; Ovalle et al. 2014; Li et al. 2015; Yang et al. 2019). Under these conditions, linear strength descriptions are structurally inadequate for very coarse mine waste.

Within this nonlinear framework, gradation enters the problem in two distinct ways. First, PSD influences density, coordination number, force transmission, and crushing tendency. Well-graded materials generally achieve denser packing and higher resistance than poorly graded assemblies, provided material quality and particle morphology remain comparable (Yan and Dong 2011; Li et al. 2015; Yang et al. 2019).

Second, PSD is often used operationally through characteristic sizes such as D50, which become inputs in empirical criteria for very coarse materials. The Barton-Kjaernsli criterion is the clearest example, because it links shear resistance to equivalent roughness R, basic friction angle ϕ_b, and size-dependent particle strength S derived from UCS and D_{50} (Barton and Kjaernsli 1981; Barton 2013, 2016). In this sense, PSD is already present in rockfill mechanics. Its role, however, is typically indirect: it enters through characteristic sizes or empirical surrogates, but it rarely constrains the curvature of the stress-dependent envelope itself.

This distinction is critical for mine waste engineering. In practice, the main obstacle is rarely the absence of a nonlinear criterion. The obstacle is calibration. Several widely cited formulations depend on fitted parameters that are not transferable without substantial case-specific testing. The power-law forms of De Mello and Charles and Watts require coefficients defined from laboratory data (De Mello 1977; Charles and Watts 1980).

Gonzalez's logarithmic formulation also depends on a large triaxial database (Gonzalez 1985). Charles's later formulation introduces constants that remain site-specific (Charles 1990). Fractal approaches proposed by Xu are conceptually attractive, but their practical use still depends on reliable PSD acquisition and on parameters that remain difficult to estimate robustly for field materials; they also do not by themselves establish a bounded calibration route for assigning curvature within a selected engineering envelope family (Xu et al. 2015; Xu 2018). The gap in current practice is therefore not mathematical scarcity. It is the absence of a disciplined route for constraining curvature independently of free fitting (Table 2).

The problem becomes more acute when prototype particles exceed the capacity of available laboratory devices. Under those conditions, scalping and parallel grading are routinely used to create testable specimens. Once the original gradation is modified, size-strength and size-shape correlations are modified as well, and the measured response no longer provides a clean bridge back to the field material.

Recent reviews have shown that scaling-down procedures may reproduce part of the response under high stress, but their reliability decreases at low to intermediate stress levels where particle correlations remain important (Ovalle and Dano 2020; Deiminiat et al. 2020; Deiminiat and Li 2022). For very coarse mine waste, this explains why engineering practice still relies heavily on empirical or probabilistic routes to estimate resistance when prototype-scale testing is infeasible (Linero Molina et al. 2021; Contreras et al. 2022).

From the literature, three conclusions follow.

1. First, stress-dependent shear resistance is intrinsic to rockfill and waste-rock materials.

2. Second, gradation is mechanically relevant and already enters several interpretations of coarse material behavior.
3. Third, current practice still lacks a clear bounded route for using pre-shear PSD as a curvature constraint in a nonlinear resistance envelope rather than treating PSD as background description or as an indirect input to empirical charts.

This unresolved issue defines the pre-failure mechanics gap addressed by this thesis.

Table 2. Representative stress-dependent shear-strength criteria and calibration limits

Criterion family	Representative basis	Main variables	Calibration demand	Main limitation, for coarse mine waste	References
Newland-Allely	Curved envelope based on particle sliding and deviation angle	Normal stress, basic friction, particle displacement angle	Moderate	Early conceptual form; not designed for field-scale dump calibration	(Newland and Allely 1957)
De Mello Charles-Watts power-law	Nonlinear power relation between shear stress and normal stress	Fitted constants, normal stress	High	Coefficients are site-specific and require laboratory calibration	(De Mello 1977) (Charles and Watts 1980)
Barton-Kjaernsli	Empirical nonlinear criterion for coarse materials	R, S, ϕ_b, normal stress, D_{50}, UCS	Moderate	Sensitive to estimation of roughness and equivalent strength; still empirical	(Barton and Kjaernsli 1981; Barton 2013, 2016)
Indraratna family	Power-law relation in principal stress space under static and dynamic loading	Principal stresses, gradation, confinement	High	Requires large-scale triaxial data and remains calibration-intensive	(Indraratna et al. 1993, 1998; Indraratna 1994)
Frossard size-effect framework	Rational interpretation of rockfill strength through size effects	Grain size, confinement, size effect	Moderate to high	Strong physical basis; still requires careful characterization of size effects	(Frossard et al. 2012)
Fractal/fragmentation family	Power-law form linked to fractal particle breakage	Fractal dimension, PSD, crushing descriptors	High	Parameter estimation remains difficult for field materials and practical calibration is not straightforward	(Xu et al. 2015; Xu 2018)

A final implication follows immediately. Pre-failure resistance representation is essential, but hazard assessment cannot end there. Once resistance is reduced or lost, the engineering question shifts from strength to consequence. That transition leads directly to the literature on flow-slide mobility, pore pressure, path geometry, and dynamic resistance reviewed in the next section.

2.3. POST-FAILURE CONSEQUENCE: PORE PRESSURE, PATH GEOMETRY, AND DYNAMIC RESISTANCE

Once failure initiates, the engineering problem shifts from pre-failure resistance to post-failure consequence. The key questions become how far the failed mass may travel, how rapidly it may move, and which field conditions control that behavior. In landslide and mine-waste literature, mobility is commonly described through runout distance, travel time, velocity, and the angle of reach. Classical empirical treatments relate these outcomes to fall height or simple geometric descriptors and remain useful for first-pass screening and regional comparison (Heim 1932; Scheidegger 1973; Corominas 1996). Their limitation is structural: they reduce post-failure behavior to geometric indices and do not explicitly represent transient basal weakening, pore-pressure generation, or velocity-dependent resistance.

To move beyond empirical reach indices, mobility analysis often begins with sliding-block concepts and is then extended through frictional or Voellmy-type rheologies. In this family of models, basal resistance is represented by a friction term and, when required, by a velocity-squared term that captures turbulent or collisional dissipation (Voellmy 1955; Perla et al. 1980; Hungr 1995; Hungr and McDougall 2009).

This framework is influential because it links field-observable geometry with dynamic resistance in a form suitable for back-analysis and forward screening. Parameter selection nevertheless remains difficult, especially in mine waste environments, where basal conditions, saturation state, and path material may change abruptly during motion (Hungr and McDougall 2009; McDougall 2017).

A central control in high-mobility flow slides is the reduction of effective basal resistance through pore-pressure increase. Long-runout failures have long been associated with basal lubrication, fluidization, or liquefaction of weak saturated materials. In waste-dump settings, the most operationally relevant interpretation is rapid undrained loading at the basal bed, commonly discussed through effective-stress reasoning and Bishop-type pore-pressure formulations that relate stress increase to pore-pressure response (Bishop 1959, 1973).

When pore pressure rises, effective normal stress falls, basal shear resistance drops, and mobility increases. Case histories of mine-waste failures in the Canadian Rockies made this mechanism especially important for high-end dumps founded on low-permeability or saturated materials (Dawson 1994; Dawson et al. 1998). The broader mobility literature supports the same general reading, namely that elevated pore pressure is one of the clearest drivers of long runout in rapid granular failures (Kent 1966; Legros 2002; Sassa Kyoji and Wang 2005).

Path geometry introduces a second layer of control. Geomorphic studies showed early that runout shape and reach depend on channelization, spreading, and the nature of the travel corridor rather than on source geometry alone. Confined paths concentrate the moving mass, increase flow depth, and can sustain higher velocities over longer distances, whereas unconfined settings promote lateral spreading and earlier energy dissipation (Benda and Cundy 1990; Nicoletti and Sorriso-Valvo 1991). The material encountered along the path also matters, since bedrock, colluvium, previous-slide debris, and saturated deposits change the effective interaction at the base of the flow (Hungr and Evans 2004; Aaron and McDougall 2019). Mobility is therefore a property of the full travel system rather than of the release zone in isolation.

These controls are coupled. Elevated pore pressure lowers effective basal resistance. Reduced resistance allows velocity growth. Increasing velocity raises the significance of dynamic-resistance terms. Path confinement and geometry determine whether that momentum is dissipated rapidly or preserved along the travel path. This coupled interpretation explains why mobility assessment remains calibration-intensive even when the governing mechanisms are conceptually established (Hungr and McDougall 2009; McDougall 2017). One unresolved issue in the literature is the limited use of a clear frictionless reference against which observed flow slides can be interpreted. Empirical reach indices and rheological simulations estimate mobility relative to past cases or calibrated resistance parameters, although they rarely define a no-dissipation comparator. The classical Brachistochrone, or minimum-time path, offers such a reference in mechanics.

Its value in geotechnical interpretation does not lie in claiming that a real flow slide follows a cycloid. Its value lies in providing a frictionless reference comparator for velocity and travel time against which the effects of pore pressure, friction, turbulence, and path geometry may be discussed cautiously (Erlichson 1999).

Accordingly, the mobility literature provides strong partial explanations. It identifies empirical mobility patterns, clarifies the role of basal weakening and pore pressure, and supplies dynamic-resistance frameworks for runout analysis (Table 3). What remains unresolved is continuity: a field-oriented screening framework that combines pore-pressure effects, path geometry, and dynamic resistance in one interpretation while also comparing real events against a defensible frictionless reference. This unresolved consequence problem forms the final literature pillar of the thesis.

Table 3. Main controls and descriptors of post-failure mobility

Control	Common descriptors	Typical literature representation	Main limitation in waste-dump practice	References
Empirical reach	H, L, angle of reach (β)	Geometric mobility indices and runout correlations	Useful for screening, weak in process representation	(Heim 1932; Scheidegger 1973; Corominas 1996)
Basal resistance	f, φ_b	Sliding block and frictional mobility models	Difficult to assign without back-analysis	(Hungr 1995; Hungr and McDougall 2009)
Pore pressure	μ, r_u, effective stress	Liquefaction and basal-weakening interpretations	Strong temporal uncertainty during rapid failure	(Bishop 1959, 1973; Dawson et al. 1998; Sassa Kyoji and Wang 2005)
Dynamic resistance	ξ	Voellmy-type velocity-dependent resistance	Calibration remains highly site-dependent	(Voellmy 1955; Perla et al. 1980; McDougall 2017)
Path geometry and material	Confinement, channelization, basal material	Geomorphic and path-based mobility interpretation	Difficult to quantify consistently at field scale	(Nicoletti and Sorriso-Valvo 1991; Hungr and Evans 2004; Aaron and McDougall 2019)
Frictionless benchmark	v_{opt}, t_{opt}	Minimum-time or Brachistochrone reference	Rarely incorporated in engineering screening	(Erlichson 1999)

2.4. Critical Review - Structural Thesis Gap and Thesis Position

The critical review of the preceding literature leads to three conclusions. First, gradation is mechanically relevant in coarse mine waste, rockfill, and waste-rock materials because it affects packing, contact density, breakage, and stress-dependent response (Leps 1970; Barton and Kjaernsli 1981; Indraratna et al. 1993; Indraratna 1994; Frossard et al. 2012).

Second, the pre-failure shear resistance of these materials is nonlinear and confinement-dependent, and the field already contains several envelope families for representing that behavior.

Third, flow-slide mobility is controlled by the combined action of basal weakening, pore pressure, dynamic resistance, and path geometry, rather than by slope geometry alone (Dawson 1994; Hungr 1995; Dawson et al. 1998; Hungr and McDougall 2009; McDougall 2017).

The literature therefore does not suffer from a shortage of descriptors, criteria, or case histories. Its weakness is structural: continuity across these domains remains weak.

2.4.1. *First disconnection: Measurement without continuity to mechanics*

Recent developments in image analysis, photogrammetry, and UAV-SfM have made field-scale PSD characterization technically feasible for large and inaccessible dump slopes (Westoby et al. 2012; Colomina and Molina 2014). This is a real advance because conventional sieving, manual field gradation, and local visual surveys are impractical at dump scale. Even so, most characterization studies still stop at measurement, description, or empirical screening.

Paper I moves further by translating UAV-derived PSD into Barton-Kjaernsli shear-strength inputs, which is a meaningful geotechnical step. The limitation remains clear: that route is still empirical and still depends on quantities such as roughness and equivalent particle strength that are not directly measured from the dump-scale surface state alone. The front-end problem is therefore only partially solved. Field-scale PSD can now be measured, but the literature still offers limited guidance on how that measured state should discipline the structure of a nonlinear resistance model rather than simply populate empirical inputs.

2.4.2. Second disconnection: Nonlinear criteria without disciplined calibration

The resistance literature is mature in mathematical form and weak in calibration discipline. Nonlinear criteria already exist for rockfill and waste-rock materials, and their stress dependence is well established (Charles and Watts 1980; Barton and Kjaernsli 1981; Indraratna et al. 1993; Indraratna 1994; Frossard et al. 2012). The persistent weakness lies elsewhere: most formulations depend on fitted constants, large triaxial programs, or site-specific regressions.

The bridge back to the prototype weakens further when scaled-down specimens are used, because the original field gradation and the associated size-strength and size-shape relations are modified. The unresolved issue is therefore not the absence of nonlinear criteria (Charles and Watts 1980; Barton and Kjaernsli 1981; Indraratna et al. 1993; Frossard et al. 2012). It is the absence of a disciplined route for constraining curvature with a field-meaningful pre-shear state descriptor rather than with free fitting alone (Ovalle and Dano 2020; Deiminiat et al. 2020; Deiminiat and Li 2022).

This is the precise opening for the middle contribution of the thesis.

2.4.3. Third disconnection: Consequence analysis without continuity to pre-failure state

The mobility literature explains much of the post-failure problem, but consequence assessment usually starts only after failure has already been idealized. Empirical reach relations provide first-pass screening. Frictional and Voellmy-type formulations provide dynamic frameworks. Pore-pressure and liquefaction studies explain why basal resistance can collapse. Geomorphic studies show why confinement and path material may amplify or limit travel (Bishop 1973; Nicoletti and Sorriso-Valvo 1991; Dawson 1994; Hungr 1995; Dawson et al. 1998; Hungr and McDougall 2009; Aaron and McDougall 2019).

Paper III shows that these controls can be assembled into a more coherent screening-level framework and that a frictionless benchmark is useful because current practice lacks a clear reference state for mobility. Even so, basal friction, pore-pressure ratio, turbulence, and path geometry are still commonly assumed or back-calibrated after the event. The consequence literature is therefore mechanically informative and still weak in continuity with pre-failure characterization.

2.4.4. Formal thesis gap and position

Existing descriptors, criteria, and runout models remain structurally disconnected. No framework establishes a continuous analytical sequence from measurable dump-scale gradation to stress-dependent shear-strength representation and subsequent flow-slide mobility governed by pore pressure, dynamic resistance, and path geometry.

This thesis closes that discontinuity through three sequential steps:

1. It makes field-scale PSD operational through UAV photogrammetry.
2. It promotes pre-shear PSD from description to calibration constraint in nonlinear shear-strength representation.
3. It interprets post-failure mobility through the coupled effects of basal weakening, pore pressure, dynamic resistance, and path geometry, with a frictionless benchmark used as a reference comparator rather than as a literal physical path.

The contribution is therefore the continuity across these three levels: an integrated field-to-consequence framework for coarse mine waste dumps. It is neither a universal constitutive law nor a single end-to-end predictive simulator.

3. Research design, evidence structure, and field-to-consequence workflow

Section 3 converts the thesis gap identified in Section 2 into a research design. It defines the analytical architecture of the dissertation, the evidence supporting each analytical level, and the workflow that links material state, pre-failure resistance, and post-failure consequence. This section does not repeat the literature review or preview the detailed results of the core Sections. Its function is to fix how the thesis claims are constructed, how far they can validly extend, and how the appended studies operate as one cumulative argument.

This section proceeds in three steps. Section 3.1 defines the analytical architecture of the thesis in the order material state, pre-failure resistance, and post-failure consequence. Section 3.2 formalizes the hypotheses, evidence base, and inference limits associated with each analytical level. Section 0 establishes the integrated field-to-consequence workflow and clarifies how the appended studies function together as one cumulative thesis argument. Across these sections, the dissertation is treated as an integrated research program linking dump-scale PSD characterization, stress-dependent pre-failure resistance representation, and flow-slide mobility assessment in coarse mine waste dumps (Arrieta and Zhang 2024, 2025).

Section 3 therefore stays at the level of research design and analytical logic. Detailed field procedures are reserved for Section 4, calibration procedures for Section 5, and mobility analysis procedures for Section 6. By the end of this section, the reader should understand how the dissertation is assembled, what each Section is allowed to claim, and why the thesis contribution exceeds the appended papers taken separately.

3.1. Analytical architecture: Material state, pre-failure resistance, and post-failure consequence

This dissertation is coherent because the appended studies resolve successive parts of one geotechnical problem. In this thesis, that problem is the discontinuous treatment of coarse mine waste across three domains that are too often assessed separately: measurable material state, pre-failure resistance, and post-failure consequence. The analytical architecture is therefore sequential. It follows the chain from state, to resistance, to consequence.

The common object across the thesis is the coarse mine waste dump, treated as a large granular system composed of rockfill and waste-rock materials. The first analytical level is material state.

At this level, the central requirement is operational field characterization. Paper I establishes a UAV-based route for dump-scale particle-size distribution estimation and shows that measured surface gradation can be translated into geotechnically relevant descriptors for first-order resistance screening. Within the architecture of the thesis, this level provides the measurable state on which the remaining analytical levels depend (Arrieta and Zhang 2024).

The second analytical level is pre-failure resistance. Once gradation has been established as a measurable state descriptor, the next requirement is to define how that state enters the representation of stress-dependent shear strength. Paper II addresses that requirement by treating pre-shear PSD as a calibration-relevant descriptor in nonlinear resistance representation. Within the analytical architecture, this level converts measured material state into a more disciplined representation of pre-failure resistance. Its role is mechanistic and calibration-oriented, not descriptive (Arrieta and Zhang 2026).

The third analytical level is post-failure consequence. Pre-failure resistance does not exhaust the hazard problem in high-end waste dumps, because once basal resistance is reduced or lost, the governing question becomes mobility. Paper III addresses this level by interpreting flow-slide behavior through the coupled influence of pore pressure, basal friction, dynamic resistance, and path geometry, while using a frictionless benchmark as a reference comparator for extreme mobility. Within the architecture of the thesis, this level translates reduction or loss of resistance into consequence analysis (Arrieta and Zhang 2025).

These three analytical levels are sequential and mechanically linked. They are not presented as a single end-to-end predictive simulator, and their continuity does not depend on propagating one universal parameter set from UAV-derived PSD directly into runout prediction. The continuity claimed by the thesis is analytical and mechanical: measurable material state defines the basis for resistance representation, and the reduction or loss of that resistance defines the basis for mobility interpretation. This sequence fixes the order of the dissertation: measurement first, resistance second, consequence third.

With the analytical architecture fixed in this form, Section 3.2 now defines the evidence supporting each level and the limits of valid inference.

3.2. EVIDENCE STRUCTURE, HYPOTHESES, AND VALID INFERENCE LIMITS

The dissertation is supported by three distinct evidence bases aligned with the three analytical levels of the thesis: material state, pre-failure resistance, and post-failure consequence. It does not rely on one homogeneous dataset or one unified predictive model. Its validity depends on matching each claim to the evidence that can actually support it. The evidence structure is therefore stratified. Field-characterization evidence supports claims about measurable state. Calibration-oriented evidence supports claims about pre-failure resistance representation. Historical-failure evidence supports claims about post-failure consequence. Measurement evidence cannot support the same claim as calibration evidence, and neither can support the same claim as historical mobility evidence.

The central thesis hypothesis is operationalized here into four hypotheses.

1. H1. Dump-scale PSD can be characterized reliably from UAV-derived surface measurements and translated into first-order geotechnical inputs.
2. H2. Pre-shear PSD scaling can provide a bounded curvature constraint in nonlinear stress-dependent shear-strength representation.
3. H3. Once resistance is reduced or lost, flow-slide mobility is governed by the coupled effects of pore pressure, basal friction, dynamic resistance, and path geometry.
4. H4. These three analytical levels can be integrated into a defensible field-to-consequence workflow for coarse mine waste assessment

H1-H3 are study-level hypotheses tested by Papers I-III. H4 is a thesis-level hypothesis and is tested only by synthesis across Sections 4 to 7.

At the first analytical level, the evidence base is field-derived. Paper I examines five coarse mine waste dumps using UAV photogrammetry and Structure-from-Motion reconstruction and validates the digital measurements against manual field measurements of 50 boulders. Paper I reports surface-visible PSD descriptors, including D_{50}, and translates these measurements into first-order geotechnical screening inputs through the Barton-Kjaernsli criterion (Arrieta and Zhang 2024).

The valid inference at this level is bounded to field-scale measurement feasibility and geotechnical translation. Paper I establishes that dump-scale PSD characterization is operationally feasible for coarse mine waste and that the resulting data can support first-order resistance screening. It does not reconstruct the internal grading of the full dump mass, and it does not constitute constitutive proof of shear-strength behavior. At the second analytical level, the evidence base is calibration oriented. Paper II addresses stress-dependent shear strength by evaluating pre-shear PSD scaling as a bounded curvature constraint within a nonlinear resistance representation. The role of this evidence is narrower than universal prediction and stronger than descriptive correlation. It tests whether a field-meaningful state descriptor can reduce arbitrariness in envelope calibration and strengthen the link between measurable material state and pre-failure resistance representation.

The valid inference at this level is a calibration inference. It supports the claim that pre-shear PSD can function as a constraint on nonlinear shear-strength calibration. It does not support a universal constitutive law, and it does not eliminate the need for material-specific data where high-confidence design is required. At the third analytical level, the evidence base is historical and mechanics based. Paper III analyzes 46 documented high-end waste-dump failures in southeastern British Columbia and interprets mobility through sliding-block concepts, Bishop-type pore-pressure reasoning, Voellmy-type dynamic resistance, path confinement, and a Brachistochrone-based frictionless benchmark (Golder Associates 1991; Golder Associates and Hungr 1995; Arrieta and Zhang 2025). The valid inference at this level is a screening-level consequence inference. It supports the claim that mobility can be interpreted mechanically through pore pressure, basal resistance, dynamic resistance, and path geometry. It does not support site-specific hydro-mechanical runout prediction or a universal mobility law.

The inference structure of the dissertation is therefore bounded. Section 4 supports a claim of field-scale PSD characterization and first-order geotechnical translation. Section 5 supports a claim of calibration discipline in stress-dependent pre-failure resistance representation. Section 6 supports a claim of mechanics-based mobility interpretation for screening-level consequence assessment. Section 7 supports the integration claim across material state, pre-failure resistance, and post-failure consequence. Claims extending beyond those four levels exceed the evidence base of the dissertation. Table 4 summarizes this structure.

A second boundary is equally important. The continuity claimed by the dissertation is analytical and mechanical, not fully numerical. The thesis does not present a single simulator in which UAV-derived PSD is propagated through one constitutive law into direct runout prediction. The continuity lies in the structured transfer of geotechnical meaning: measurable material state informs pre-failure resistance representation, and the degradation or loss of that resistance frames post-failure consequence. This is the strongest defensible continuity supported by the available evidence.

With the evidence structure and inference limits fixed in this manner, Section 3.3 can formalize the integrated workflow and the linkage between the core Sections.

Table 4. Evidence base and valid inference limits across the thesis

Analytical level	Evidence source	Main procedure	Primary output	Valid inference	Claim excluded
Material state	Paper I; five waste dumps; UAV images and field validation	UAV-SfM PSD characterization and validation	Dump-scale surface PSD, D50, geotechnical screening inputs	Measurement feasibility and geotechnical translation	Full internal gradation reconstruction; constitutive proof
Pre-failure resistance	Paper II; appended analytical study using PSD-informed resistance representation	PSD-constrained nonlinear calibration	Bounded curvature-constrained stress-dependent shear-strength representation	Bounded calibration discipline and reduced curvature-fitting arbitrariness	Universal constitutive law; full predictive generalization
Post-failure consequence	Paper III; 46 historical failures from southeastern British Columbia	Mechanics-based mobility analysis using pore pressure, friction, path geometry, and dynamic resistance	Mobility interpretation, screening thresholds, frictionless benchmark comparison	Screening-level consequence assessment	Site-specific hydro-mechanical runout prediction
Thesis synthesis	Sections 4 to 7	Cross-Section integration	Field-to-consequence framework	Integrated geotechnical workflow	Single end-to-end numerical simulator

3.3. INTEGRATED FIELD-TO-CONSEQUENCE WORKFLOW AND SECTION LINKAGE

This dissertation is integrated through a field-to-consequence workflow rather than through a single end-to-end predictive simulator. The purpose of the workflow is to define how each core Section receives a bounded input, resolves one analytical task, and transfers a defined output to the next level of the thesis. The dissertation is therefore cumulative, not parallel. Figure 1 summarizes this workflow and the linkage between the core Sections. The workflow begins in Section 4 where the analytical task is the characterization of material state at operational field scale. Paper I shows that UAV photogrammetry and Structure-from-Motion can reconstruct waste-dump surfaces, estimate PSD at dump scale, and derive characteristic sizes such as D_{50} for coarse mine waste materials (Arrieta and Zhang 2024).

Within the workflow, the critical output of Section 4 is not the imagery itself, nor the three-dimensional model as an end in itself. It is a measurable gradation descriptor that can be carried into geotechnical interpretation. This is the first essential handoff in the dissertation. Without a field-scale descriptor of material state, the remaining stages revert to unsupported fitting, laboratory abstraction, or qualitative judgment.

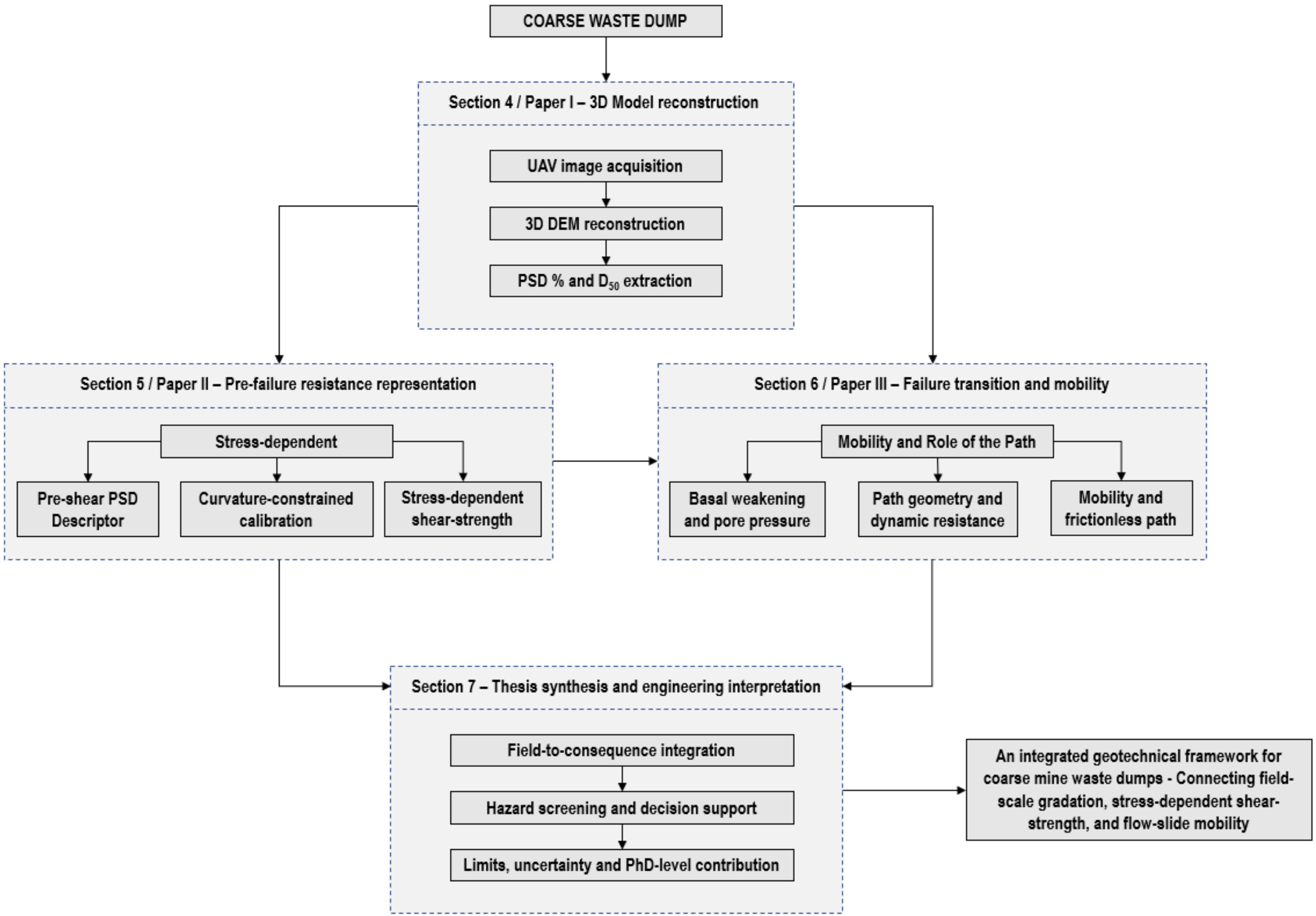

Figure 1. Field-to-consequence workflow and linkage between thesis sections

The second stage of the workflow is developed in section 5, where the analytical task is the representation of pre-failure resistance. At this stage, the thesis no longer asks whether gradation can be measured. It asks how measured pre-shear gradation enters the calibration of stress-dependent shear strength. Paper II addresses that problem by treating pre-shear PSD as a calibration-relevant descriptor in nonlinear shear-strength representation rather than as background description alone (Arrieta and Zhang 2026).

The critical output of Section 5 is a constrained representation of stress-dependent pre-failure resistance. The handoff from Section 4 to Section 5 is mechanistic: field-scale gradation becomes calibration-relevant state information. This is the point at which material characterization becomes resistance representation.

The third stage of the workflow is addressed in Section 6, where the analytical task is no longer pre-failure resistance itself, but the consequence of its reduction or loss. This transition must be stated precisely. The dissertation does not propagate one calibrated resistance model directly from Section 5 into a single runout simulator in Section 6. That would exceed the evidence base of the thesis. The linkage is analytical rather than fully numerical. Once resistance is represented in a stress-dependent framework, the hazard problem can be reframed in post-failure terms: what governs mobility when basal resistance is reduced or lost? Paper III addresses that domain by interpreting flow-slide mobility through the coupled action of pore pressure, basal friction, dynamic resistance, and path geometry, with a Brachistochrone-based frictionless benchmark used as a reference comparator for extreme mobility (Arrieta and Zhang 2025). The critical output of Section 6 is therefore a mechanics-based interpretation of post-failure consequence.

Section 7 performs the thesis-level synthesis that none of the appended studies can perform independently. It reconnects the outputs of Sections 4, 5, and 6 into one engineering chain: field-scale characterization, pre-failure resistance representation, failure transition, and mobility assessment. In that synthesis, the state descriptor established in Section 4 and the resistance framework developed in Section 5 are not treated as isolated results. They are used to show why post-failure mobility cannot be interpreted independently of pre-failure material state and basal resistance conditions. The function of Section 7 is therefore integrative and thesis-level.

The section linkage is explicit. Section 4 establishes what can be measured. Section 5 establishes how that measured state disciplines pre-failure resistance representation. Section 6 establishes how post-failure consequence is interpreted once resistance is reduced or lost. Section 7 establishes how these three levels form an integrated geotechnical workflow for coarse mine waste dumps. This linkage defines the internal logic of the dissertation and explains why the appended studies are presented in thesis order rather than in publication order.

With the workflow and Section linkage fixed in this form, the dissertation can proceed to the first core analytical level: field-scale material-state characterization.

4. Field-scale PSD characterization and first-order shear-strength screening of coarse mineral waste dumps

Section 4 resolves the first analytical level of the dissertation: material state. Built mainly on Paper I, it tests whether surface-visible PSD can be characterized reliably at operational dump scale in coarse mine waste dumps. UAV photogrammetry and Structure-from-Motion reconstruction are used to estimate PSD across five waste dumps, validate those measurements against 50 manually measured boulders, and translate representative descriptors, particularly D_{50}, into first-order shear-strength screening through the Barton-Kjaernsli criterion (Barton and Kjaernsli 1981; Arrieta and Zhang 2024).

The purpose of the section is exactly to establish PSD as a defensible field-scale state descriptor for coarse mine waste dumps. It does not reconstruct the full internal grading of the dump mass, and it does not claim constitutive proof of shear resistance. Its contribution is to show that dump-scale surface characterization can support first-order geotechnical screening and provide the measurable state information required for the pre-failure resistance problem addressed in Section 5.

4.1. Study basis and material classes

This section uses five coarse mine waste dumps from an open-pit operation in the Caribbean archipelago. The mine name and coordinates are not reported because the field data are subject to confidentiality. The site is therefore identified at regional scale, and the field context is defined through the dump views in Figure 2 and the material properties in Table 5. The cases were selected to provide strong contrasts in material quality, PSD, and exposed surface texture at operational scale. The dataset includes blasted and quarried materials and spans intact-rock uniaxial compressive strengths from 14 to 40 MPa. That spread is not incidental. It creates the minimum geotechnical contrast required to test whether UAV-derived PSD can discriminate weaker, finer, and more degradable dump materials from stronger, coarser, and rockier dump materials under field conditions. Figure 2 shows the five analyzed dumps, and Table 5 summarizes the representative material properties that form the empirical basis of this section (Arrieta and Zhang 2024).

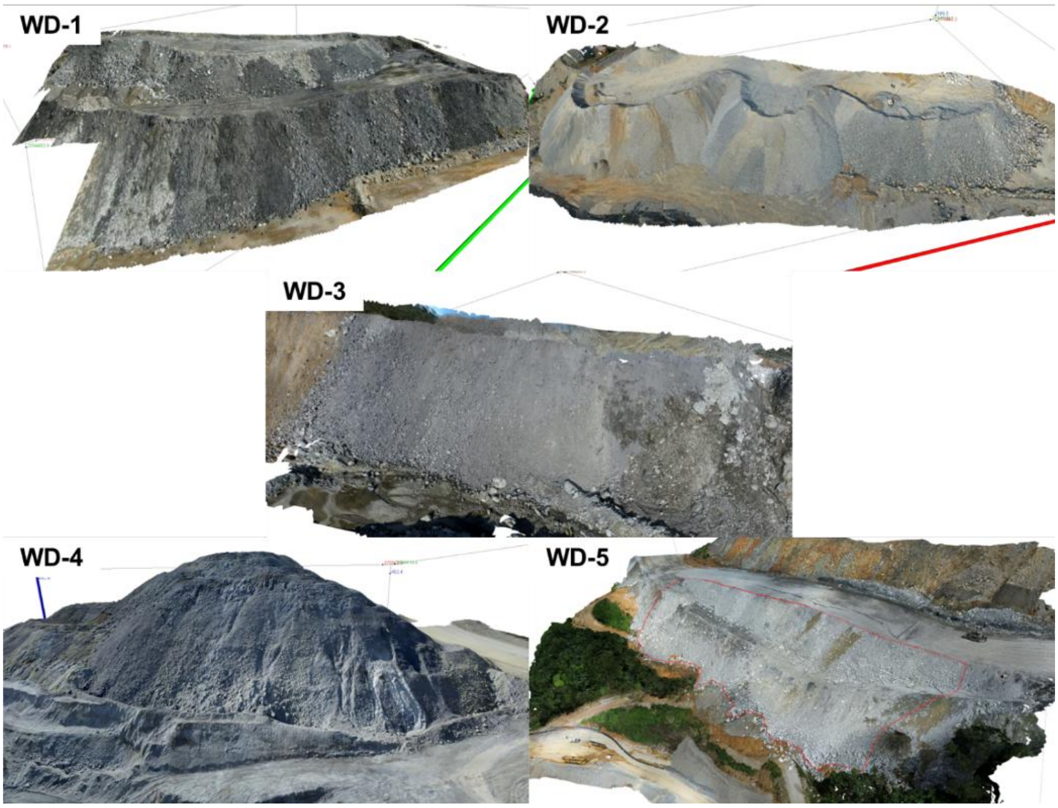

Figure 2. 3D views of the five waste dumps used as the Section 4 field basis

Table 5. Representative material properties of the five waste dumps used in Section 4

Waste dump	Dominant material	UCS (MPa)	Density Intact rock (g/cm³)	D_{10} (mm)	D_{30} (mm)	D_{50} (mm)	D_{60} (mm)	C_u	C_c
WD-1	Carbonaceous mudstone	14	2.65	9	83	200	267	31.6	3.1
WD-2	Limestone	30	2.80	37	77	135	165	4.4	1.0
WD-3	Carbonaceous mudstone	18	2.77	3	49	109	152	47.9	5.0
WD-4	Andesitic waste rock	35	2.79	187	469	788	845	4.5	1.4
WD-5	Andesitic waste rock	40	2.80	48	122	248	310	6.5	1.0

The five dumps represent three mechanically distinct groups.

1. WD-1 and WD-3 are weaker carbonaceous mudstone dumps with acid-generation potential and relatively low intact strength.
2. WD-2 is a limestone dump with intermediate strength and a gravel-to-cobble-dominated surface expression.
3. WD-4 and WD-5 are strong coarse rocky dumps dominated by volcaniclastic or andesitic waste, with the highest intact strengths and the largest exposed particle sizes in the dataset.

Across the five dumps, characteristic particle sizes extend from fine-rich surfaces to blocky materials with particles on the order of several hundred millimeters and locally above two meters. This spread is exactly what makes routine full-scale PSD measurement impractical in active mine conditions and justifies the use of a field-scale photogrammetric approach (Arrieta and Zhang 2024).

The study basis is intentionally restricted to surface-visible material state. The exposed dump face is not treated as a reconstruction of the internal dump mass. The question of the section is narrower and defensible: whether visible surface gradation can be characterized consistently enough to function as a field-scale state descriptor for geotechnical screening.

This restriction is methodologically necessary. The value of the five-dump dataset lies in the coexistence, within one operational setting of marked contrasts in lithology, intact-rock strength, and surface gradation. That combination makes the dataset suitable for evaluating both the reliability of UAV-based PSD characterization and the sensitivity of the first-order screening outputs developed later in the section (Arrieta and Zhang 2024).

4.2. PHOTOGRAMMETRIC WORKFLOW AND EXTRACTION OF PSD DESCRIPTORS

The workflow adopted in this section transforms aerial RGB imagery into spatially resolved PSD descriptors for coarse mine waste dumps. It comprises four consecutive operations: (i) three-dimensional surface reconstruction, (ii) area selection and discretization, (iii) automatic PSD analysis, and (iv) extraction of representative PSD descriptors from cumulative passing curves. Figure 3 summarizes this sequence. The workflow is not complete when a three-dimensional model has been reconstructed. It is complete only when that model has been converted into PSD descriptors that can be transferred into geotechnical screening (Westoby et al. 2012; Colomina and Molina 2014; Arrieta and Zhang 2024).

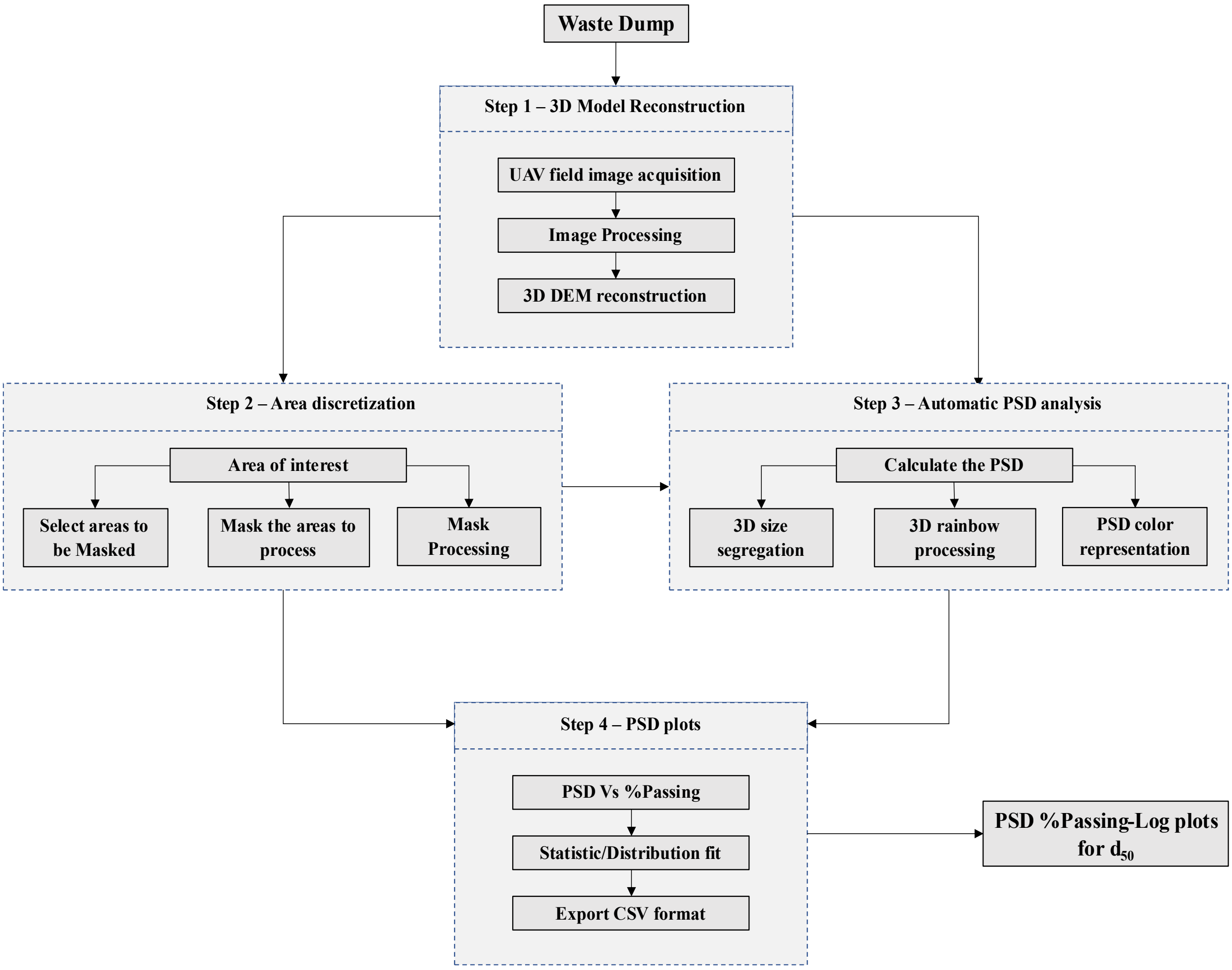

Figure 3. Workflow for field-scale PSD characterization using UAV photogrammetry

Image acquisition was carried out using a lightweight UAV platform equipped with a 12 MP RGB camera. The field procedure comprised flight planning, ground-control placement, and overlapping image collection over the selected dump faces. Across the five dumps, 3,855 photographs were acquired from stand-off distances of approximately 30-120 m, yielding a ground sample distance on the order of 1 cm. These overlapping image sets were processed using Structure-from-Motion photogrammetry to reconstruct georeferenced point clouds and surface meshes of the waste-dump faces. The use of SfM is central because it converts multiple two-dimensional views into a metrically usable three-dimensional representation of the exposed dump surface, which is the required front-end condition for PSD extraction at operational scale (Westoby et al. 2012; Colomina and Molina 2014; Arrieta and Zhang 2024).

The reconstructed surfaces were not treated as homogeneous faces. Each dump was first reduced to an area of interest, and that area was then subdivided into analysis zones and, where required, into smaller subareas. This step is necessary, not cosmetic. A single whole-slope PSD would suppress the heterogeneity generated by end-dumping, segregation, and local surface sorting. Spatial discretization preserves that variability and produces multiple D50 values for each dump rather than one averaged value with limited engineering meaning. Figure 4 illustrates this logic through a discretized waste-dump surface used for local PSD extraction (Arrieta and Zhang 2024).

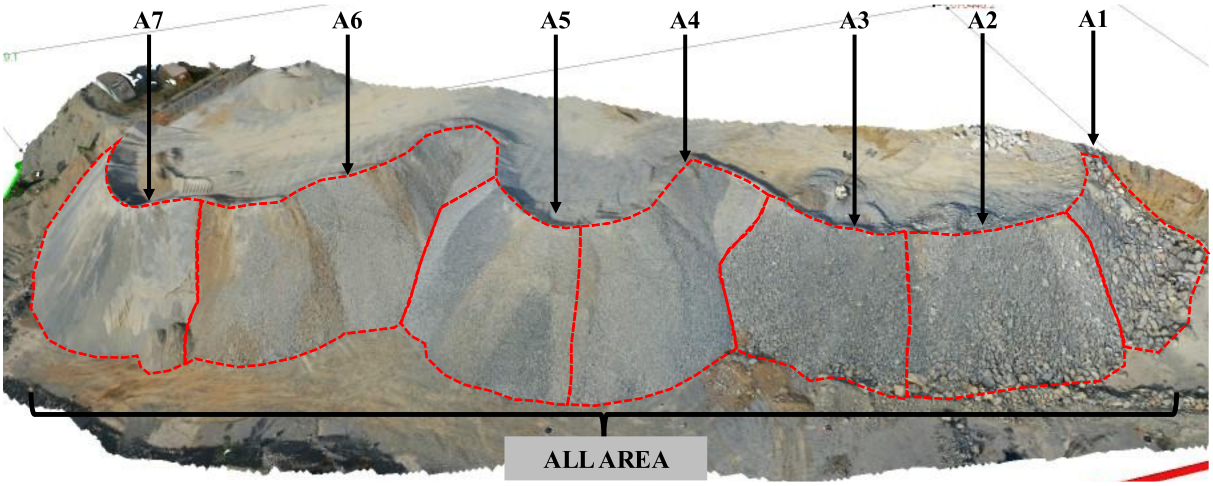

Figure 4. Discretization of a waste-dump surface for local PSD extraction

Automatic PSD analysis was then applied to the selected three-dimensional surfaces. In this stage, the reconstructed model is segmented and processed to calculate particle-size distributions from the visible surface, producing cumulative percentage-passing curves in logarithmic scale and allowing the extraction of characteristic particle sizes. The key descriptor used in this section is D_{50}, defined as the particle size below which 50% of the sampled material volume is smaller. This descriptor is not treated as an isolated number. It is used as the field-scale gradation descriptor that links measured surface state to the first-order shear-strength screening developed later in the section and, through that route, to the pre-failure resistance problem addressed in Section 5 (Arrieta and Zhang 2024).

The workflow is deliberately bounded. It estimates the gradation of the exposed dump face, not the internal grading of the full dump mass. Its strength lies in scale, coverage, and reproducibility. It enables quantitative characterization of large, unsafe, or inaccessible slopes that are poorly served by manual surveys or full-scale sieving. For this dissertation, that is the required threshold: a defensible field-scale state descriptor, not a complete internal reconstruction of the waste dump. The accuracy of that descriptor and the resulting PSD distributions are examined in the next section (Arrieta and Zhang 2024).

4.3. VALIDATION AND SPATIAL VARIABILITY OF PSD

Table 6 and Figure 5 show that the UAV-SfM workflow reproduces field-measured particle size with screening-level accuracy and without a strong systematic offset. Across the five dumps, deviation ratios are 6.9% for WD-1, 5.3% for WD-2, 5.7% for WD-3, 4.4% for WD-4, and 4.7% for WD-5, all below 10%. Mean field and UAV particle sizes differ by only 1-14 mm across the dataset. For dump-scale geotechnical characterization, that agreement is sufficient to treat UAV-derived PSD as a reliable field-scale descriptor of exposed material state (Arrieta and Zhang 2024).

Table 6. Field and UAV particle-size comparison for validation boulders

Site	Method	Number of data sets	Mean Value (mm)	Std	Error (%)
WD-1	Field	10	232	16.9	6.9
	UAV		218	12.3	
WD-2	Field	10	241	43.3	5.3
	UAV		240	42.4	
WD-3	Field	10	205	21.7	5.7
	UAV		199	14.2	
WD-4	Field	10	217	49.9	4.4
	UAV		220	52.5	
WD-5	Field	10	248	41	4.7
	UAV		242	39.1	

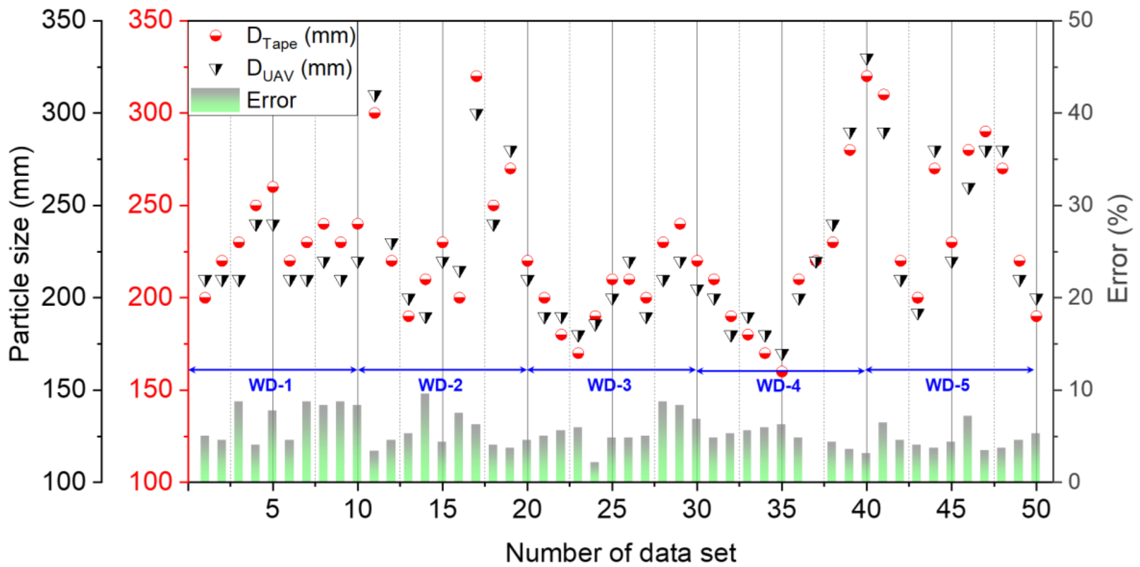

Figure 5. Validation of UAV-derived particle size against field measurements

Once validated, the workflow reveals clear PSD contrasts between the five dumps. Figure 6 shows that WD-4 is the coarsest material in the dataset, WD-2 and WD-3 are the finest, WD-5 is also coarse although less extreme than WD-4, and WD-1 occupies an intermediate position with a broader spread. These contrasts are not cosmetic. They confirm that the method can discriminate materially different dump surfaces at operational scale rather than collapsing the five cases into visually similar PSD trends (Arrieta and Zhang 2024).

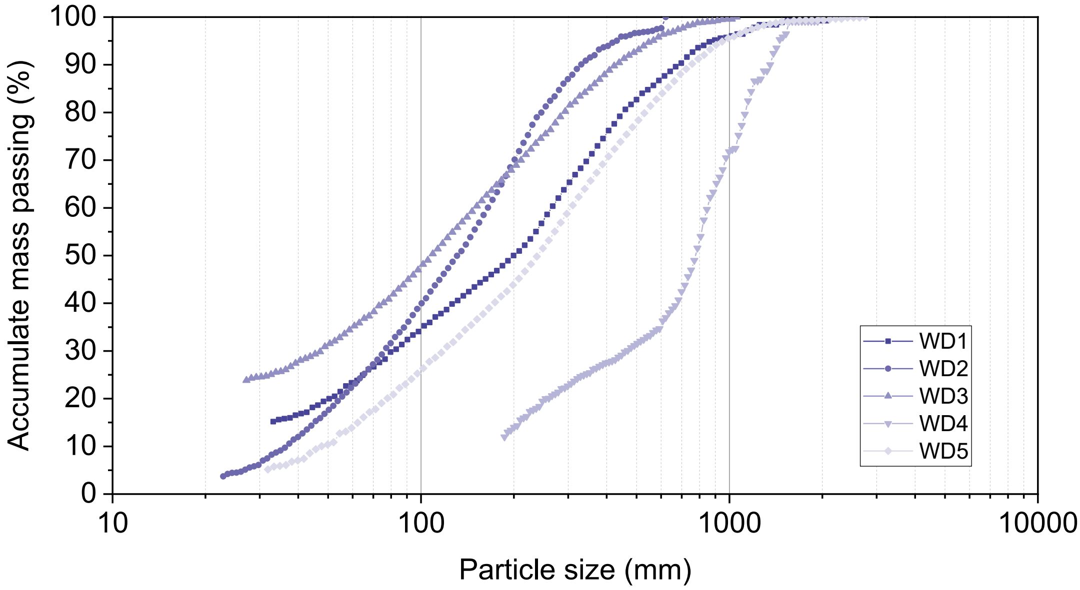

Figure 6. Comparative PSD curves for the five waste dumps

Whole-dump PSD curves are not sufficient for geotechnical use because they suppress the heterogeneity created by end-dumping, segregation, and local surface sorting. That variability becomes explicit when each area of interest is subdivided and multiple D_{50} values are extracted. Figure 7 shows that WD-4 remains consistently coarse across its analyzed sectors, whereas WD-1, WD-2, and WD-5 display wider dispersion and stronger local variability. WD-3 is finer and more compact in its D50 distribution than WD-1 and WD-5. The mean D_{50} values carried forward into Section 4.4 are 117.9 mm for WD-1, 88.6 mm for WD-2, 89.8 mm for WD-3, 770.6 mm for WD-4, and 238.1 mm for WD-5.

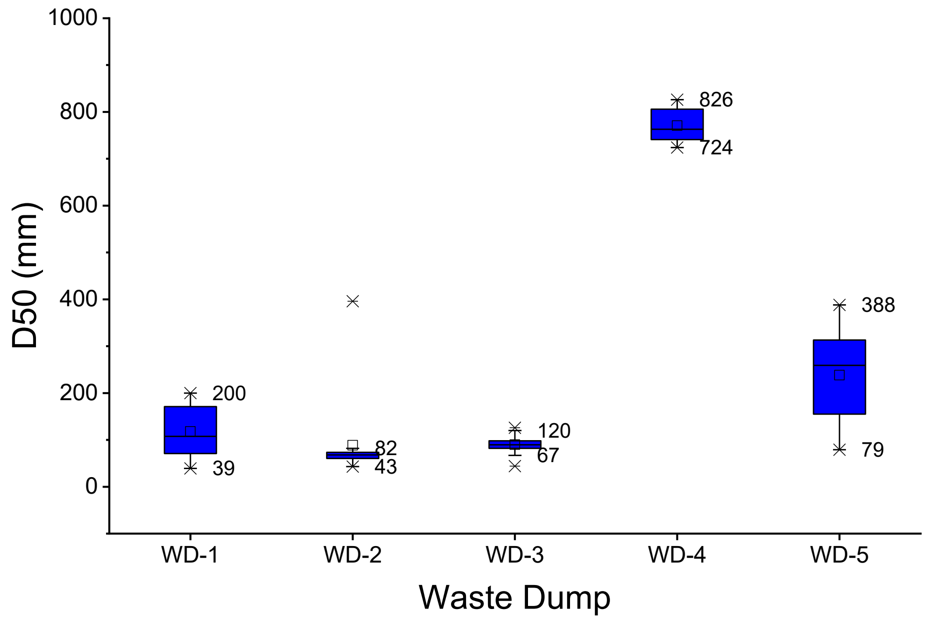

Figure 7. Distribution of D_{50} values from subdivided dump-scale PSD analysis

This section establishes two points. First, UAV-derived PSD is sufficiently reliable to function as a field-scale state descriptor for coarse mine waste dumps. Second, discretized PSD analysis preserves within-dump variability rather than reducing each dump to a single weak average. That result is essential for the next section, where the measured PSD descriptors are translated into first-order pre-failure resistance screening parameters.

4.4. First-order pre-failure resistance screening from measured PSD

Measured PSD acquires geotechnical value only when it is translated into a resistance framework. In this section, that translation is performed at first-order screening level using the Barton-Kjaernsli criterion, selected because it was developed for coarse granular materials and explicitly incorporates particle size through a characteristic diameter. For the present study, the criterion provides a practical route for linking UAV-derived PSD to pre-failure resistance screening where prototype-scale laboratory testing is impractical (Barton and Kjaernsli 1981; Arrieta and Zhang 2024).

The screening equation is written as:

$$\tau = \sigma_n' \tan\left[RLog_{10}\left(\frac{S}{\sigma_n'}\right) + \varphi_b\right] \tag{1}$$

Where τ is shear stress, σ_n' is effective normal stress, φ_b is the basic friction angle, R is the equivalent roughness parameter, and S is the size-dependent equivalent particle strength.

The screening inputs were assigned from measured or defensibly estimated quantities. The representative particle-size descriptor was taken as the mean D_{50} obtained from the subdivided PSD analysis in Section 4.3. The normalized equivalent particle strength (S/σ_c) was assigned from the Barton-Kjaernsli particle-strength chart using the mean D_{50} and the intact-rock strength of each dump, as illustrated in Figure 8.

The basic friction angle φ_b was taken as the mean of the tilt-test results reported for each dump. The roughness parameter R was assigned conservatively by assuming a dump porosity of 25% and particles with smooth to moderately angular surfaces, which yielded values between 6.0 and 6.5 across the five dumps. Table 7 summarizes the resulting screening inputs and outputs. This procedure is deliberately bounded: it is a geotechnical screening translation of measured PSD, not a constitutive calibration exercise.

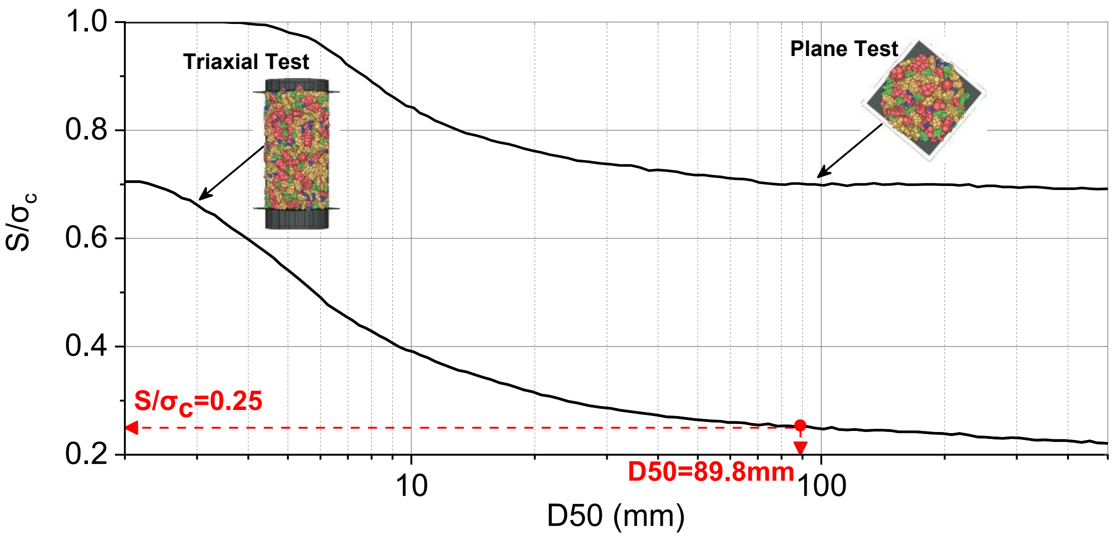

Figure 8. Equivalent particle strength ratio S/σ_c for D_{50}=89.8 mm, modified from the Barton-Kjaernsli particle-strength chart (Barton and Kjaernsli 1981)

Table 7. First-order shear-strength screening inputs and outputs derived from measured PSD

Waste dump	Mean D_{50} (mm)	S/σ_c	Mean φ_b (°)	Assigned R	Reference σ'_n (MPa)	Screened τ (MPa)	Screened ϕ (°)
WD-1	117.9	0.23	26.9	6.1	1.0	0.67	33.9
WD-2	88.6	0.25	30.5	6.4	1.0	0.90	42.1
WD-3	89.8	0.25	26.9	6.0	1.0	0.71	35.3
WD-4	770.6	0.2	31.2	6.3	1.0	0.87	41.1
WD-5	238.1	0.23	31.3	6.5	1.0	0.94	43.3

The reference effective normal stress of 1.0 MPa, Table 7 separates the five dumps into two geotechnically meaningful groups. The weaker carbonaceous mudstone dumps, WD-1 and WD-3, yield screened shear stresses of 0.67 and 0.71 MPa and corresponding screened effective friction angles of 33.9° and 35.3°. The stronger coarse materials, WD-2, WD-4, and WD-5, yield higher screened shear stresses of 0.90, 0.87, and 0.94 MPa and screened effective friction angles of 42.1°, 41.1°, and 43.3°, respectively. These contrasts are not produced by visual classification alone. They arise from measured PSD carried through the Barton-Kjaernsli framework together with site-specific intact-rock strength and basic friction angle. In engineering terms, dump-scale PSD is already functioning here as a meaningful state descriptor rather than as a descriptive appendage.

Figure 9 shows the corresponding nonlinear screening envelopes. The stronger, coarser materials align with the expected range of practical rockfill behavior and remain close to the Leps practice bounds, whereas the weaker carbonaceous mudstone dumps systematically lower. This confirms that UAV-derived PSD is not generating arbitrary screening outputs. It also fixes the boundary of the section. PSD does not explain shear resistance by itself. The lower envelopes of WD-1 and WD-3 reflect finer and weaker gradation together with lower intact-rock strength. Section 4 therefore supports a narrower and stronger claim: measured PSD can be translated into a realistic first-order screening framework whose outcome still depends on material strength and particle roughness (Leps 1970; Barton and Kjaernsli 1981; Arrieta and Zhang 2024).

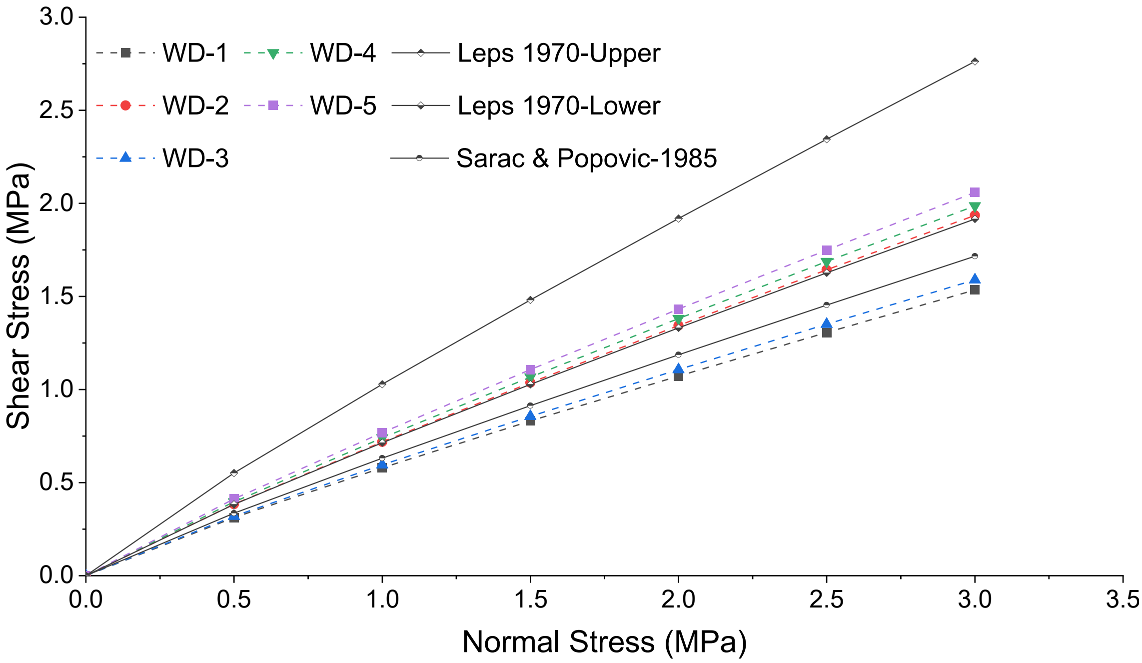

Figure 9. First-order shear-strength screening envelopes derived from measured PSD

This interpretation also clarifies the relative leverage of the screening parameters. For the stronger coarse dumps, variations in the roughness term R exert greater influence on the screened response than the equivalent particle-strength term S. For the weaker mudstone-rich dumps, the influence of S becomes more pronounced because the intact particles themselves are weaker. That result matters for the thesis. Field-scale PSD is a necessary and usable state descriptor, but it is not a complete mechanical description. That is exactly where Section 4 stops and Section 5 begins. Section 4 has shown that PSD can be measured at dump scale and converted into first-order pre-failure resistance screening. Section 5 addresses the harder question: whether that measured state can constrain the structure of stress-dependent resistance representation more systematically.

4.5. SECTION SYNTHESIS, LIMITS, AND TRANSITION TO SECTION 5

Section 4 resolves the first analytical level of the dissertation: material state. Across the five waste dumps, the UAV-SfM workflow reproduced field-measured particle sizes with deviation ratios below 10%, captured strong contrasts in whole-dump PSD and local D_{50} variability, and provided the gradation descriptors required for first-order screening through the Barton-Kjaernsli criterion. The section therefore converts exposed dump faces from visually interpreted surfaces into quantified material-state information suitable for engineering use (Barton and Kjaernsli 1981; Arrieta and Zhang 2024).

The section also fixes an essential engineering boundary. Measured PSD does not explain shear resistance by itself. The screening outputs remain sensitive to particle roughness and intact-rock strength, particularly when weaker carbonaceous mudstone materials are compared with stronger coarse rocky dumps. This is why Section 4 remains a first-order screening study rather than a constitutive modeling section. The translation from measured PSD to resistance is still empirical and depends on assumptions regarding porosity, particle roughness, and equivalent particle strength. The resulting envelopes are useful for preliminary geotechnical interpretation, but they are not substitutes for calibrated laboratory or site-specific resistance models where design-level prediction is required (Barton and Kjaernsli 1981; Arrieta and Zhang 2024).

The limits of the section are equally clear. The workflow characterizes exposed surface state and does not reconstruct the internal grading of the full dump mass. The empirical basis is restricted to five waste dumps from one mining operation, and the strength translation is bounded by the assumptions built into the Barton-Kjaernsli framework. These constraints define the exact contribution of the section rather than weaken it: field-scale gradation can be measured reliably enough to function as a defensible state descriptor in coarse mine waste engineering. That boundary defines the transition to Section 5. Section 4 has shown that pre-shear gradation can be measured at realistic scale and transferred into first-order resistance screening. Section 5 addresses the next and harder question: whether that measured state can constrain curvature in stress-dependent shear-strength representation and thereby reduce arbitrariness in nonlinear calibration.

5. PRE-FAILURE RESISTANCE: PSD-CONSTRAINED CURVATURE IN STRESS DEPENDENT SHEAR-STRENGTH REPRESENTATION

Section 5 resolves the second analytical level of the dissertation: pre-failure resistance. Section 4 established that PSD can be measured at realistic scale as a defensible state descriptor. The transition is analytical, Section 4 defines measurable state, whereas Section 5 evaluates how that state enters stress-dependent resistance calibration. Section 5 now asks the harder question: whether pre-shear PSD can do more than populate first-order screening inputs and instead constrain curvature in stress-dependent shear-strength representation for rockfills and waste-rock materials. Built mainly on the appended manuscript, the section evaluates a PSD-constrained route within an existing power-law envelope family (Arrieta and Zhang 2024, 2026).

5.1. CURVATURE AS THE UNRESOLVED CALIBRATION PROBLEM IN PRE-FAILURE RESISTANCE

The unresolved mechanics problem is not whether curved envelopes should be used. For rockfills and waste-rock materials, curved strength envelopes are the expected response of coarse granular systems as particle rearrangement, dilation, confinement, and breakage modify the load-bearing structure with increasing stress (Newland and Allely 1957; Leps 1970; Indraratna et al. 1993, 1998; Indraratna 1994). Power-law forms are therefore already established in engineering practice. The unresolved issue is narrower and more precise: how curvature should be defined in a way that remains mechanically interpretable across gradation states and observed stress windows (Gonzalez 1985).

In existing power-law formulations, the curvature exponent m is commonly obtained by regression from triaxial data. Because m controls the rate at which shear strength increases with effective normal stress, a fitted value can reflect the calibration window more strongly than the declared material state when the stress range is narrow, uneven, or strongly weighted toward one part of the response field. The result is curvature that may be numerically convenient but mechanically weak. The central question of the section is therefore exact: can curvature be constrained from pre-shear

PSD rather than left to free fitting against the triaxial response alone? (Tang et al. 2016; Xu and Xu 2021).

A direct constraint based on particle morphology may appear attractive, but it is difficult to defend at engineering scale. Common descriptors such as roundness, sphericity, and aspect ratio are often derived from limited size fractions, depend on imaging method and operator decisions, and do not transfer cleanly across datasets, laboratories, and sampling scales. In coarse granular materials, size, shape, and breakage effects are also entangled, which further weakens any attempt to use morphology alone as a robust cross-study constraint on curvature. For that reason, this section does not pursue a morphology-based curvature law. It pursues a reproducible descriptor derived from the pre-shear PSD itself (Hryciw et al. 2016; Ovalle and Dano 2020; Deiminiat and Li 2022; Beemer et al. 2022).

In the present framework, that descriptor is D, a finite-window PSD-scaling descriptor estimated from the cumulative pre-shear gradation over an explicitly declared size window. Its role is narrow and must remain narrow. In this section, D does not denote D_{50}, it is not a particle-shape metric, and it is not presented as a complete structural state variable. It is used only as a reproducible descriptor of PSD scaling for the declared pre-shear state. That boundary matters because PSD scaling in granular media is meaningful only over explicit size domains rather than across the full particle-size range. Section 5 therefore evaluates a finite-window route within an existing envelope family, not a universal fractal material law.

Within this bounded setting, this section evaluates whether curvature in an existing stress-dependent power-law envelope can be assigned from pre-shear PSD scaling, leaving only the strength level to be obtained from peak-state triaxial data. Table 8 positions this route relative to the principal power-law formulations considered in this section and shows exactly where the present approach differs from free-fitted curvature forms, fractal-exponent forms, and anchor-normalized envelopes. The scope is restricted to pre-shear PSDs, peak-state triaxial compression, and the observed database stress range. Direct shear, residual-state response, cyclic loading, and post-shear PSD evolution are outside the analysis. That boundary is not a weakness. It is the condition that makes the section defensible.

Table 8. Power-law shear-strength envelopes and how curvature is assigned in Section 5

Criterion	Mathematical Form	Required inputs beyond τ, σ_n	Quantities to determine for use	Reference
Generic power law envelope	$\tau = A\sigma_n^b$	- None	- A, and b, from shear-strength data.	(De Mello 1977; Charles and Watts 1980)
Fractal exponent power law	$\tau = a\sigma_n^{\frac{D}{3}}$	- D, based on PSD scaling.	- $a = k^{\frac{D}{3}} \cdot l^{\frac{(6-2D)}{3}}, b = \frac{D}{3}$ - a and b, coefficients, from shear-strength data.	(Xu et al. 2015; Cylwik et al. 2025)
Anchor parameterized power law envelope	$\tau = \tan(\phi_1')(10p_a)^{1-m}\,\sigma_n^m$	- p_a, normalization.	- $\phi_1' = \phi_{e=0}' - \omega \cdot e$ - m and ω, from shear-strength data.	(Cylwik et al. 2025)
PSD-constrained anchor power-law calibration route	$\tau = \tan(\phi_1')(10p_a)^{1-\frac{D}{3}}\,\sigma_n^{\frac{D}{3}}$	- p_a, normalization. - D finite-window pre-shear PSD-scaling descriptor. - Adopted closure $m = D/3$	- ϕ_1', calibrated from triaxial response	This study

5.2. From pre-shear PSD to a curvature-constrained envelope

This section defines the method core of Section 5, how declared pre-shear gradation enters stress-dependent pre-failure resistance representation. The route is deliberately narrow. A finite-window PSD-scaling descriptor D is estimated from the pre-shear gradation, D is used to assign the curvature exponent m, and the remaining unknown is reduced to the anchor strength level. In this section, D denotes a PSD-scaling descriptor, not a characteristic particle size such as D_{50}. (Turcotte 1986; Bittelli et al. 1999; Arrieta and Zhang 2026). This is also the point at which Section 5 separates itself from free curvature fitting. Table 8 has already positioned the proposed route inside an existing power-law envelope family. The task here is not to introduce a new constitutive family, but to state explicitly how curvature is assigned independently of the triaxial fit while keeping the formulation within a bounded calibration framework (Arrieta and Zhang 2026).

The PSD descriptor is defined over a finite retained window, not over the full reported particle-size range. In the admitted database, that window is fixed to the central $d_{10} - d_{90}$ interval of the pre-shear PSD. Within this window, the cumulative mass fraction finer is written in normalized finite-window form as:

$$P(\leq d\,) \equiv \frac{M(\leq d)}{M_T} = \frac{d^{3-D} - d_L^{3-D}}{d_U{}^{3-D} - d_L^{3-D}}, d \in [d_L, d_U] \quad (2)$$

Where d_L and d_U are the lower and upper bounds of the retained fitting window. This formulation matters because it avoids the false claim that PSD scaling holds over the full-size domain. It states exactly what is being scaled and exactly where that scaling is admitted (Turcotte 1986; Bittelli et al. 1999; Arrieta and Zhang 2026).

When the lower-bound contribution is negligible over the retained points, the straight-line approximation is used, and the PSD-scaling descriptor follows from the fitted log-log slope s as:

$$D = 3 - s \quad (3)$$

Otherwise, D is obtained by direct fitting of Eq. 2 over the same retained window. Because power-law exponents fitted over finite empirical ranges can be sensitive to fitting method and available data format, D is used here only as an operational finite-window PSD-scaling descriptor. The admitted sources provide published cumulative gradation curves rather than raw particle-count samples, so the procedure is not treated as a formal power-law distribution test. Consequently, D is not used as proof of a unique scale-invariant material constant, a full-range fractal property, or a particle-shape metric (Clauset et al. 2009; Ali and Kikumoto 2025).

Once D has been estimated, the formulation remains within the established unit-normalized power-law envelope class rather than introducing a new constitutive family. The baseline normalized envelope is:

$$\tau = K p_a \left(\frac{\sigma_n}{p_a}\right)^m \quad (4)$$

Where K is a dimensionless strength coefficient, m is the curvature exponent, and p_a is the reference atmospheric pressure used only for normalization. The normalization is not cosmetic. It removes unit dependence from the strength coefficient and preserves comparison across datasets expressed in the same stress-normalized form (Duncan and Chang 1970; Yu et al. 2020; Cylwik et al. 2025).

To separate strength level from curvature, an anchor secant friction angle is defined at the reference normal stress $\sigma_n = 10p_a$ as:

$$\tan(\phi_1') \equiv \frac{\tau}{\sigma_n}\Big|_{\sigma_n=10p_a} \tag{5}$$

Which leads to the anchor-parameterized envelope:

$$\tau = \tan(\phi_1')\,(10p_a)^{1-m}{\sigma_n}^m \tag{6}$$

In this form, ϕ_1' carries the strength level at the anchor stress, while m governs the stress sensitivity away from that anchor. That separation is essential. It is what makes curvature assignment independent of the triaxial fit and leaves only the level parameter to be estimated from the response.

In the revised formulation, $D/3$ is first treated as a normalized PSD count-scaling descriptor relative to a three-dimensional reference count. The equality $m = D/3$ is then adopted as a first-order, no-extra-parameter PSD-to-curvature closure within the selected power-law envelope family. It is not treated as a theorem of PSD mass balance, not as a unique PSD-to-curvature law, and not as a universal constitutive exponent.

The adopted PSD-to-curvature closure is then:

$$m = \frac{D}{3} \tag{7}$$

Which yields the closed-form PSD-constrained envelope:

$$\tau = \tan(\phi_1')\,(10p_a)^{1-\frac{D}{3}}{\sigma_n}^{\frac{D}{3}} \tag{8}$$

This equation is the center of Section 5. It keeps the formulation inside an existing power-law envelope family but removes free curvature fitting. Curvature is assigned through the adopted $m = D/3$ closure, and only the anchor strength level remains to be obtained from the triaxial response. In this framework, m is the logarithmic normal-stress sensitivity exponent of the selected envelope, not a universal constitutive exponent law (Arrieta and Zhang 2026).

With D fixed from the pre-shear PSD, the remaining unknown is ϕ_1'. It is obtained from a one-parameter least-squares fit through the origin over the admitted peak-state triaxial tangency pairs $(\sigma_{n,i}, \tau_i)$ as:

$$\tan(\phi_1') = (10p_a)^{\frac{D}{3}-1} \left(\frac{\sum_{i=1}^{N} \tau_i \sigma_{n,i}^{\frac{D}{3}}}{\sum_{i=1}^{N} \sigma_{n,i}^{2\cdot\frac{D}{3}}} \right) \tag{9}$$

For the present Section, these pairs are interpreted at peak-state triaxial tangency rather than through a Mohr-Coulomb plane transformation. The full Mohr-circle tangency reduction is retained in the appended manuscript and is not repeated line-by-line here, because it does not change the central logic of the route: once D is specified, the envelope becomes a one-parameter fit in ϕ_1' under the adopted peak-state triaxial interpretation (Arrieta and Zhang 2026).

Three boundaries follow directly from this formulation. First, the route is defined for pre-shear PSD only; post-shear PSD evolution is excluded. Second, the route is defined for peak-state triaxial compression only; direct shear, residual-state response, and cyclic loading are outside scope. Third, the assigned D remains a descriptor of PSD scaling over the retained $d_{10} - d_{90}$ window; it is not a substitute for density, fabric, breakage evolution, or particle shape. These are not weaknesses. They are the conditions that keep the formulation interpretable and make this section defensible. Section 5.3 now tests this bounded route against the admitted triaxial database as a route comparison, not as an external predictive-validation exercise.

5.3. Admitted evidence base and route-comparison protocol for the PSD-constrained route

Section 4 established that PSD can be measured at realistic scale as a defensible descriptor of material state. Section 5 now tests whether the same class of pre-shear state information can constrain curvature in stress-dependent shear-strength representation when the evidence is expanded beyond one site to a compiled triaxial database. The purpose of this section is therefore not universal validation. It is to define the admitted evidence base and the comparison protocol by which the PSD-constrained route is examined across published peak-state triaxial evidence.

The evidence base was assembled from published large-scale triaxial compression tests on rockfills and waste-rock materials that reported pre-shear PSDs together with effective-stress data at a clearly defined peak state. After application of the admissibility criteria, the database retained

42 published studies, 1005 admitted triaxial compression data points, and 181 distinct pre-shear PSD-defined cases. This distinction is critical. The 1005 data points define the stress-response field. The 181 cases define the pre-shear gradation states from which the PSD-scaling descriptor D is estimated. The units of inference of the section are therefore case-wise, not point-wise. Table 9, Table 10, and Figure 10. summarize the scope of the admitted evidence base.

The admitted database spans a broad engineering range. Apparatus diameters vary from 50.0 to 1130.3 mm, effective confining stresses σ_3' from 0.001 to 4.482 MPa, tangency normal stresses σ_n from 0.008 to 10.534 MPa, and peak shear stresses τ from 0.002 to 9.728 MPa. The reported materials are predominantly coarse-grained, with median particle sizes from 0.3 to 109.7 mm and maximum particle sizes from 1.4 to 454.0 mm. The apparatus diameter range, from 50.0 to 1130.3 mm, is retained as part of the admitted evidence domain rather than corrected as an independent scale-effect term. Accordingly, the route comparison is interpreted within the reported apparatus-size, PSD, and stress ranges, not as scale-independent validation.

Table 9. Composition of the admitted triaxial database by apparatus class, lithology, and geographic origin

Category	Descriptor	Count	%
Apparatus diameter class	Small (D_s <100 mm)	68	6.80%
	Medium (100 ≤ D_s < 300 mm)	331	32.90%
	Large (300 ≤ D_s < 1000 mm)	435	43.30%
	Super large (D_s ≥1000 mm)	171	17.00%
Lithology	Sedimentary	176	17.50%
	Igneous	331	32.90%
	Metamorphic	332	33.00%
	Alluvial/unconsolidated granular	166	16.50%
Geographic	Americas	301	30.00%
	Asia	330	32.80%
	Australia	89	8.90%
	Europe	37	3.70%
	Not reported	248	24.70%

Table 10. Descriptive statistics of the admitted triaxial database

Variable	Symbol	Unit	Minimum	Mean	Median	Maximum	Standard deviation
Apparatus diameter	D_S	mm	50.0	409.9	300.0	1130.3	336.4
Size ratio	D_S/D_{max}	-	0.7	9.9	5.9	500.0	30.2
Effective confining stress	σ_3'	MPa	0.001	0.733	0.414	4.482	0.846
Tangency normal stress	σ_n	MPa	0.008	1.024	0.677	10.534	1.155
Peak shear stress	τ	MPa	0.002	1.324	0.854	9.728	1.351
Maximum particle size	D_{max}	mm	1.4	69.5	51.0	454.0	61.6
Median particle size	D_{50}	mm	0.3	20.1	8.5	109.7	25.6
Gravel fraction	Gravel	%	0.0	77.0	79.9	100.0	19.6
Sand fraction	Sand	%	0.0	19.3	18.2	92.7	16.6
Fines fraction	Fines	%	0.0	3.7	0.7	48.3	7.3
Initial void ratio	e_i	-	0.16	0.40	0.36	0.89	0.14

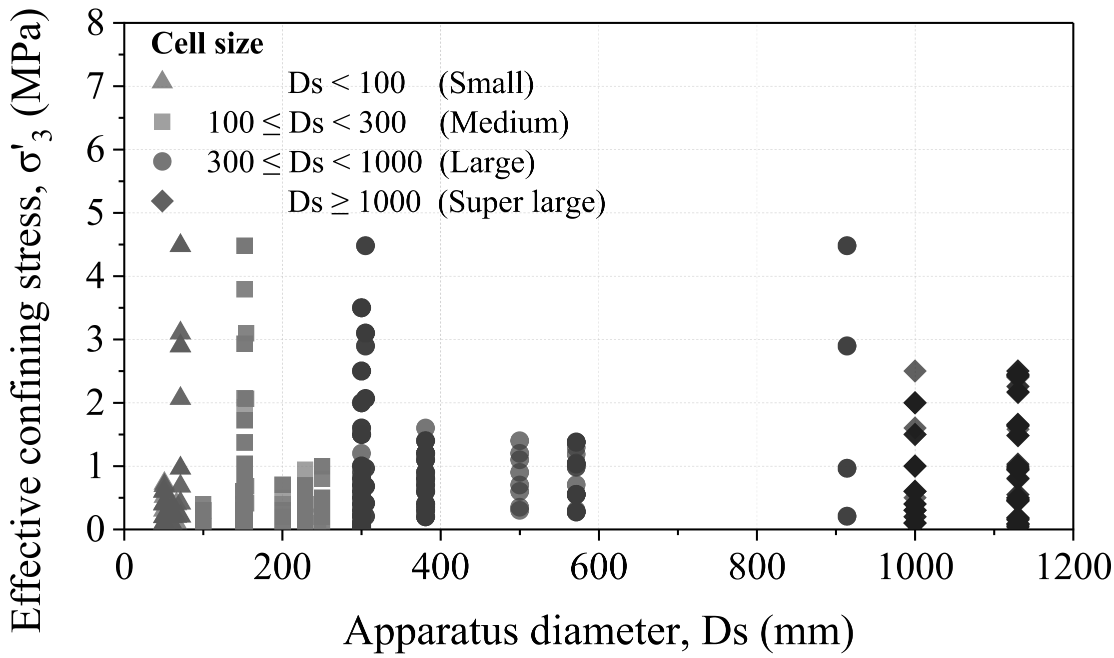

Figure 10. Coverage of the admitted triaxial evidence base

Lithologic coverage includes sedimentary, igneous, metamorphic, and alluvial or unconsolidated granular materials. A unified engineering material classification was not imposed because the source studies do not report labels consistently enough to support one defensible cross-study scheme. For that reason, the database is described through apparatus-size class, lithologic origin, and reported geographic origin, which are the most consistently documented attributes across the admitted studies.

Admissibility was deliberately strict. A dataset was retained only when it provided:

1. Pre-shear PSD with sufficient resolution to define a retained fitting window and estimate D.
2. Effective principal stresses σ_1' and σ_3' at peak failure;
3. A clearly identified peak failure state applied consistently within the reported subset.
4. Reporting conditions clear enough to support effective-stress interpretation.
5. Direct shear datasets were excluded. Post-shear-only gradations were excluded.

Datasets with incomplete PSD information, ambiguous failure-state definitions, or duplicate publication of the same test series were also excluded; where duplication occurred, the most complete source was retained. These criteria are not procedural decoration. They define the boundary within which the PSD-constrained route can be examined without mixing incompatible material states, failure conventions, or stress interpretations. Only pre-shear PSDs were used. Reported gradations were compiled from published tables when available and digitized from published cumulative curves when tabulated values were absent. When digitization was necessary, points were sampled densely enough within the retained fitting window to reproduce the published curve smoothly. These sampled points are not new measurements. They are reconstructions of the reported PSD shape required for estimation of D.

For consistency across studies, the retained scaling window was fixed to the central $d_{10} - d_{90}$ interval of each compiled pre-shear PSD, provided that the reported resolution within that interval was sufficient to support stable estimation. The cumulative curve was then restricted to that window and linearly renormalized to satisfy the finite-window conditions defined in Section 5.2. This is a standardization choice for cross-study comparison, not a claim that the d_{10}–d_{90} interval is the unique optimal scaling window for every material.

Once D had been estimated for each admitted PSD-defined case, the proposed route was evaluated case by case. The curvature exponent was assigned through the mapping $m = D/3$, and the remaining strength-level parameter was obtained from the one-parameter least-squares expression defined in Section 5.2 using the peak-state triaxial tangency coordinates $(\sigma_{n,i}, \tau_i)$. In parallel, an unconstrained reference route was evaluated on the same admitted triaxial source data using conventional triaxial interpretation and free fitting of the curvature exponent.

The two routes were kept separate throughout the evaluation. The reference route used fitted curvature under its own stress-reduction convention. The proposed route used PSD-assigned curvature and the tangency-based interpretation defined in Section 5.2. This distinction matters because the comparison is not a strict like-for-like optimization contest in one common coordinate space. It is a case-wise comparison of two internally consistent routes applied to the same admitted triaxial evidence. The valid inference is therefore route-level calibration discipline across admitted cases, not external predictive validation or universal constitutive generalization. Section 5.4 now tests that route in response space.

5.4. Response-space performance of the PSD-constrained route

Sections 5.2 and 5.3 fixed the formulation and the admitted evidence base. This section evaluates the response-space consequence of replacing freely fitted curvature with PSD-constrained curvature across the admitted database. The test is performed on the same 181 PSD-defined cases and the same admitted peak-state triaxial source data. The result is a route comparison under a fixed evidence base, not an external predictive-validation exercise (Arrieta and Zhang 2026).

Table 11 shows that the admitted database spans a broad and mechanically meaningful range of PSD-defined curvature states. The estimated PSD-scaling descriptor D ranges from 1.30 to 2.88, with mean 2.40 and median 2.49. The assigned curvature exponent $m = D/3$ therefore ranges from 0.43 to 0.96, with mean 0.80 and median 0.83. The database does not collapse into one narrow curvature class. It carries a real spread of gradation states and a real spread of PSD-constrained curvature states.

The lower end of this distribution, $D = 1.30$, corresponds to $m_{PSD} = 0.43$ under the adopted $m = D/3$ closure. This value is interpreted only as the lower tail of the finite-window $d_{10} - d_{90}$ PSD-scaling descriptor. Within the adopted power-law route, it assigns lower logarithmic normal-stress sensitivity and stronger envelope concavity; it is not treated as a separate material class, a particle-shape measure, or evidence of full-range fractal scaling.

Table 11. Summary statistics of estimated D and assigned curvature exponent m across 181 admitted PSD-defined cases

Quantity	Symbol	Minimum	Mean	Median	Maximum	Standard deviation
PSD-scaling descriptor	D	1.30	2.40	2.49	2.88	0.29
Curvature parameter	m	0.43	0.80	0.83	0.96	0.10

Table 12 and Figure 11 summarize the curvature-space comparison between PSD-assigned curvature and fitted-reference curvature. The signed curvature deviation Δm has mean -0.03 and median -0.03, while the absolute deviation $|\Delta m|$ has mean 0.11 and median 0.08. These statistics indicate a small average negative shift and modest typical mismatch. Figure 11 is not interpreted as evidence of a pointwise predictive relationship between m_{PSD} and m_{fit}; the scatter around the 1:1 line is part of the route comparison and is summarized by Δm and $|\Delta m|$. The response-space consequences of this curvature substitution are evaluated in Table 13 to Table 15.

Table 12. Summary statistics of signed and absolute curvature deviation across 181 admitted PSD-defined cases

Quantity	Symbol	Minimum	Mean	Median	Maximum	Standard deviation
Signed curvature deviation	$\triangle m$	-0.43	-0.03	-0.03	0.47	0.14
Absolute curvature deviation	$\|\triangle m\|$	0.00	0.11	0.08	0.47	0.00

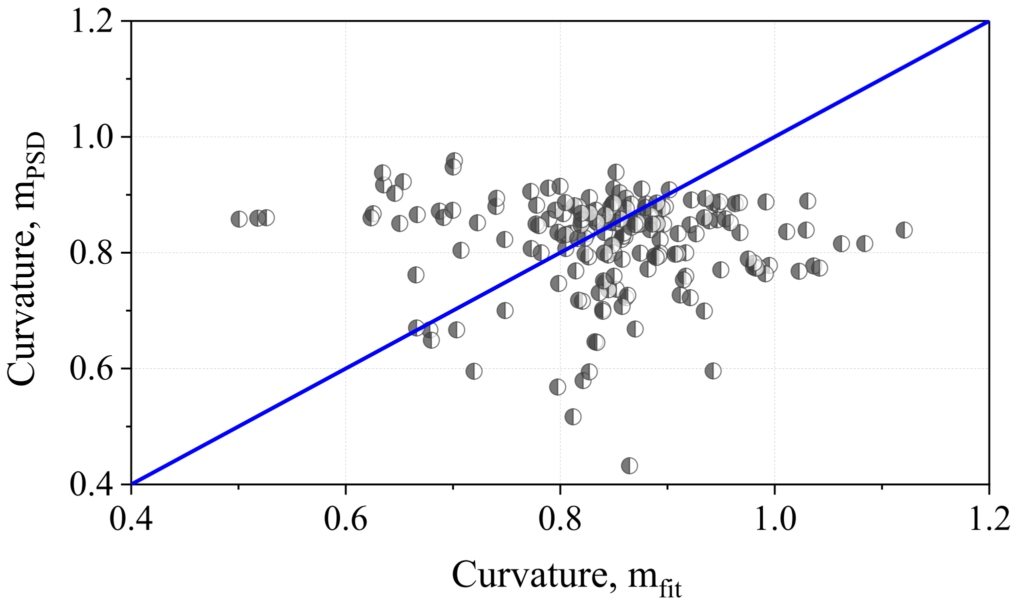

Figure 11. Curvature-space comparison between fitted curvature exponent and PSD-constrained curvature exponent across 181 admitted PSD-defined cases.

The main route-comparison result lies in response space, not curvature space. Under the adopted within-database comparison protocol, Table 13 shows lower central route-to-observed discrepancy for the PSD-constrained route. Median MAE decreases from 0.24 to 0.06 MPa, median RMSE from 0.26 to 0.07 MPa, and median Bias from 0.24 to 0.06 MPa under the adopted sign convention. The same direction is observed in the mean values: MAE decreases from 0.56 to 0.21 MPa, RMSE from 0.62 to 0.23 MPa, and Bias from 0.56 to 0.19 MPa. These values are interpreted as within-database route-comparison metrics, not as external predictive-validation statistics.

Table 13 shows the distribution of case-wise RMSE differences. Negative values indicate lower RMSE for the PSD-constrained route. The distribution is shifted toward negative values, indicating that lower RMSE is common across the admitted case set, although the route does not improve every case. Table 13 also shows a reduced upper-error range: the standard deviation of RMSE decreases from 1.74 to 0.86 MPa, and the maximum RMSE decreases from 15.35 to 8.00 MPa. The remaining 8.00 MPa maximum shows that upper-tail residuals still exist. The supported conclusion is therefore bounded: the PSD-constrained route lowers central response discrepancy and reduces the upper-error range within the admitted database, but it does not eliminate all high-error cases.

Table 13. Case-wise response-space errors for fitted and PSD-constrained routes across 181 admitted comparison cases

Quantity	Symbol	Minimum	Mean	Median	Maximum	Standard deviation
MAE, reference fitted route	$MAE_{\tau,fit}$	0.03	0.56	0.24	13.56	1.60
MAE, proposed PSD-constrained route	$MAE_{\tau,PSD}$	0.00	0.21	0.06	6.93	0.75
Casewise MAE difference	ΔMAE_{τ}	-9.98	-0.36	-0.17	0.53	0.94
RMSE, reference fitted route	$RMSE_{\tau,fit}$	0.03	0.62	0.26	15.35	1.74
RMSE, proposed PSD-constrained route	$RMSE_{\tau,PSD}$	0.00	0.23	0.07	8.00	0.86
Casewise RMSE difference	$\Delta RMSE_{\tau}$	-9.82	-0.39	-0.18	0.51	0.98
Bias, reference fitted route	$Bias_{\tau,fit}$	0.03	0.56	0.24	13.56	1.60
Bias, proposed PSD-constrained route	$Bias_{\tau,PSD}$	-0.17	0.19	0.06	6.93	0.75
Casewise Bias difference	$\Delta Bias_{\tau}$	-9.98	-0.37	-0.18	0.07	0.93

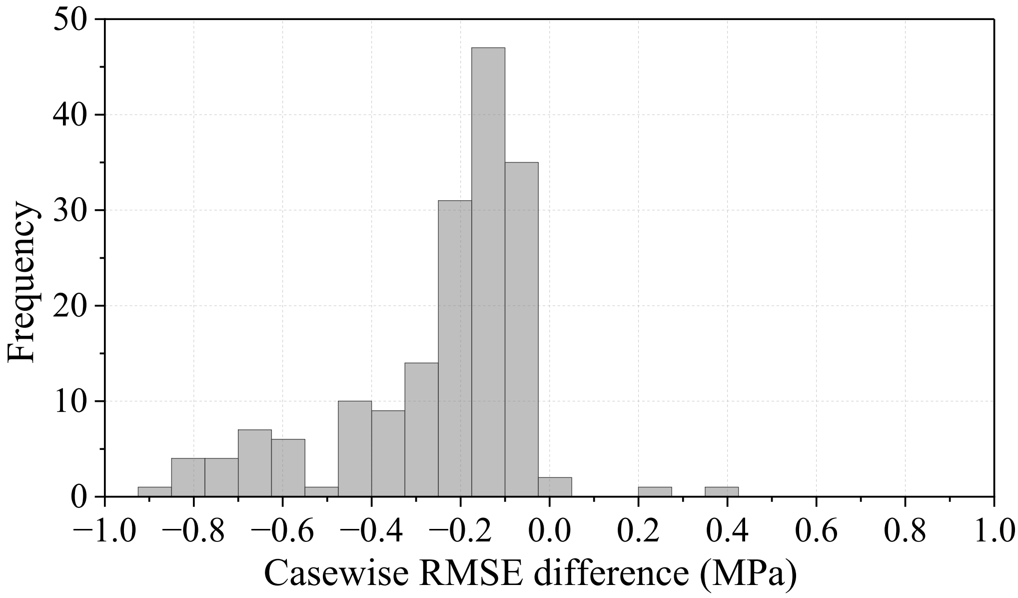

Figure 12. Distribution of case-wise $\Delta RMSE_{\tau}$ across 181 admitted comparison cases.

Table 14 and Figure 13 compare the PSD-constrained route against the fitted-reference response. The median PSD-fit $MAE_{\tau,PSD-fit}$ and $RMSE_{\tau,PSD-fit}$ are 0.18 and 0.19 MPa, respectively, indicating limited central departure from the fitted-reference route. The maximum $MAE_{\tau,PSD-fit}$ and $RMSE_{\tau,PSD-fit}$ are 9.98 and 10.13 MPa, respectively, showing that a high-error upper tail remains. No post-hoc outlier elimination is applied, because the cases satisfy the admissibility criteria defined in Section 5.3. These high-error cases are retained as part of the admitted comparison domain and are interpreted as upper-tail route departures rather than removed from the analysis. Figure 13 shows that the largest departures occur mainly at higher fitted-reference shear-stress levels, where curvature has the strongest leverage on response amplification.

Table 14. Case-wise PSD-to-fitted response deviation across 181 admitted comparison cases [+]

Quantity	Symbol	Minimum	Mean	Median	Maximum	Standard deviation
MAE, PSD-fit	$MAE_{\tau,PSD-fit}$	0.02	0.38	0.18	9.98	0.94
RMSE, PSD-fit	$RMSE_{\tau,PSD-fit}$	0.02	0.41	0.19	10.13	1.00
Bias, PSD-fit	$Bias_{\tau,PSD-fit}$	-0.07	0.37	0.18	9.98	0.93

[+]$Bias_{\tau,PSD-fit}$ is included only as a supplementary directional comparison metric relative to the fitted reference; interpretation remains secondary to $MAE_{\tau,PSD-fit}$ and $MAE_{\tau,PSD-fit}$.

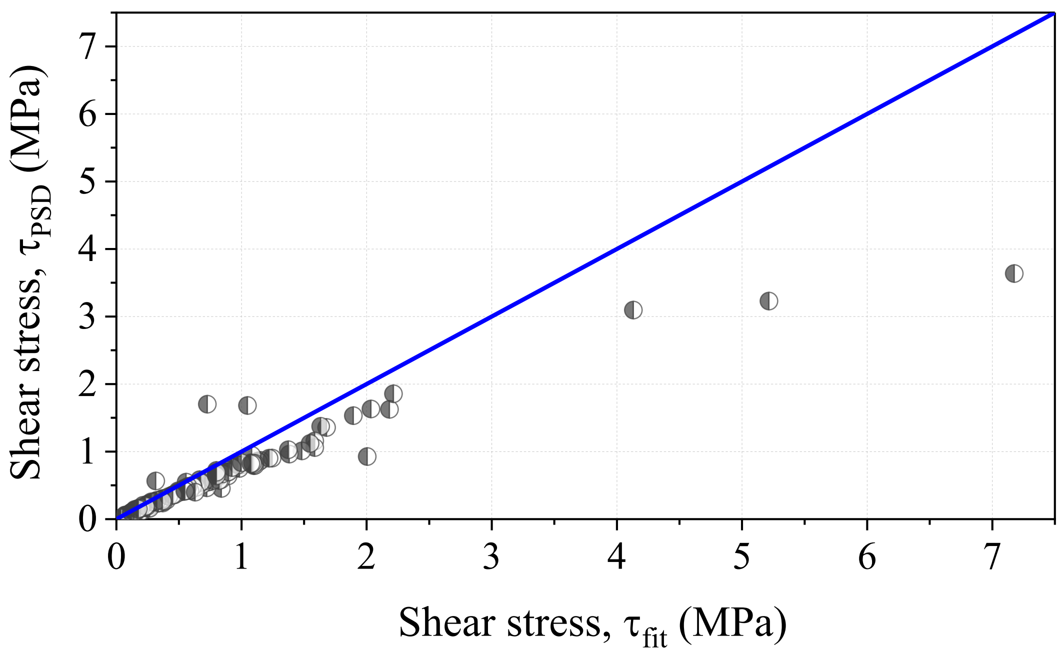

Figure 13. PSD-route shear stress versus fitted-reference shear stress.

The reliability limit of the route is equally clear. It is not controlled by curvature substitution alone. Table 15 shows that response penalties remain rare in every absolute curvature-deviation class. For $|\ \Delta m\ | \leq 0.10$, the median ΔRMSE is −0.20 MPa, and 98% of cases retain non-positive penalty. For $0.10 < |\ \Delta m\ | \leq 0.20$, the median ΔRMSE is −0.15 MPa and again 98% of cases retain non-positive penalty.

For | Δm |> 0.20, the median ΔRMSE remains −0.19 MPa and 100% of cases retain non-positive penalty. Figure 14 confirms the same point: penalty cases are sparse, and they do not organize themselves along a monotonic threshold in Δm. Large curvature substitution therefore does not by itself define failure of the PSD route. The remaining departures are governed mainly by the upper-stress region, where curvature has its strongest leverage on response growth.

Table 15. Response penalty by absolute curvature-deviation class.

Curvature deviation class	Number of cases	Median $\Delta RMSE_\tau$ (MPa)	Cases with $\Delta RMSE_\tau \leq 0$ (%)
Negligible change (≤ 0.10)	109.00	-0.20	98%
Moderate change (0.10-0.20)	41.00	-0.15	98%
Significant change (>0.20)	31.00	-0.19	100%
Total	181.00	---	---

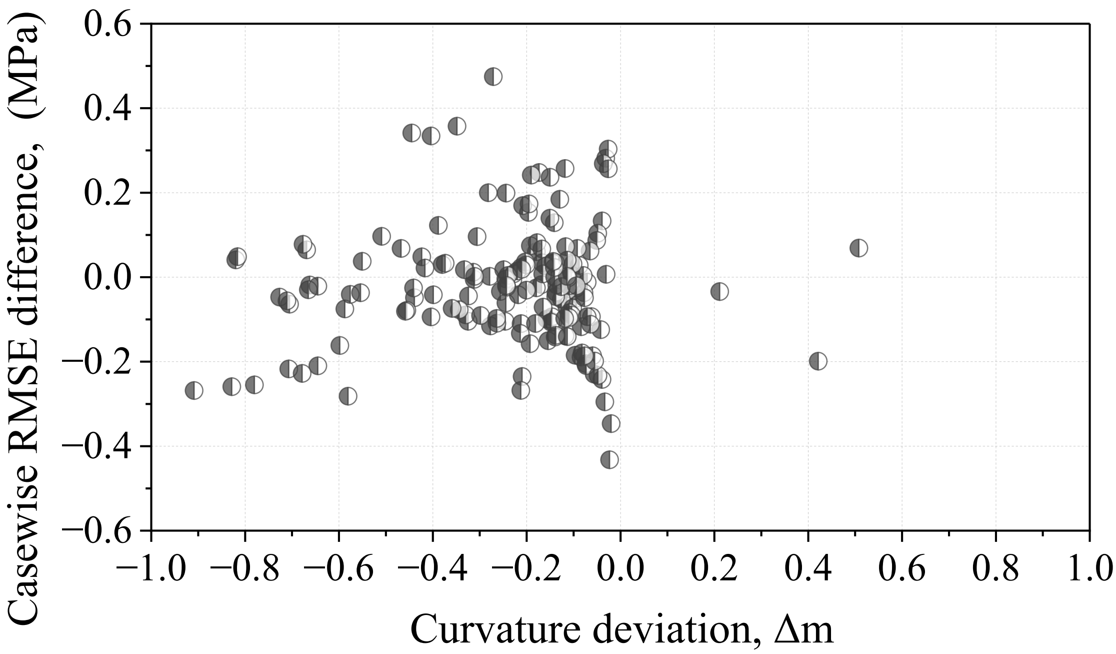

Figure 14. Case-wise RMSE difference versus curvature deviation.

This section establishes a direct result. Within the observed domain of pre-shear PSDs and peak-state triaxial envelopes. Under the adopted within-database route-comparison protocol, the PSD-constrained route reduces route-to-observed error, bias, and upper-tail amplification relative to the fitted-reference route. That is the contribution of Section 5 at section level. It is not a universal constitutive exponent law. It is not an external predictive-validation claim. It is a more disciplined route for representing pre-failure resistance from a declared pre-shear material state. Section 4 established the measurable state. Section 5 shows that the same state can discipline pre-failure resistance. Section 5.5 now fixes the boundary and prepares the transition to Section 6, where the problem becomes post-failure consequence once that resistance is reduced or lost.

5.5. Section synthesis, claim boundary, and transition to Section 6

Section 5 closes the second analytical level of the dissertation, pre-failure resistance. Table 11 to Table 15 show that, across 42 published studies, 1005 admitted triaxial compression data points, and 181 pre-shear PSD-defined cases, the PSD-constrained route remains close to fitted-curvature practice while reproducing the observed peak-state response with lower error. Median signed curvature deviation is −0.03 and median absolute curvature deviation is 0.08. Median MAE decreases from 0.24 to 0.06 MPa, median RMSE from 0.26 to 0.07 MPa, and median Bias from 0.24 to 0.06 MPa under the adopted sign convention. The section claim is therefore direct: within the observed domain, within the admitted peak-state triaxial database, pre-shear PSD scaling provides a bounded curvature constraint for the adopted power-law calibration route. Measured pre-shear state no longer serves only as description or empirical screening input. In Section 5, it disciplines the structure of pre-failure resistance itself.

The engineering significance of that result lies in lower central response discrepancy and a reduced upper-error range, not in elimination of all high-error cases. Table 13 shows that the standard deviation of RMSE decreases from 1.74 to 0.86 MPa and the maximum RMSE from 15.35 to 8.00 MPa. The remaining 8.00 MPa maximum confirms that upper-tail residuals remain under the PSD-constrained route. Table 15 further shows that response penalties are rare across the absolute curvature-deviation classes, so the remaining departures are not controlled by curvature substitution alone It resolves the actual mechanics problem set by this section: how to constrain curvature without losing engineering fidelity in the observed database, while reducing the upper-stress amplification that free fitting can produce.

The claim boundary of Section 5 is exact. It does not establish a universal constitutive exponent law, full-range fractal control of shear strength, or external predictive validation. The formulation remains an anchor-normalized power-law envelope in which curvature is assigned from finite-window pre-shear PSD scaling and only the anchor strength level is fitted from peak-state triaxial evidence. Direct shear, residual-state response, cyclic loading, and post-shear PSD evolution remain outside scope. The inference is also bounded to the admitted stress range, PSD range, apparatus-size range, and peak-state triaxial conditions represented in the compiled database.

These are not weaknesses. They are the conditions that keep this section technically defensible and analytically transferable as a disciplined representation of pre-failure resistance.

This boundary defines the transition to Section 6. Section 4 resolved measurable material state. Section 5 resolved pre-failure resistance representation for that declared state. Section 6 will resolve post-failure consequence once that resistance is reduced or lost. The continuity is analytical and mechanical, not fully numerical: the dissertation does not propagate one calibrated envelope directly into a single runout simulator. It crosses the failure boundary in the correct thesis order, from measured state to pre-failure resistance, to post-failure consequence. That is not a break in the dissertation logic. It is the next step in the same field-to-consequence chain.

6. POST-FAILURE CONSEQUENCE: FLOW-SLIDE MOBILITY IN HIGH-END WASTE DUMPS

Sections 4 and 5 resolved measured material state and pre-failure resistance. Section 6 resolves the third analytical level of the dissertation: post-failure consequence. It begins where resistance is no longer sufficient to prevent motion and the governing engineering question becomes consequence: how far the failed mass travels, how rapidly it moves, and which field conditions control that behavior. In high-end waste dumps, post-failure consequence is governed by the coupled action of pore pressure, basal resistance, path geometry, and dynamic resistance rather than by source geometry alone. Section 6 therefore does not revisit pre-failure shear-strength representation. It defines the consequence field that must be explained once resistance is reduced or lost (Bishop 1959; Hungr 1995; Dawson et al. 1998; Hungr and McDougall 2009).

This section is built on a documented database of 46 high-end waste-dump failures from southeastern British Columbia. It first defines that failure record and refines it into four mobility classes, low, moderate, high, and extreme, before interpreting those classes through pore-pressure ratio, basal resistance, path confinement, basal-bed slope, and dynamic resistance. The evidence base comes first. The mechanics follow it (Golder Associates 1991, 1992; Golder Associates and Hungr 1995; Arrieta and Zhang 2025).

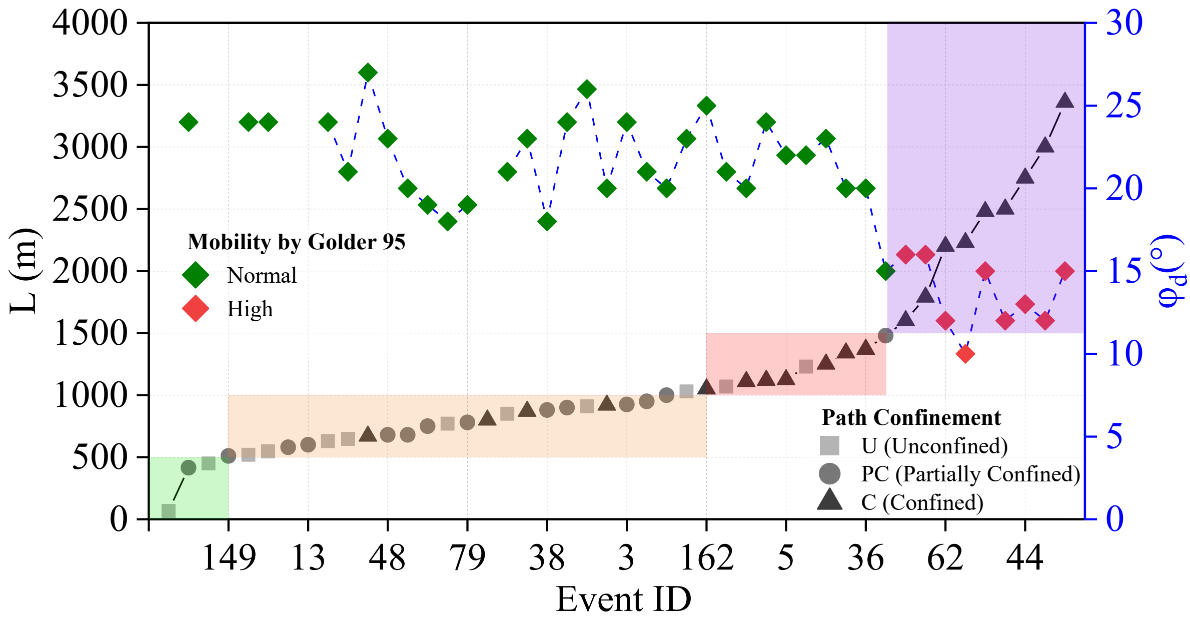

Figure 15. Runout distribution and four-tier mobility classes of the 46 documented failures used in Section 6.

The mechanics used later in this section are screening-level and explicit: back-analysis of equivalent basal resistance, effective-stress reduction through pore pressure, measurable path confinement, Voellmy-type dynamic resistance, and a Brachistochrone-based frictionless benchmark used only as a reference comparator. The benchmark is not treated as the real path of a failed mass and not as an inviolable upper-bound law for field motion (Golder Associates 1991, 1992; Golder Associates and Hungr 1995; Erlichson 1999; Arrieta and Zhang 2025).

The purpose of Section 6 is exact. It identifies the controls that transform a waste-dump failure into a long-runout flow slide and translates those controls into a screening-level mechanics framework for consequence assessment. It does not attempt a coupled hydro-mechanical site-specific runout simulation, and it does not claim direct numerical propagation from the calibrated resistance envelopes of Section 5 into a single predictive mobility model. Its contribution is to close the field-to-consequence chain by showing how resistance loss is expressed in mobility through pore pressure, basal resistance, path geometry, and dynamic resistance. For that reason, Section 6 must begin with the consequence evidence base itself: the failure database and the mobility classes that later sections must separate mechanically (McDougall 2017; Arrieta and Zhang 2025).

6.1. Failure database, four-tier mobility classes, and screening-level mechanics after resistance loss

Section 6 begins at the failure boundary. Once pre-failure resistance is reduced or lost, the governing question is no longer how strength is represented, but how consequence develops. Section 6.1 therefore has a double function that must remain explicit: it first fixes the observed field consequence, and it then defines the minimum mechanics required to interpret that field. The consequence field is the documented database of 46 high-end waste-dump failures from southeastern British Columbia. Figure 15 not a decorative figure. It is the first result of the section: the runout record does not collapse into one undifferentiated population, and the older two-tier mobility distinction is too coarse for thesis use. In this dissertation, the events are resolved into four consequence classes: low mobility for $L < 500\text{m}$, moderate mobility for $500 \leq L < 1000\text{m}$, high mobility for $1000 \leq L < 1500\text{m}$, and extreme mobility for $L \geq 1500\text{m}$. The rest of Section 6 has to explain that structured consequence field, not merely restate it (Hungr 1995; Hungr and McDougall 2009; McDougall 2017; Arrieta and Zhang 2025).

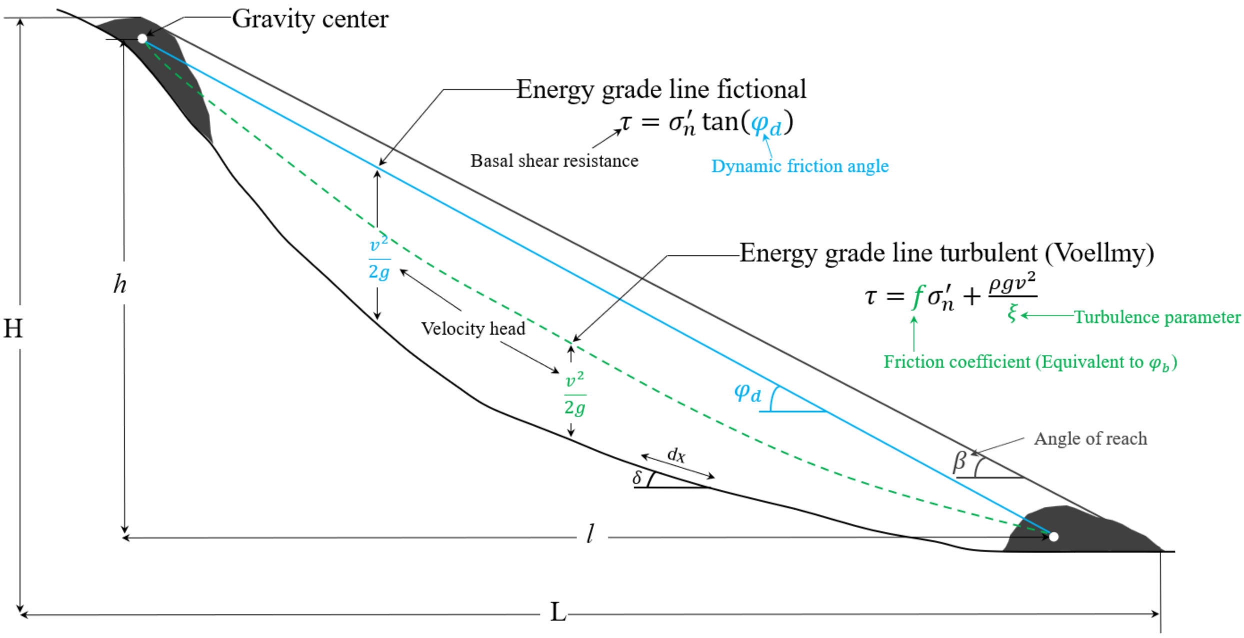

Figure 16. Energy-grade-line interpretation of the screening-level mobility mechanics adopted in Section 6.1.

With the consequence classes fixed, the mechanics can be introduced for a reason. Figure 16 summarizes the screening-level framework adopted in this section through the energy-grade-line interpretation: a frictional line defined by equivalent basal resistance, a pore-pressure-controlled reduction of effective stress, and a velocity-dependent line that represents additional dynamic dissipation. This is the right level of mechanics for the thesis. Anything simpler suppresses one of the dominant controls on runout. Anything more elaborate exceeds the screening-level claim boundary established for Section 6.

The first mechanical quantity needed is the equivalent dynamic friction angle φ_d, because the documented events already tell us the fall height H and runout distance L. The starting point is therefore the classical sliding-block representation, used here as a back-analysis tool for post-failure motion rather than as a constitutive law for the material itself. For a failed mass moving downslope, the along-path acceleration is written as:

$$m\frac{d^2x}{dt^2} = mg\sin(\delta) - mg\cos(\delta)\tan(\varphi_d) \tag{10}$$

where g is gravitational acceleration, δ is the basal-bed slope, and φ_d is the equivalent dynamic friction angle. When the moving mass reaches its distal limit and the centroid velocity falls to zero, the back-analysis reduces to:

$$\tan(\varphi_d) = \frac{H}{L} \tag{11}$$

Eq. 11. is the first mechanical reduction of the failure database. It converts observed consequence geometry into an equivalent basal-resistance indicator. That is why it belongs here: Section 6 is not estimating an abstract friction angle, it is interpreting how much resistance must have remained after failure initiation in the documented events (Scheidegger 1973; Hungr 1995; Arrieta and Zhang 2025).

Dry friction alone does not explain the longest runouts in Figure 15. The second mechanism required is the reduction of effective basal resistance through pore pressure. Following Bishop-type reasoning, the pore-pressure increment generated under rapid undrained loading is written as:

$$\Delta\mu = B\Delta\sigma_v \tag{12}$$

where u is pore pressure, B is Bishop's pore-pressure coefficient, and $\Delta\sigma_v$ is the vertical stress increment. With the pore-pressure ratio defined at the basal bed and with $\sigma_n = \sigma_v\cos\delta$, the effective-stress reduction enters the basal friction term as:

$$\tau = (\sigma_n - \mu)\tan(\varphi_d) = (1 - r_u)\sigma_n\tan(\varphi_d) \tag{13}$$

Eq. 13 is the decisive mechanics transition of Section 6.1. Once r_u increases, effective normal stress falls, the frictional part of basal resistance collapses, and the consequence field changes class. In the documented high-end dumps, this is not secondary detail. It is the main route by which weak, saturated, or liquefaction-prone basal materials generate high and extreme mobility (Bishop 1973; Dawson et al. 1998; Arrieta and Zhang 2025).

A third mechanism is still missing. Once flow slides become rapid, a frictional term alone is no longer enough; momentum exchange and collisional or turbulent dissipation also control mobility. For that reason, the section adopts the Voellmy-type representation:

$$\tau = (1 - r_u)\sigma_n \tan(\varphi_d) + \frac{\rho g v^2}{\xi} \tag{14}$$

where ρ is bulk density, v is flow velocity, and ξ is the turbulence coefficient. Eq. 14 completes the mechanics structure of this section. The first term expresses frictional resistance after pore-pressure reduction of effective stress. The second expresses the velocity-dependent dissipation that becomes more important once motion is rapid and laterally focused. This is exactly why Figure 16 matters: it makes explicit that high mobility in Section 6 cannot be read from basal friction alone (Voellmy 1955; Hungr 1995; Hungr and McDougall 2009; Arrieta and Zhang 2025).

For the event-based interpretation used later in this section, Eq. 14 is rearranged to recover the turbulence coefficient from observed or post-dicted field quantities:

$$\xi = \left(\frac{L}{\tau L - H\sigma_n}\right)\rho g v^2 \tag{15}$$

Eq. 15 is operational, not universal. Its function is to make velocity-dependent dissipation comparable across the 46 documented failures within one screening-level framework. That is enough for the thesis. Section 6 does not need a universal turbulence law; it needs a defensible way to compare how reduced basal resistance and runout-corridor conditions combine to produce low, moderate, high, and extreme mobility (Arrieta and Zhang 2025).

The logic of Section 6.1 is now explicit. Figure 15 defines the consequence field that has to be explained. Figure 16 and Eq. 10 to Eq. 15 define the minimum mechanics needed to explain it: equivalent dynamic friction from observed geometry, pore-pressure reduction of effective stress, and velocity-dependent resistance. What remains unresolved after Section 6.1 is not the general mechanics of motion, but the geometry of the runout corridor itself. Section 6.2 must therefore define confinement in measurable form through the coefficient a.

6.2. RUNOUT PATH GEOMETRY AND THE CONFINEMENT COEFFICIENT a

Section 6.1 fixed the post-failure mechanics required after resistance loss through equivalent basal resistance, pore-pressure reduction of effective stress, and velocity-dependent dissipation. One control remains undefined: the geometry of the runout path itself. The documented failures include confined, partially confined, and unconfined paths, but those labels cannot yet enter the. Section 6 mechanics in measurable form. Section 6.2 therefore does one exact job: it converts path shape into a confinement variable that can be carried directly into the consequence analysis (Nicoletti and Sorriso-Valvo 1991; Golder Associates and Hungr 1995; Arrieta and Zhang 2025).

The path classes are mechanically distinct. Confined paths remain narrower than the source over a substantial part of the travel path and therefore focus the moving mass. Partially confined paths allow limited lateral spreading. Unconfined paths widen progressively and dissipate momentum through lateral dispersion. The engineering consequence is direct: path geometry controls whether flow depth is preserved, whether velocity persists, and whether the dynamic term of Eq. 14 remains important over distance. Confinement is therefore treated here as a primary path control on mobility, not as secondary site description (Borenäs and Lundberg 1986; Nicoletti and Sorriso-Valvo 1991; Arrieta and Zhang 2025).

To quantify that control consistently across the 46-event database, the representative cross-section of the runout path is expressed as a parabola referenced to the thalweg, taken as the lowest point of the cross section. The adopted expression is:

$$y = ax^2 \tag{16}$$

where x is the horizontal distance from the thalweg, y is the elevation above the thalweg, and a is the fitted geometric coefficient. Rearrangement gives:

$$a = \frac{y}{x^2} \tag{17}$$

For a fixed elevation y, the corresponding half-width is:

$$x = \sqrt{\frac{y}{a}} \tag{18}$$

Eq. 16 to Eq. 18 fix the meaning of a unambiguously. For a fixed y, larger $a$gives smaller x, and therefore a narrower path. In this dissertation, larger $a$means stronger confinement. That definition is non-negotiable, because the later mobility analysis depends directly on the sign of the a-mobility relation. Figure 17 is the standard geometric construction used throughout Section 6: thalweg as the reference point, $x$as half-width, $y$as elevation above the thalweg, and a as the fitted confinement coefficient (Arrieta and Zhang 2025).

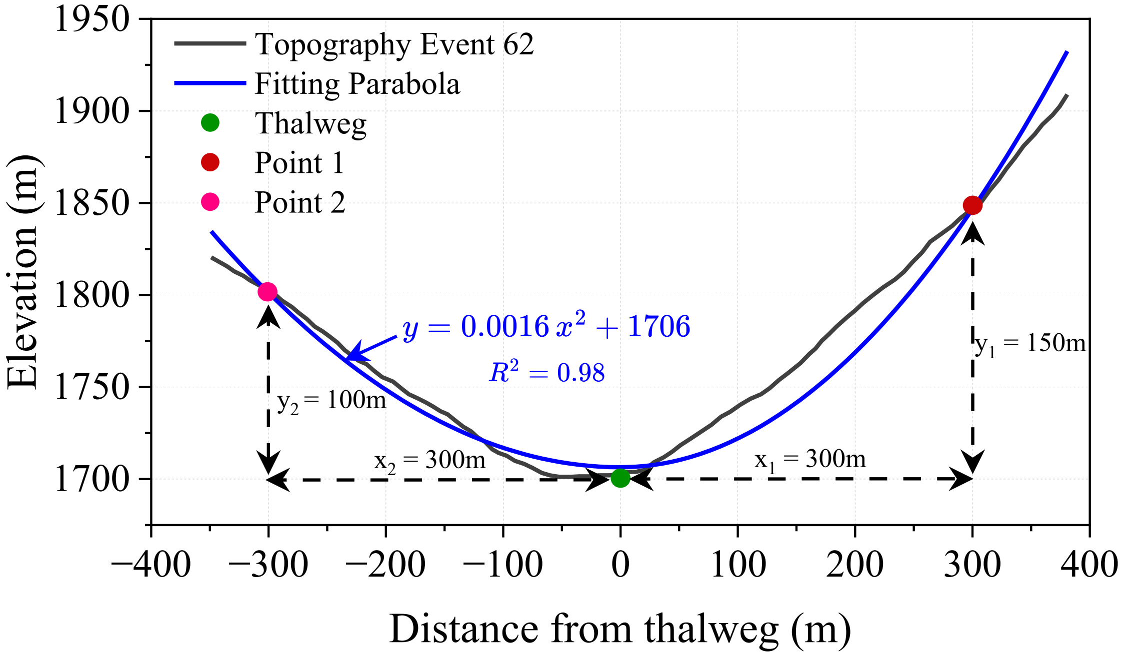

Figure 17. Estimation of the confinement coefficient a from a fitted parabolic cross-section.

This definition explains exactly how path geometry enters the mechanics fixed in Section 6.1. Larger $a$means a narrower path, less lateral spreading, stronger focusing of the moving mass, and more persistent flow depth. Under those conditions, velocity is sustained over longer distances and the dynamic-resistance term in Eq. 14, together with the event-based back-analysis of ξ in Eq. 15, becomes more consequential because momentum is concentrated rather than dispersed laterally. By contrast, smaller a denotes broader path sections, earlier spreading, and weaker persistence of high-velocity motion. Within the documented failure database, a is therefore not a descriptive add-on. It is the measurable path variable that links qualitative path classes to the mechanics of post-failure consequence. It is the geometric control required to move from path description to path-based mobility discrimination (Borenäs and Lundberg 1986; Arrieta and Zhang 2025).

The logic of Section 6 is now continuous. Section 6.1 defined the post-failure mechanics after resistance loss. Section 6.2 adds the missing geometric control by defining path confinement in measurable form through a. Section 6.3 can therefore move directly to the decisive test: which combinations of r_u, f, a, and δ actually separate low, moderate, high, and extreme mobility in the documented failure database.

6.3. Coupled controls and thresholds that separate the four mobility classes

Sections 6.1 and 6.2 fixed the consequence field and the mechanics needed to interpret it: the 46-event database, the four mobility classes, the post-failure variables r_u, f, and δ, and the path-confinement coefficient a. Section 6.3 now does the first true results work for Section 6. It tests which combinations of those variables actually separate low, moderate, high, and extreme mobility once resistance has been reduced or lost. The failure record does not scatter randomly in consequence space. High and extreme mobility cluster where pore-pressure ratio is elevated, basal friction is very low, path confinement is strong, and basal-bed slope lies within a limited mobility window. Low and moderate mobility occupy the opposite side of that field. The purpose of this section is to show that pattern explicitly from the documented events and then state it mechanically in the language already fixed by Sections 6.1 and 6.2 (Arrieta and Zhang 2025).

The first control is path confinement. Under the fixed parabolic definition of Section 6.2, larger a means a narrower path and therefore stronger confinement. Figure 18 shows that runout distance tends to increase with increasing a, and Figure 19 shows that maximum velocity rises in the same direction.

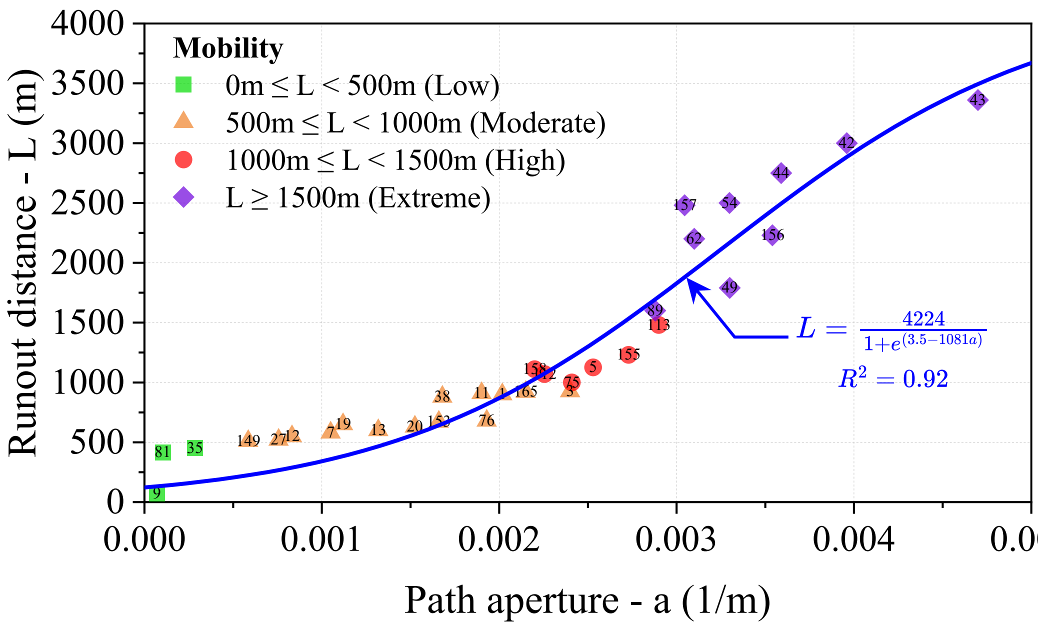

Figure 18. Runout distance as a function of the confinement coefficient a.

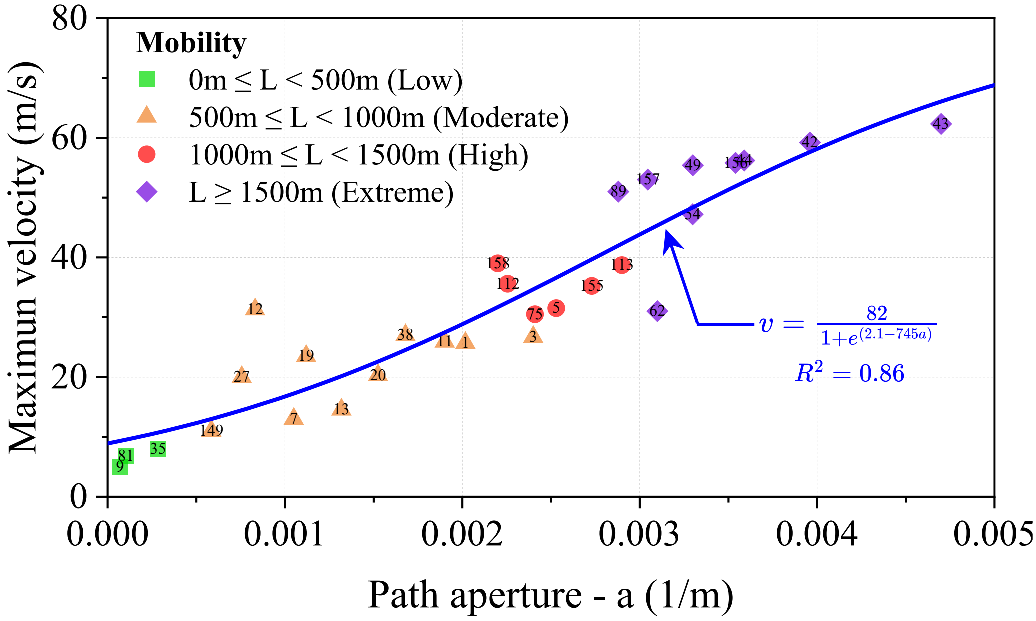

Figure 19. Maximum velocity as a function of the confinement coefficient a.

Taken together, the two figures establish one result: confinement does not merely guide the failed mass laterally. It preserves flow depth, focuses momentum, and helps sustain motion over longer distances. In the mechanics of Section 6, a is therefore the geometric amplifier of mobility, not its primary driver. That reading is consistent with the geomorphic interpretation in which channelized paths preserve directed motion more efficiently than laterally spreading flows (Nicoletti and Sorriso-Valvo 1991; Arrieta and Zhang 2025).

The second control is basal shear resistance, expressed here through the friction coefficient f. Figure 20 shows that runout distance decreases sharply as f increases. The class separation is direct: extreme-mobility failures concentrate where f is very low, generally below about 0.15, equivalent to a dynamic friction angle below roughly 10°.

Low-mobility events occupy the higher-friction end of the field. This is mechanically decisive. High-end waste-dump flow slides require severe basal weakening after failure initiation, consistent with dumps founded on weak, saturated, or liquefaction-prone basal materials. Figure 20 therefore remains essential to the interpretation, but f is not included in Table 16 as an independent lead indicator. In this framework, f is back derived from the same post-failure geometry through Eq. 11, so a rank test against L would be circular. The statistical summary therefore uses r_u, a, and δ as the independent lead indicators and treats r_u as the physical driver of the low-friction state (Dawson 1994; Dawson et al. 1998; Arrieta and Zhang 2025).

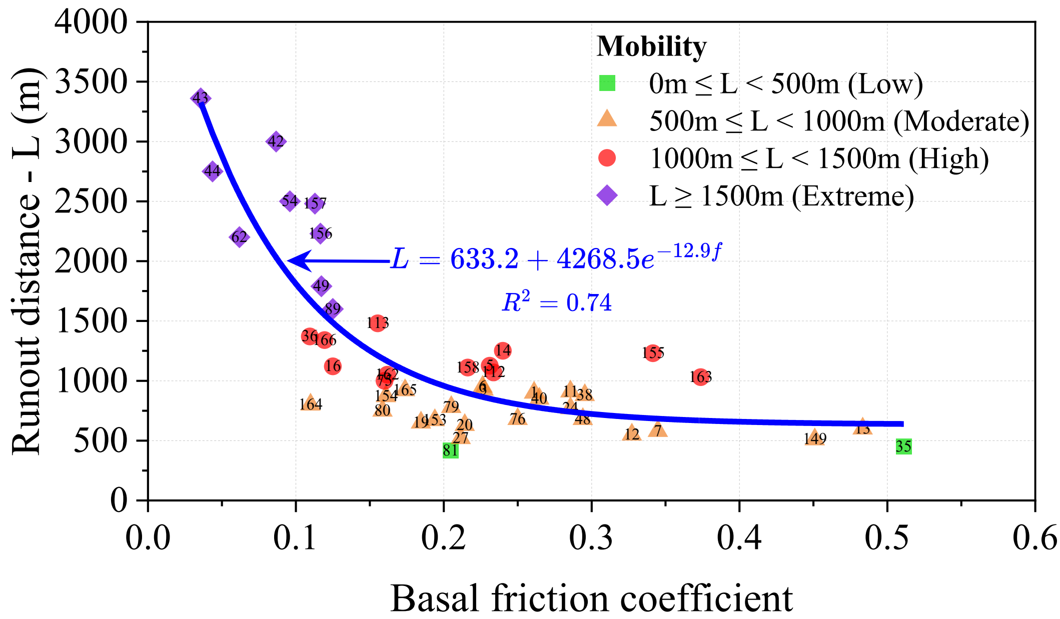

Figure 20. Runout distance as a function of basal friction coefficient f.

The third control is pore pressure at the basal bed. Figure 21 shows that the runout field changes character once the pore-pressure ratio rises above about $r_u = 0.4$. Below $r_u < 0.3$, long runouts are uncommon. Between 0.3 and 0.4, the outcome field is mixed. Above 0.4, the greatest travel distances concentrate in the high- and extreme-mobility classes. This is the clearest driver in the database. Through Eq. 13, elevated r_u reduces effective normal stress, lowers the frictional part of basal resistance, and moves the failed mass into the high-mobility domain. The small number of long-runout cases at lower r_u do not weaken that conclusion. They show that strong confinement and favorable path slope can amplify motion when the path is exceptionally efficient. The primary reading remains unchanged: r_u is the principal driver of mobility in the documented failure set (Bishop 1973; Dawson 1994; Dawson et al. 1998; Arrieta and Zhang 2025).

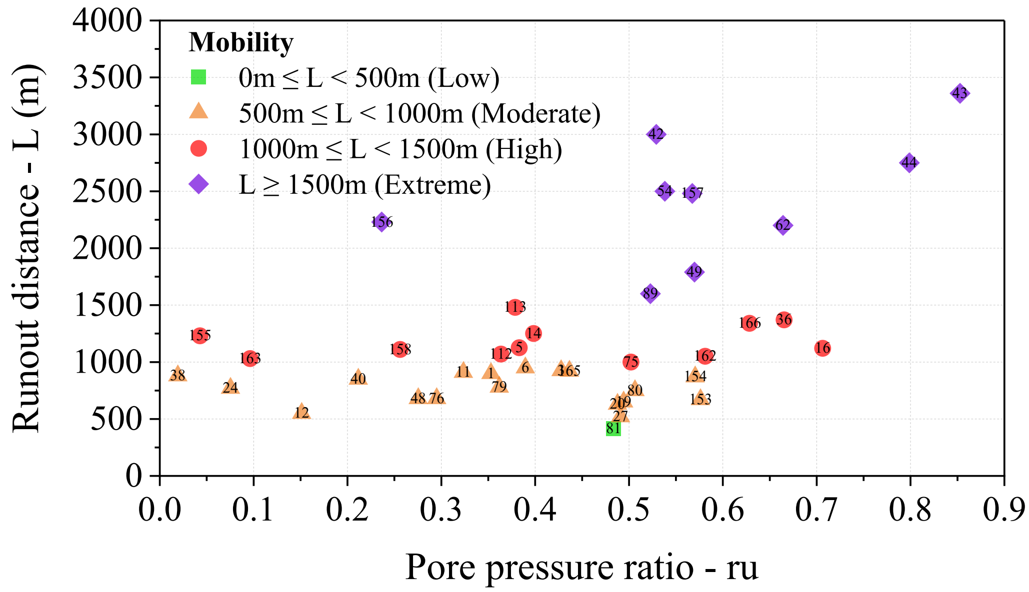

Figure 21. Runout distance as a function of pore-pressure ratio r_u.

The fourth control is the basal-bed slope δ. Figure 22 shows that the longest runouts are concentrated mainly where δ lies between approximately 15° and 30°. This is the mobility window of the database. Slopes steeper than 30° do not dominate the extreme-runout field, and very gentle slopes do not dominate it either. The interpretation is precise. δ is not a simple accelerator of motion. It is a limiter of total reach. Within the intermediate range, the path retains enough driving force while still permitting the undrained and liquefaction-prone conditions associated with long travel. Outside that range, either horizontal room for travel is reduced or deposition becomes more likely (Benda and Cundy 1990; Bathurst et al. 1997; Arrieta and Zhang 2025).

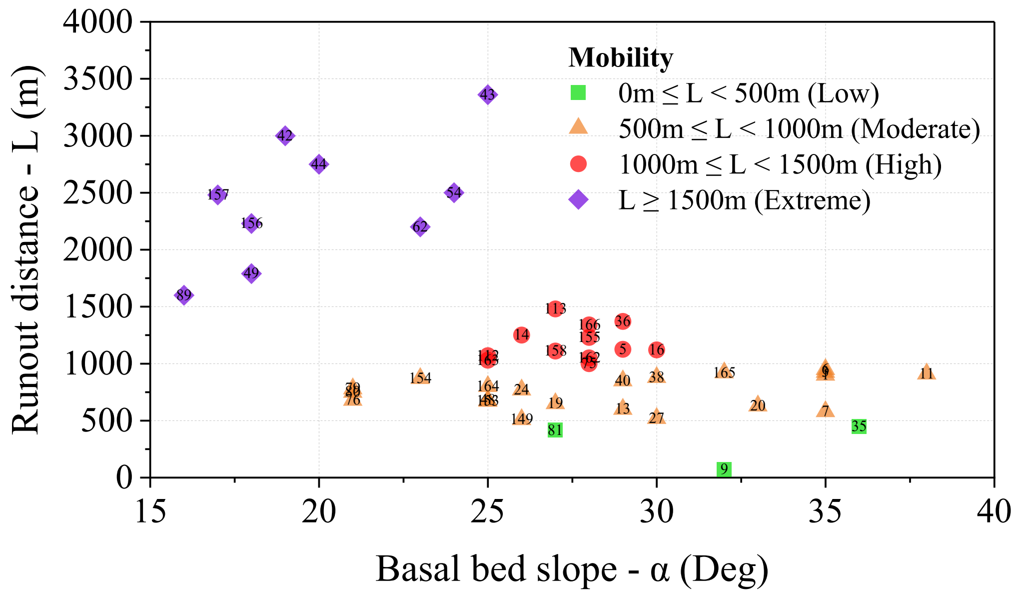

Figure 22. Influence of basal-bed slope δ on runout distance.

The key point is that these controls do not act independently. High and extreme mobility occurs where basal friction is very low, pore pressure is elevated, confinement is strong, and basal-bed slope lies inside the mobility window. The opposite combination confines failures to low or moderate runout. That coupled mechanics field is the real result of Section 6.3. The mobility classes are not descriptive labels attached after the fact. They are the consequence response of the failed mass to a definable combination of f, r_u, a, and δ (Arrieta and Zhang 2025).

Table 16 confirms the same pattern quantitatively. Runout $L$is positively associated with $r_u(\psi = +0.40,\ p = 0.01)$, positively associated at trend level with $a(\psi = +0.37,\ p = 0.08)$, and negatively associated with $\delta(\psi = -0.42,\ p < 0.01)$.

Table 16. Rank-based associations between runout and the lead indicators r_u, a, and δ.

Rank	Correlation	L	r_u	a	δ
L	ψ	1.00	0.40	0.37	-0.42
	p-value	--	0.01	0.08	0.00
r_u	ψ	0.40	1.00	0.20	-0.26
	p-value	0.01	--	0.40	0.11
a	ψ	0.37	0.20	1.00	-0.56
	p-value	0.08	0.40	--	0.00
δ	ψ	-0.42	-0.26	-0.56	1.00
	p-value	0.00	0.11	0.00	--

The same table also shows a negative association between $a$and $\delta(\psi = -0.56,\ p < 0.01)$, which is physically consistent with the most mobile events in this dataset: strongly confined paths tend to coincide with gentler along-path slopes that provide more horizontal room for travel. The quantitative reading therefore matches the figure-based reading. Pore pressure acts as the driver, confinement acts as the amplifier, and basal-bed slope acts as the limiter (Arrieta and Zhang 2025).

Section 6.3 therefore establishes the control structure of post-failure consequence. Once resistance is reduced or lost, mobility in high-end waste dumps is separated by a coupled control space defined by r_u, f, a, and δ. Section 6.4 does not replace that interpretation. It tests how close the most mobile failures come to a frictionless reference comparator and, in doing so, fixes the final scope boundary of the consequence framework.

6.4. Frictionless reference benchmark and the scope boundary of consequence assessment

Section 6.3 already established the coupled control space that separates low, moderate, high, and extreme mobility. Section 6.4 does not introduce a new explanation. It asks one narrower question: how close do the documented failures come to a frictionless reference state once that control space has already been identified? The Brachistochrone is used here only as a reference comparator for ideal no-dissipation descent. It is not treated as the real path of the failed mass, and it is not used to claim that a waste-dump flow slide literally follows a cycloid in the field (Erlichson 1999; Arrieta and Zhang 2025).

For the benchmark used in this section, the ideal frictionless quantities are written as:

$$v_{opt} = \sqrt{2gH} \tag{19}$$

and

$$t_{opt} \approx \pi\sqrt{\frac{H}{g}} \tag{20}$$

where H is the maximum vertical fall height and g is gravitational acceleration. Observed failures are then compared to these reference values through the ratios:

$$\eta_v = \frac{v_{obs}}{v_{opt}} \tag{21}$$

and

$$\eta_t = \frac{t_{obs}}{t_{opt}} \tag{22}$$

These ratios do not define a new mechanics law. They quantify proximity to the frictionless reference state after the mobility controls have already been identified. In the logic of Section 6, they are the last step in consequence interpretation, not a replacement for the control framework established in Section 6.3 (Erlichson 1999; Arrieta and Zhang 2025).

Figure 23 gives the direct mechanical reading. Most events remain below the frictionless reference line, confirming that frictional and dynamic processes dissipate part of the available gravitational energy. At the same time, many high- and extreme-mobility failures approach a large fraction of that reference. In the database analyzed here, extreme events commonly reach about 60-90% of the frictionless reference velocity, whereas low- and moderate-mobility cases remain distinctly lower. The most mobile failures are therefore not only farther-traveling; they are dynamically closer to the no-dissipation reference state (Arrieta and Zhang 2025).

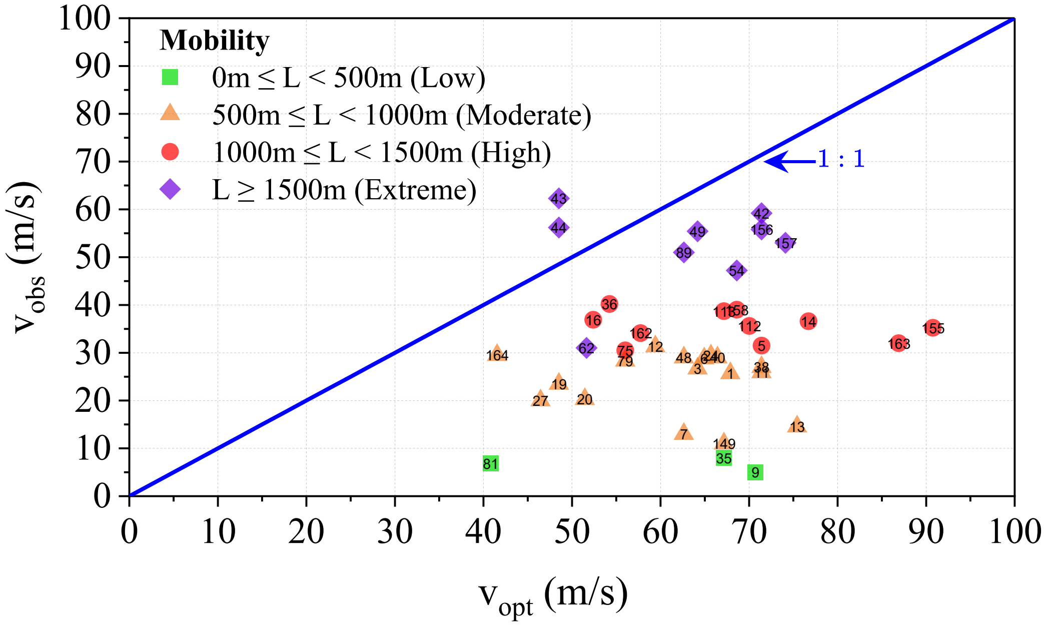

Figure 23. Observed flow-slide velocity relative to the frictionless reference benchmark.

Figure 24 provides the ratio view and also fixes the caution required by the benchmark. The velocity ratio η_v is the more robust indicator of proximity to the frictionless reference. The time ratio η_t is much more sensitive to path segmentation, timing resolution, and the adopted vertical drop. For that reason, the benchmark in this dissertation is used strictly as a reference comparator, not as an inviolable physical upper-bound law for every reported field point. Apparent exceedances or unusually short travel times are therefore interpreted as uncertainty-sensitive proximity to the frictionless envelope rather than as proof of super-physical motion. That caution does not weaken the benchmark. It keeps it in its correct role: a mechanical reference for judging how close the most mobile failures come to zero-dissipation motion (Erlichson 1999; Arrieta and Zhang 2025).

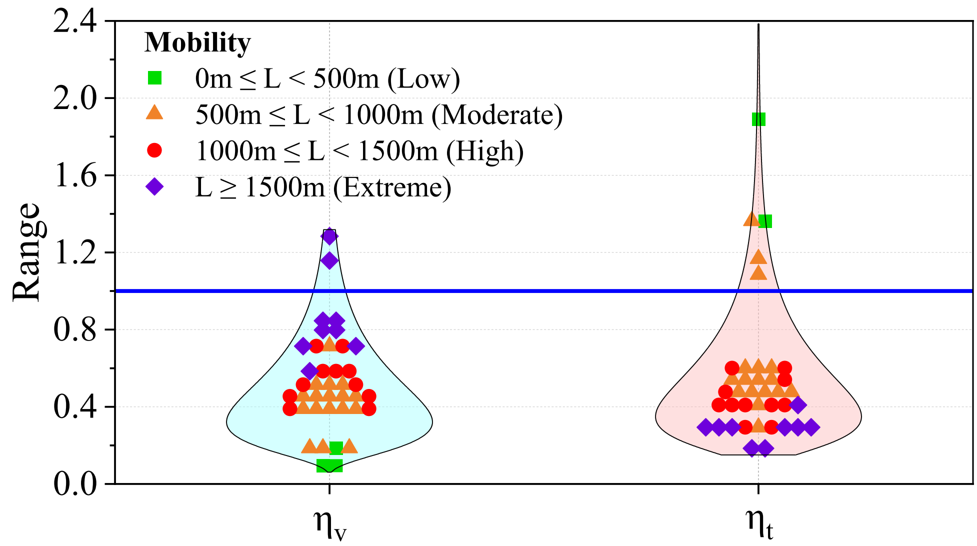

Figure 24. Velocity and time ratios relative to the frictionless reference benchmark.

The benchmark therefore confirms, rather than replaces, the interpretation established in Section 6.3. The failures that approach the frictionless reference most closely are the same failures already identified as occurring under elevated pore pressure, very low basal friction, strong path confinement, and basal-bed slopes within the mobility window. The Brachistochrone comparison does not create a new explanation. It confirms how severe that control combination becomes when it drives the failed mass toward a near-frictionless response state (Arrieta and Zhang 2025).

The scope boundary of this section is therefore explicit, it provides a screening-level mechanics framework for post-failure consequence based on a documented event database, effective-stress reduction through pore pressure, dynamic resistance, path confinement, and a frictionless reference comparator. It does not provide a coupled hydro-mechanical site-specific runout model, and it does not propagate the calibrated stress-dependent envelopes of Section 5 into a single end-to-end simulator. That is not a deficiency. It is the exact claim boundary that keeps the consequence framework defensible (Arrieta and Zhang 2025).

This boundary also defines the transition to Section 7. Section 4 established measurable field state. Section 5 established how that state constrains pre-failure resistance. Section 6 established how post-failure consequence is governed once resistance is reduced or lost. Section 7 can now do the thesis-level work that no appended paper can do independently: integrate state, resistance, and consequence into one field-to-consequence geotechnical framework for coarse mine waste dumps (Arrieta and Zhang 2024, 2025, 2026).

6.5. Section synthesis, scope boundary, and transition to Section 7

Section 6 closes the third analytical level of the dissertation: post-failure consequence. Across the 46 documented failures, the four-tier mobility classification, the mechanics of resistance loss, the path-confinement coefficient a, and the frictionless reference comparator establish one direct result: post-failure consequence is not an arbitrary extension of failure and is not controlled by source geometry alone. It is governed by a coupled mobility field in which elevated pore-pressure ratio, severe basal weakening, strong path confinement, and basal-bed slopes within the mobility window produce the longest and fastest runouts.

The result is not a loose collection of indicators. The high- and extreme-mobility events occupy the same consequence domain: r_u commonly above about 0.4, f commonly below about 0.15, larger a values indicating stronger path confinement, and δ concentrated within the mobility window identified in Section 6.3. Section 6.4 then shows that these same events approach the frictionless reference most closely, commonly reaching about 60-90% of the reference velocity. The Brachistochrone comparison therefore confirms the severity of the same control combination already identified from the failure database; it does not introduce a second explanation. This is the section result: once resistance is reduced or lost, mobility in high-end waste dumps is governed by identifiable controls that separate low, moderate, high, and extreme consequence classes (Arrieta and Zhang 2025).

The engineering reading is precise. Pore pressure acts as the driver because it reduces effective normal stress and pushes the basal bed into a low-friction state. Basal friction remains mechanically essential as the expression of that weakening, even though the rank summary in Table 16 is carried by the independent lead indicators r_u, a, and δ. Path confinement acts as an amplifier because larger a values denote narrower paths that preserve flow depth, concentrate momentum, and sustain velocity. Basal-bed slope acts as the limiter because extreme travel is concentrated within a defined geometric window rather than increasing monotonically with slope. In that sense, Section 6 closes the post-failure part of the thesis by converting a broad mobility problem into a bounded and defensible consequence framework (Bishop 1973; Dawson 1994; Dawson et al. 1998; Arrieta and Zhang 2025)

The claim boundary of Section 6 is exact, it provides a screening-level mechanics framework for post-failure consequence. It does not provide a site-specific coupled hydro-mechanical runout simulation, and it does not propagate the calibrated resistance envelopes of Section 5 into a single end-to-end mobility model. The Brachistochrone is used strictly as a frictionless reference comparator for proximity to a no-dissipation state. It is not treated as the real path of the failed mass, and apparent exceedances are interpreted cautiously as uncertainty-sensitive benchmark comparisons rather than as proof of super-physical motion. Keeping that boundary explicit is what makes the consequence framework technically defensible (Erlichson 1999; Arrieta and Zhang 2025).

This boundary makes Section 7 necessary. Section 4 established measurable field state through dump-scale PSD characterization. Section 5 established how that pre-shear state constrains pre-failure resistance through PSD-constrained curvature. Section 6 has now established how post-failure consequence is governed once that resistance is reduced or lost. What remains is not another result, but thesis-level integration. Section 7 can therefore do the work that no appended paper can do independently: integrate state, resistance, and consequence into one field-to-consequence geotechnical framework for coarse mine waste dumps (Arrieta and Zhang 2024, 2025, 2026).

7. INTEGRATED FIELD-TO-CONSEQUENCE FRAMEWORK FOR COARSE MINE WASTE DUMPS

Section 7 performs the thesis-level synthesis of the dissertation. It is kept as a separate section because it integrates the outputs of Sections 4, 5, and 6 rather than presenting another component study. Sections 4 to 6 have already established the three analytical levels of the thesis: measurable material state, pre-failure resistance, and post-failure consequence. The task here is to integrate those results into one field-to-consequence argument for coarse mine waste dumps. The section develops that synthesis through two analytical handoffs. The first carries measurable field state into pre-failure resistance representation. The second carries resistance loss into post-failure consequence assessment. On that basis Section 7 converts the chain into an integrated engineering workflow and closes by stating the exact thesis contribution (Arrieta and Zhang 2024, 2025, 2026).

7.1. THESIS ARGUMENT AND ANALYTICAL CONTINUITY ACROSS THE STATE-RESISTANCE-CONSEQUENCE CHAIN

The thesis argument is a bounded continuity claim. The dissertation stands as one controlled argument only if coarse mine waste hazard can be carried across two defined analytical transitions without breaking its engineering logic: from measurable material state to pre-failure resistance representation, and from resistance loss to post-failure consequence assessment. That continuity is analytical and mechanical. It is not the transfer of one unchanged scalar through all Sections, and it is not a direct numerical simulator from field PSD to runout (Arrieta and Zhang 2024, 2025, 2026).

The first analytical transition is from state to resistance. Section 4 established PSD as a defensible field-scale descriptor of material state. Section 5 established that pre-shear PSD scaling provides a bounded curvature constraint within the adopted stress-dependent power-law calibration route. The continuity claimed by the thesis is therefore PSD as state at both levels, not one site-specific D_{50} inserted directly into the compiled triaxial database. In Section 4, PSD appears as field-measurable gradation. In Section 5, it appears as a finite-window pre-shear PSD-scaling descriptor used as a bounded curvature constraint (Arrieta and Zhang 2024, 2025, 2026).

The second analytical transition is from resistance to consequence. Section 5 defined the structure of available pre-failure resistance for a declared material state. Section 6 then interpreted consequence once that resistance was reduced or lost through pore pressure, basal resistance, path geometry, and dynamic resistance. The continuity claimed here is the failure boundary itself. No direct insertion of the Section 5 calibrated envelope into a single runout simulator is demonstrated. Post-failure mobility is interpreted as the mechanical consequence of resistance loss rather than as a separate hazard domain detached from pre-failure analysis (Arrieta and Zhang 2025, 2026).

In its shortest defensible form, the thesis argument is this: measurable field state can be carried into pre-failure resistance representation, and resistance loss can be carried into post-failure consequence assessment. Section 7.2 now develops the first analytical transition directly by showing how the field state established in Section 4 becomes the basis of the resistance framework developed in Section 5 (Arrieta and Zhang 2024, 2025, 2026).

7.2. MEASURED PSD AS THE LINK BETWEEN MATERIAL STATE AND PRE-FAILURE RESISTANCE

This link has to be stated precisely. The dissertation does not claim that one site-specific D_{50} from Section 4 is inserted directly into the compiled triaxial database of Section 5 That would be false. The defensible continuity is that PSD functions as state at both levels: in Section 4 as field-measurable gradation, and in Section 5 as a pre-shear PSD-scaling descriptor used as a bounded curvature constraint. The common variable is therefore PSD as state, not one shared scalar parameter forced across incompatible evidence bases (Arrieta and Zhang 2024, 2025, 2026).

Section 4 established the first half of that continuity by making PSD measurable at field scale. UAV-SfM characterization reproduced field particle size with screening-level accuracy, preserved both between-dump contrast and within-dump variability, and translated measured PSD into first-order resistance screening. That result matters here for one reason only: it established that pre-failure state can be expressed quantitatively at operational dump scale rather than left as visual description or laboratory abstraction (Barton and Kjaernsli 1981; Arrieta and Zhang 2024).

Section 5 established the second half by carrying PSD into the mechanics of pre-failure resistance. It did not treat PSD as background description or as an empirical plotting variable. It evaluated pre-shear PSD scaling as a bounded curvature constraint within an existing stress-dependent envelope family, leaving only the strength level to be fitted from peak-state triaxial evidence. The section result is the load-bearing point for Section 7: within the observed domain, within the admitted peak-state triaxial database, pre-shear PSD scaling provides a bounded curvature constraint for the adopted power-law calibration route (Arrieta and Zhang 2024, 2025, 2026).

The result of this section is therefore exact and bounded. In this dissertation, PSD is elevated from measurable gradation to resistance-relevant state descriptor. The continuity from Section 4 to Section 5 is real because it is carried by a shared state concept and a defined mechanical role, not by narrative stitching. That closes the first half of the field-to-consequence chain. Section 7.3 then develops the second half by showing how the dissertation moves from pre-failure resistance to post-failure consequence across the failure boundary (Arrieta and Zhang 2024, 2025, 2026).

7.3. Resistance loss as the analytical link between pre-failure resistance and post-failure consequence

The defensible continuity between Section 5 and Section 6 is the failure boundary itself. The dissertation does not claim that the calibrated resistance envelope of Section 5 is propagated directly into a single runout simulator in Section 6. No such numerical continuity is demonstrated. Section 5 defines the structure of available pre-failure resistance for a declared material state, and Section 6 defines the mechanics of consequence once that resistance is reduced or lost. That is the exact analytical continuity the thesis can defend (Arrieta and Zhang 2024, 2025, 2026).

In Section 5, pre-shear PSD scaling provides a bounded curvature constraint in the adopted stress-dependent power-law calibration route. That result matters beyond envelope fitting because it shows how declared material state can inform the represented pre-failure resistance field. Once weak basal conditions, elevated pore pressure, or progressive loading reduce that available resistance, the governing problem changes from peak-state resistance to post-failure motion.

Section 5 therefore does not end as an isolated calibration Section. It defines the resisting system whose degradation gives Section 6 physical meaning (Arrieta and Zhang 2025, 2026).

The result of this second analytical transition is therefore exact. In this dissertation, post-failure mobility is interpreted as the mechanical consequence of resistance loss. That is sufficient to connect Sections 5 and 6 without making a false end-to-end simulator claim. The next section converts that continuity, together with the state-to-resistance continuity developed in Section 7.2, into the integrated engineering workflow of the thesis (Arrieta and Zhang 2024, 2025, 2026).

7.4. INTEGRATED ENGINEERING WORKFLOW

Section 7.4 converts the analytical continuity established in Sections 7.2 and 7.3 into operational sequence. The framework begins with field-scale PSD characterization of exposed dump surfaces in order to define measurable material state at operational scale. Where the engineering question remains pre-failure, analysis proceeds to resistance representation, in which pre-shear PSD scaling provides the bounded curvature constraint and peak-state triaxial evidence calibrates the anchor strength level. Where the engineering question extends beyond instability, the framework then crosses the failure boundary and interprets consequence through pore-pressure ratio r_u, basal resistance f, path confinement a, basal-bed slope δ, and a frictionless reference comparator (Arrieta and Zhang 2024, 2025, 2026).

The sequence is strict because each analytical level depends on the previous one. Material state defines the basis for resistance representation. Resistance loss defines the basis for consequence assessment. The framework therefore carries geotechnical meaning from field measurement to screening-level consequence without implying one end-to-end numerical simulator (Arrieta and Zhang 2024, 2025, 2026).

Table 17. Integrated engineering workflow of the field-to-consequence framework.

Workflow stage	Main input	Main output	Valid engineering use	Principal uncertainty
Field-scale state characterization	Exposed dump surface and UAV imagery	PSD, D_{50}, spatial variability	Definition of measurable material state	Surface-only characterization; segmentation and visibility
Pre-failure resistance representation	Pre-shear PSD and admitted triaxial evidence	PSD-constrained stress-dependent power-law envelope	Representation of pre-failure resistance	Finite-window (D); admitted stress, PSD, and apparatus-size ranges; peak-state triaxial scope
Failure-boundary interpretation	Weak basal conditions and resistance loss indicators	Conditions for transition from stability to motion	Framing of credible failure scenarios	Basal material uncertainty; pore-pressure estimation
Post-failure consequence assessment	r_u, f, a, δ, frictionless benchmark	Mobility class and consequence screening	Screening-level runout and consequence assessment	Historical back-analysis; benchmark sensitivity

7.5. THESIS CONTRIBUTION AND EXACT CLAIM BOUNDARY

The thesis contribution is the integration of three bounded analytical levels into one field-to-consequence geotechnical framework for coarse mine waste dumps. Within that framework, measured PSD defines material state, pre-shear PSD scaling provides a bounded curvature constraint within pre-failure resistance representation, and resistance loss frames post-failure consequence through mobility mechanics. That is the exact thesis claim, and it is fully supported by the evidence assembled across Sections 4 to 6 (Arrieta and Zhang 2024, 2025, 2026).

The claim boundary is equally exact. The dissertation does not provide a universal constitutive law for coarse mine waste, does not provide a single end-to-end numerical simulator from UAV-derived PSD to runout prediction, and does not claim that PSD alone explains shear strength or mobility. Section 4 remains field-scale characterization and first-order screening of exposed dump surfaces. Section 5 remains a bounded PSD-constrained power-law calibration route, limited to pre-shear PSDs, peak-state triaxial compression, and the admitted stress, PSD, and apparatus-size ranges; it is not an external predictive or scale-independent validation claim. Section 6 remains a screening-level mechanics framework for post-failure consequence, not a site-specific coupled hydro-mechanical runout model (Arrieta and Zhang 2024, 2025, 2026).

With the synthesis claim fixed in this form, Section 8 can now do a different job: define the operational domain of the framework, identify the unresolved variables that still prevent direct predictive design use, and prioritize the research needed to strengthen predictive capacity.

8. OPERATIONAL SCOPE, METHODOLOGICAL LIMITS, AND RESEARCH NEEDS OF THE INTEGRATED FRAMEWORK

Section 8 defines the operational domain of the integrated framework, identifies the unresolved variables that still limit continuity across the state-resistance-consequence chain, explains why those limits prevent direct predictive design use, and prioritizes the research needed to strengthen predictive capacity. Its function is therefore operational rather than synthetic: the framework has already been established, and the task here is to state where it can be used with technical confidence and where it still remains incomplete. (Arrieta and Zhang 2024, 2025, 2026).

8.1. OPERATIONAL DOMAIN AND VALID ENGINEERING USE OF THE INTEGRATED FRAMEWORK

The integrated framework is operationally valid where coarse mine waste hazard has to be resolved across the three linked levels already established in the dissertation: measurable material state, pre-failure resistance, and post-failure consequence. At the state level, validity requires exposed dump surfaces that can be characterized by UAV photogrammetry and Structure-from-Motion reconstruction so that PSD and characteristic sizes such as D_{50} can be estimated at field scale. At the resistance level, validity requires a pre-failure problem centered on pre-shear gradation and peak-state stress-dependent resistance representation in rockfills and waste-rock materials. At the consequence level, validity requires screening-level assessment of high-end waste-dump mobility using documented geometry, basal-bed conditions, and mechanics-based interpretation of runout. These are the conditions under which the dissertation evidence is strongest and most internally consistent. (Arrieta and Zhang 2024, 2025, 2026).

The framework is particularly suited to engineering settings in which full-scale sieving is impractical, prototype-scale mechanical testing is limited, and consequence still has to be assessed on a defensible basis. Under those conditions, it supports a sequential analysis: quantify field state, represent pre-failure resistance for that state, and interpret how resistance loss may be expressed in mobility through pore pressure, basal resistance, path confinement, and basal-bed slope. This is the actual operational domain of the framework, not an abstract research space. It is the class of geotechnical problems for which the dissertation was built (Arrieta and Zhang 2024).

Within that domain, the framework is best suited to screening, comparative assessment, staged investigation, and hazard review rather than final predictive design. It is appropriate where the engineering objective is to connect field-scale evidence to pre-failure and post-failure interpretation without breaking the mechanics of the problem into disconnected specialist tasks. In practical terms, that includes reassessment of active waste dumps, comparison of sectors within large dumps, early-stage hazard evaluation, and consequence screening where the available data are heterogeneous but still sufficient to support a structured chain from state to consequence. This is the positive domain of validity of the framework, and the unresolved variables identified in the following sections must be judged against it (Arrieta and Zhang 2024, 2025, 2026).

8.2. Unresolved variables that still limit continuity across the state-resistance-consequence chain

The integrated framework remains operational but not yet fully predictive because several variables still limit continuity across the state-resistance-consequence chain. These are not secondary omissions. They determine how reliably measured field state can be transferred into pre-failure resistance representation and how reliably resistance loss can be transferred into consequence assessment. The unresolved variables cluster at three analytical levels, state, resistance, and consequence and, more importantly, across the boundaries between them (Arrieta and Zhang 2024, 2025, 2026).

At the state level, the unresolved variable is the relation between exposed surface state and mechanically relevant internal state. Section 4 showed that UAV photogrammetry can characterize PSD at realistic dump scale and preserve both between-dump contrast and within-dump variability. It did not establish how faithfully the visible surface represents the grading, segregation, fines content, or particle-shape distribution of the internal zones that may later control deformation or failure. In coarse mine waste dumps, where end-dumping, weathering, and slope-wise segregation generate strong vertical and lateral heterogeneity, that distinction is fundamental. The unresolved issue at this level is therefore not whether surface PSD can be measured. It is how reliably the measured surface state represents the internal state that governs mechanical response (Arrieta and Zhang 2024).

At the resistance level, the unresolved variables lie between the declared pre-shear state and the evolving resistance envelope. Section 5 showed that pre-shear PSD scaling provides a bounded curvature constraint within the adopted power-law calibration route and the admitted peak-state triaxial database. It did not resolve the variables that remain active once loading begins density state, fabric, loading path, particle breakage, and the evolution of gradation beyond peak state. In the present framework, curvature is assigned through the adopted $m = D/3$ closure, and the route is bounded to pre-shear PSDs, peak-state triaxial compression, and the admitted stress, PSD, and apparatus-size ranges. It therefore does not capture how the envelope evolves when breakage modifies contact structure, when loading departs from triaxial compression, or when the material moves into post-peak and residual response. The unresolved issue at this level is not whether pre-shear PSD matters. It is how much resistance evolution remains controlled by variables that are not contained in the pre-shear PSD descriptor alone (Arrieta and Zhang 2026).

At the consequence level, the unresolved variables are those that govern transient motion after failure initiation. Section 6 showed that pore-pressure ratio, basal resistance, path confinement, and basal-bed slope separate the observed mobility classes of the 46 documented failures. That is sufficient for screening-level consequence assessment. It does not resolve the time evolution of pore pressure during motion, the spatial variability of basal material along the full runout path, entrainment, internal deformation, or the evolution of dynamic resistance as flow depth and path geometry change. The frictionless reference comparator is also sensitive to path segmentation, timing resolution, and the adopted vertical drop. The unresolved issue at this level is therefore not whether the governing controls are known. It is how those controls evolve during the event rather than appearing only as event-level or back-calculated indicators after the fact (Arrieta and Zhang 2025).

The most important point is that these unresolved variables are not confined to individual Sections. They lie between the sections. The framework does not yet track the same material state continuously from exposed dump surface to active shear zone, to failed moving mass. That is the central unresolved continuity of the dissertation. Section 4 defines the state that can be measured. Section 5 defines the resistance that can be represented from that state. Section 6 defines the consequence once that resistance is reduced or lost. What remains unresolved is full material continuity across those stages. That is why the framework is operationally strong yet still short of direct predictive design use. Section 8.3 addresses that predictive boundary explicitly (Arrieta and Zhang 2024, 2025, 2026).

8.3. LIMITS ON DIRECT PREDICTIVE DESIGN USE OF THE INTEGRATED FRAMEWORK

Direct predictive design would require one continuous site-scale chain: the same dump sector, the same material definition, the same geometry, and the same evolving mechanical state carried from field characterization, through pre-failure resistance, into site-specific runout prediction. The dissertation does not yet provide that chain. It provides the analytical and mechanical structure of the chain. That is the exact reason the framework is already useful for structured hazard assessment while still stopping short of direct predictive design (Arrieta and Zhang 2024, 2025, 2026).

The first limitation is the definition of the design state itself. Section 4 characterizes the exposed surface state of the dump through UAV-derived PSD and related descriptors. That is a strong field result, and it is sufficient for screening and state definition at operational scale. It is not a full definition of the internal grading, density, segregation depth, moisture condition, or shear-zone state of the dump mass that would be required for direct predictive design. A design model must act on the material body that can fail, not only on the part of that body that can be observed from the surface. The framework therefore defines a measurable state, although not yet the complete design state of the failure mass (Arrieta and Zhang 2026).

The second limitation is the scope of the resistance model. Section 5 demonstrates that pre-shear PSD scaling can provide a bounded curvature constraint within the adopted stress-dependent power-law calibration route for rockfills and waste-rock materials. That result is mechanically important, although it remains bounded to pre-shear PSDs, peak-state triaxial compression, and the admitted stress, PSD, and apparatus-size ranges of the compiled database. Direct predictive design would require more than that. It would require a site-specific resistance formulation that can address the actual loading path, density state, breakage evolution, post-peak degradation, and the relevant mode of shearing in the dump. The dissertation does not claim that level of constitutive completeness, and it would be false to present Section 5 as if it already delivered it. The framework therefore improves the representation of pre-failure resistance, although it does not yet provide a full design model of resistance evolution (Arrieta and Zhang 2026).

The third limitation lies in the treatment of post-failure consequence. Section 6 identifies the controls that separate low, moderate, high, and extreme mobility and interprets those controls through pore pressure, basal friction, confinement, dynamic resistance, and a frictionless benchmark. That is sufficient for screening-level consequence assessment. It is not equivalent to a site-specific predictive runout model. Direct predictive design would require transient pore-pressure evolution, spatially resolved basal materials, calibrated entrainment, evolving path resistance, and geometry updated along the full travel corridor. Section 6 does not attempt that, and it should not be read as if it does. The benchmark comparison strengthens interpretation of consequence. It does not convert the framework into a predictive simulator (Arrieta and Zhang 2025).

The fourth limitation is the absence of numerical continuity across the failure boundary. The framework is integrated analytically, Section 4 defines the measurable state, Section 5 defines pre-failure resistance for that declared state, and Section 6 defines post-failure consequence once resistance is reduced or lost. Direct predictive design would require a single site-scale model that carries the same material definition, the same geometry, and the same evolving mechanical state through all three stages. That continuity is not yet present in the dissertation. The framework therefore supports a defensible engineering sequence of assessment, though not a single predictive design workflow from first measurement to final runout computation. This is the exact reason why the dissertation can already support structured hazard evaluation while still stopping short of direct predictive design use (Arrieta and Zhang 2024, 2025, 2026).

This limit is not a weakness in the thesis claim. It is the correct maturity statement of the framework. The dissertation provides a field-to-consequence assessment structure that is technically stronger than isolated characterization, isolated strength fitting, or isolated runout interpretation. What it does not yet provide is a direct predictive design system. The next section follows directly from that conclusion: it identifies the research needs that would convert the present framework into a stronger and more predictive engineering tool (Arrieta and Zhang 2024, 2025, 2026).

8.4. Priority research directions for strengthening predictive capacity of the integrated framework

The research directions that follow this dissertation are defined directly by the unresolved variables identified in Section 8.2 and by the predictive-design boundary stated in Section 8.3. They are sequential rather than parallel. The first priority is design-state definition. The second is extension of pre-failure resistance representation beyond the present pre-shear, peak-state scope. The third is advancement of consequence assessment from screening-level mechanics to site-specific predictive modeling. The fourth is integration of those levels through repeated monitoring and model updating. This order is necessary because predictive consequence assessment cannot be strengthened if the state and resistance definitions remain incomplete at the front end of the chain (Arrieta and Zhang 2024, 2025, 2026).

The first priority is resolution of the relation between exposed surface state and internal design state. Section 4 established that UAV photogrammetry can characterize PSD at realistic scale and can do so in large, unsafe, and inaccessible waste-dump settings. What remains unresolved is how accurately that observed surface represents the internal grading, segregation, fines distribution, and material transitions that later govern deformation and failure. Research at this stage requires coordinated programs in which UAV-based PSD characterization is linked to direct internal observations, controlled excavation exposures, or complementary survey methods where necessary. The field method itself can also be strengthened through improved calibration of oversized particles, higher-resolution imaging, and integrated sensing where one observation mode alone remains insufficient. Predictive design begins with design-state definition, and that definition is not yet complete if exposed-surface characterization remains the only source of state information (Arrieta and Zhang 2024).

The second priority is extension of the resistance framework from pre-shear, peak-state envelopes to the broader resistance evolution experienced by real waste dumps. Section 5 showed that pre-shear PSD scaling can provide a bounded curvature constraint within the adopted stress-dependent power-law calibration route. What remains unresolved is how that constrained curvature evolves once loading induces breakage, density change, fabric change, and gradation evolution. Research at this stage requires datasets that include not only pre-shear PSD, but also post-shear PSD, density evolution, and comparable loading histories within one experimental framework. It also requires extension beyond peak-state triaxial compression to direct shear, post-peak degradation, residual-state response, and cyclic loading where those mechanisms are relevant. Without that extension, the framework can represent pre-failure resistance more rigorously, but it cannot yet represent the full resistance path of the material through failure (Arrieta and Zhang 2026).

The third priority is advancement of the consequence framework from screening-level interpretation to site-specific predictive modeling. Section 6 identified the variables that separate low, moderate, high, and extreme mobility and interpreted them through pore pressure, basal resistance, path confinement, dynamic resistance, and a frictionless reference comparator. What remains unresolved is the evolution of those variables during motion rather than their appearance as event-level or back-calculated indicators. Research at this stage requires instrumented case histories, monitored pore-pressure response, stronger characterization of basal materials along the runout path, and coupled hydro-mechanical or DEM/FEM modeling calibrated to site geometry and evolving resistance. It also requires stronger statistical separation of the mobility variables, including partial-rank or regression-based frameworks that isolate the effect of each indicator under covariation. Without that development, the framework remains strong for consequence screening and incomplete for direct runout prediction at individual sites (Arrieta and Zhang 2025).

The fourth priority is conversion of the framework from one-time analytical assessment to time-updated hazard evaluation. At present, the dissertation integrates state, resistance, and consequence analytically. The next engineering development is repeated updating of those levels as the dump evolves. In practical terms, this requires repeated UAV-based surface characterization, integration of pore-pressure and displacement monitoring, and staged reassessment of both stability and consequence as new information becomes available. This is the stage at which the present field-to-consequence framework would become monitored and adaptive rather than static. That extension is essential for active mine environments, where dump geometry, exposed surface state, and hydrological conditions change during operation (Arrieta and Zhang 2024, 2025, 2026).

Taken together, these priorities define the shortest technically defensible sequence for strengthening predictive capacity. First, strengthen design-state definition. Second, extend resistance representation. Third, advance consequence modeling. Fourth, connect the full chain through monitoring and updating. A different order would leave the predictive structure mechanically incomplete. Section 8 therefore closes with a defined research sequence rather than a generic future-work list (Arrieta and Zhang 2024, 2025, 2026). Table 18 summarizes these priority research directions and the corresponding evidence required to strengthen the predictive capacity of the integrated framework.

Table 18. Priority research directions for strengthening predictive capacity of the integrated framework.

Priority	Research need	Main unresolved variable	Required evidence or method	Expected gain
1	Internal state definition beyond exposed surface	Surface state versus internal grading and segregation	Combined UAV characterization with direct internal observations and complementary survey methods	Stronger design-state definition
2	Resistance evolution beyond pre-shear peak-state scope	Breakage, density evolution, post-shear PSD, loading-path effects	Controlled mechanical datasets with pre- and post-shear characterization	Stronger pre-failure resistance modeling
3	Site-specific consequence prediction	Transient pore pressure, basal-material variability, evolving path resistance	Instrumented case histories and coupled DEM/FEM modeling	Stronger runout prediction
4	Time-updated hazard reassessment	Temporal change in state, resistance, and hydrology	Repeated UAV surveys, monitoring, and staged model updating	Adaptive operational risk management

9. Conclusions

Section 9 answers the four research questions in the same order in which they were defined in Section 1 and bounded in Section 3.2. It is kept separate from Section 8 because Section 8 defines operating limits and research needs, whereas Section 9 states the final answers to the research questions and the final thesis conclusion. Each section states the final answer, the evidence on which that answer rests, and the valid scope of the claim. The section then closes with one final thesis conclusion (Arrieta and Zhang 2024, 2025, 2026).

9.1. Answer to RQ1: Field-scale characterization of material state

RQ1 asked how the gradation of coarse mine waste dumps can be characterized reliably at operational field scale. The dissertation answers this directly in Section 4. Exposed-surface gradation can be characterized at operational scale through UAV photogrammetry, Structure-from-Motion reconstruction, and spatially resolved PSD extraction. In the five waste dumps studied, the method reproduced field particle size with errors below 10%, preserved both between-dump contrast and within-dump variability, and converted dump surfaces from visual description into quantified material-state information. Within the evidence base of Section 4, PSD is therefore established as a defensible field-scale descriptor of material state in coarse mine waste dumps (Arrieta and Zhang 2024).

The answer is bounded exactly as required by Section 3.2. Section 4 characterizes exposed surface state, not the full internal grading of the dump mass, and translates measured PSD into first-order geotechnical screening rather than constitutive proof of shear behavior. Within that scope, RQ1 is fully answered: measurable field state can be established through dump-scale PSD characterization and carried forward into geotechnical analysis (Arrieta and Zhang 2024).

9.2. Answer to RQ2: Pre-failure resistance representation

RQ2 asked how pre-shear gradation information can be used to constrain nonlinear stress-dependent shear-strength representation. The dissertation answers this directly in Section 5. Within the admitted peak-state triaxial database, pre-shear PSD scaling can be used as a bounded curvature constraint within the adopted stress-dependent power-law calibration route. Curvature is assigned through the adopted $m = D/3$ closure, and only the anchor strength level is calibrated from peak-state triaxial response. Across 42 studies, 1005 triaxial data points, and 181 PSD-defined cases, the PSD-constrained route remained close to fitted-curvature practice in curvature space and reduced route-to-observed response discrepancy under the adopted route-comparison protocol. Median MAE decreased from 0.24 to 0.06 MPa, median RMSE from 0.26 to 0.07 MPa, and median Bias from 0.24 to 0.06 MPa (Arrieta and Zhang 2026).

The answer is bounded exactly as required by Section 3.2. Section 5 does not establish a universal constitutive exponent law, a unique PSD-to-curvature law, external predictive validation, or scale-independent validation. Its valid scope is restricted to pre-shear PSDs, peak-state triaxial compression, and the admitted stress, PSD, and apparatus-size ranges of the compiled database. Within that scope, RQ2 is fully answered: pre-shear PSD scaling provides a bounded curvature constraint for the adopted power-law calibration route and supports a more disciplined representation of pre-failure resistance than free curvature fitting alone (Arrieta and Zhang 2026).

9.3. Answer to RQ3: Post-failure consequence and flow-slide mobility

RQ3 asked how pore pressure, basal resistance, dynamic resistance, and path geometry govern flow-slide mobility once resistance is reduced or lost. The dissertation answers this directly in Section 6. At screening level, mobility in high-end waste dumps is governed by a coupled mechanics field defined by pore-pressure ratio r_u, basal friction coefficient f, path confinement a, basal-bed slope δ, and velocity-dependent resistance. In the 46 documented failures analyzed, high and extreme mobility concentrate where r_u exceeds about 0.4, f commonly falls below about 0.15, confinement is strong, and δ lies mainly within a mobility window of about $15°$ to $30°$. Within that field, pore pressure acts as the driver, confinement as the amplifier, and basal-bed slope as the limiter (Arrieta and Zhang 2025).

Section 6 also resolved RQ3 dynamically rather than geometrically only. The Voellmy-type framework showed that rapid consequence is governed by both frictional and velocity-dependent resistance, and the Brachistochrone reference comparator showed that the most mobile events commonly reached about 60-90% of the frictionless reference velocity. The answer is bounded exactly as required by Section 3.2. Section 6 does not provide a site-specific hydro-mechanical predictive model; it provides a screening-level mechanics framework based on documented failures, back-calculated controls, and a frictionless reference used cautiously as a comparator. Within that scope, RQ3 is fully answered (Arrieta and Zhang 2025).

9.4. Answer to RQ4: Integrated field-to-consequence workflow for coarse mine waste assessment

RQ4 asked how the elements of the dissertation can be integrated into a defensible engineering workflow for coarse mine waste assessment. The dissertation answers this through the combined results of Sections 4 to 7. The workflow is obtained by treating coarse mine waste assessment as a field-to-consequence sequence in which field-scale PSD defines measurable material state, pre-shear PSD scaling provides a bounded curvature constraint within pre-failure resistance representation, and resistance loss frames post-failure consequence through mobility mechanics. The answer is therefore direct: a defensible workflow is achieved by linking characterization, resistance representation, and consequence assessment in one bounded analytical sequence rather than treating them as disconnected tasks (Arrieta and Zhang 2024, 2025, 2026).

The answer is bounded exactly as required by Section 3.2. The dissertation does not provide one end-to-end numerical simulator from UAV-derived PSD to runout prediction and does not claim a universal constitutive law for granular mine waste. It provides a bounded engineering workflow in which measurable field state is carried into pre-failure resistance representation and resistance loss is carried into post-failure consequence assessment. Within the scope of coarse mine waste dumps, RQ4 is fully answered (Arrieta and Zhang 2024, 2025, 2026).

9.5. FINAL CONCLUSIONS

This dissertation demonstrates that coarse mine waste hazard can be assessed through an integrated geotechnical framework in which measured PSD defines material state, pre-shear PSD scaling provides a bounded curvature constraint within pre-failure resistance representation, and resistance loss governs post-failure consequence through identifiable mobility controls. That is the final thesis conclusion.

The contribution of the dissertation is not a universal constitutive law and not a single end-to-end numerical simulator. It is the closure of a practical and scientific discontinuity in current mine waste assessment by connecting measurable field state, pre-failure resistance representation, and post-failure consequence assessment within one bounded field-to-consequence framework for coarse mine waste dumps (Arrieta and Zhang 2024, 2025, 2026).

10. References

Aaron J, McDougall S (2019) Rock avalanche mobility: The role of path material. Eng Geol 257:105126. https://doi.org/10.1016/j.enggeo.2019.05.003

Abellan A, Derron M-H, Jaboyedoff M (2016) "Use of 3D Point Clouds in Geohazards" Special Issue: Current Challenges and Future Trends. Remote Sens (Basel) 8:130. https://doi.org/10.3390/rs8020130

Ali U, Kikumoto M (2025) Role of particle shape in sheared granular media: roundness and elongation. Powder Technol 449:120436. https://doi.org/10.1016/j.powtec.2024.120436

Arrieta M, Zhang Z-X (2024) Particle size distribution (PSD) estimation using unmanned aerial vehicle (UAV) photogrammetry for rockfill shear strength characterization. Acta Geotech 19:6239–6258. https://doi.org/10.1007/s11440-024-02315-x

Arrieta M, Zhang Z-X (2025) Minimum-Time Path (Brachistochrone) Analysis for Extreme Flow Slide Mobility in High-End Waste Dumps: Integrating Pore Pressure and Dynamic Rheology. Rock Mech Rock Eng. https://doi.org/10.1007/s00603-025-05009-2

Arrieta M, Zhang Z-X (2026) Stress-dependent shear strength of rockfills and waste-rock materials with curvature constrained by particle size distribution scaling. Appended manuscript.

Bar N, Kostadinovski M, Tucker M, et al (2020) Rapid and robust slope failure appraisal using aerial photogrammetry and 3D slope stability models. Int J Min Sci Technol 30:651–658. https://doi.org/10.1016/j.ijmst.2020.05.013

Barton N (2013) Shear strength criteria for rock, rock joints, rockfill and rock masses: Problems and some solutions. Journal of Rock Mechanics and Geotechnical Engineering 5:249–261. https://doi.org/10.1016/j.jrmge.2013.05.008

Barton N (2016) Non-linear shear strength for rock, rock joints, rockfill and interfaces. Innovative Infrastructure Solutions 1:30. https://doi.org/10.1007/s41062-016-0011-1

Barton N, Kjaernsli B (1981) Shear Strength of Rockfill. Journal of the Geotechnical Engineering Division 107:873–891. https://doi.org/10.1061/AJGEB6.0001167

Bathurst JC, Burton A, Ward TJ (1997) Debris Flow Run-Out and Landslide Sediment Delivery Model Tests. Journal of Hydraulic Engineering 123:410–419. https://doi.org/10.1061/(ASCE)0733-9429(1997)123:5(410)

Beemer RD, Li L, Leonti A, et al (2022) Comparison of 2D Optical Imaging and 3D Microtomography Shape Measurements of a Coastal Bioclastic Calcareous Sand. J Imaging 8:72. https://doi.org/10.3390/jimaging8030072

Benda LE, Cundy TW (1990) Predicting deposition of debris flows in mountain channels. Canadian Geotechnical Journal 27:409–417. https://doi.org/10.1139/t90-057

Bishop AW (1959) The Principle of Effective Stress. Teknisk Ukeblad 39:859–863

Bishop AW (1973) The stability of tips and spoil heaps. Quarterly Journal of Engineering Geology 6:335–376. https://doi.org/10.1144/GSL.QJEG.1973.006.03.15

Bittelli M, Campbell GS, Flury M (1999) Characterization of Particle-Size Distribution in Soils with a Fragmentation Model. Soil Science Society of America Journal 63:782–788. https://doi.org/10.2136/sssaj1999.634782x

Borenäs K, Lundberg P (1986) Rotating hydraulics of flow in a parabolic channel. J Fluid Mech 167:309. https://doi.org/10.1017/S0022112086002835

Breitenbach J (2012) Definition of Rockfill versus Earthfill Material. Journal of Indian Committee on Large Dams 1:8–12

Carrasco S, Cantor D, Ovalle C (2022) Effects of particle size-shape correlations on steady shear strength of granular materials: The case of particle elongation. Int J Numer Anal Methods Geomech 46:979–1000. https://doi.org/10.1002/nag.3329

Carrasco S, Cantor D, Ovalle C, Quiroz-Rojo P (2023) Shear strength of angular granular materials with size and shape polydispersity. Open Geomechanics 4:1. https://doi.org/10.5802/ogeo.15

Charles JA (1990) Laboratory Shear Strength Tests and the Stability of Rockfill Slopes. In: Advances in Rockfill Structures. Springer Netherlands, Dordrecht, pp 53–72

Charles JA, Watts KS (1980) The influence of confining pressure on the shear strength of compacted rockfill. Géotechnique 30:353–367. https://doi.org/10.1680/geot.1980.30.4.353

Clauset A, Shalizi CR, Newman MEJ (2009) Power-Law Distributions in Empirical Data. SIAM Review 51:661–703. https://doi.org/10.1137/070710111

Colomina I, Molina P (2014) Unmanned aerial systems for photogrammetry and remote sensing: A review. ISPRS Journal of Photogrammetry and Remote Sensing 92:79–97. https://doi.org/10.1016/j.isprsjprs.2014.02.013

Contreras L-F, Linero-Molina S, Dixon J (2022) Bayesian Approach To Improve The Confidence Of The Estimation Of The Shear Strength Of Coarse Mine Waste Using Barton's Empirical Criterion. Australian Geomechanics Journal. https://doi.org/10.56295/AGJ5728

Corominas J (1996) The angle of reach as a mobility index for small and large landslides. Canadian Geotechnical Journal 33:260–271. https://doi.org/10.1139/t96-005

Cylwik SD, Arrieta M, Cunning JC, Hawley PM (2025a) Update to the Leps Strength Envelopes for Rockfill Based on 900 Large-Scale Triaxial Tests. International Journal of Geomechanics 25:. https://doi.org/10.1061/IJGNAI.GMENG-12050

Cylwik SD, Arrieta M, Cunning JC, Hawley PM (2025b) Update to the Leps Strength Envelopes for Rockfill Based on 900 Large-Scale Triaxial Tests. International Journal of Geomechanics 25:. https://doi.org/10.1061/IJGNAI.GMENG-12050

Dawson RF (1994) Mine waste geotechnics. PhD , University of Alberta

Dawson RF, Morgenstern NR, Stokes AW (1998) Liquefaction flowslides in Rocky Mountain coal mine waste dumps. Canadian Geotechnical Journal 35:328–343. https://doi.org/10.1139/t98-009

De Mello VFB (1977) Reflections on design decisions of practical significance to embankment dams. Géotechnique 27:281–355. https://doi.org/10.1680/geot.1977.27.3.281

Deiminiat A, Li L (2022) Experimental Study on the Reliability of Scaling Down Techniques Used in Direct Shear Tests to Determine the Shear Strength of Rockfill and Waste Rocks. CivilEng 3:35–50. https://doi.org/10.3390/civileng3010003

Deiminiat A, Li L, Zeng F, et al (2020) Determination of the Shear Strength of Rockfill from Small-Scale Laboratory Shear Tests: A Critical Review. Advances in Civil Engineering 2020:1–18. https://doi.org/10.1155/2020/8890237

Duncan JM, Chang C-Y (1970) Nonlinear Analysis of Stress and Strain in Soils. Journal of the Soil Mechanics and Foundations Division 96:1629–1653. https://doi.org/10.1061/JSFEAQ.0001458

Erlichson H (1999) Johann Bernoulli's brachistochrone solution using Fermat's principle of least time. Eur J Phys 20:299–304. https://doi.org/10.1088/0143-0807/20/5/301

Frossard E, Hu W, Dano C, Hicher P-Y (2012) Rockfill shear strength evaluation: a rational method based on size effects. Géotechnique 62:415–427. https://doi.org/10.1680/geot.10.P.079

Gao S, Zhou W, Shi X, et al (2017) Mechanical properties of material in a mine dump at the Shengli #1 Surface Coal Mine, China. Int J Min Sci Technol 27:545–550. https://doi.org/10.1016/j.ijmst.2017.03.014

Golder Associates (1991) Runout characteristics of debris from dump failures in mountainous terrain - Stage 1. Data collection. British Columbia Mine Waste Rock Pile Research Committee

Golder Associates (1992) Study of Runout of Failed Mined Waste Dumps in Mountainous Terrain

Golder Associates, Hungr O (1995) Runout characteristics of debris from dump failures in mountainous terrain - Stage 2. Analysis, modelling and prediction. Interim report. British Columbia Mine Waste Rock Pile Research Committee

Gonzalez A (1985) Rockfill strength with dimensionless parameters. . In: Proceedings of the Eleventh International Conference on Soil Mechanics and Foundation Engineering. San Francisco, pp 479–485

Hawley M, Cunning J (2017) Guidelines for Mine Waste Dump and Stockpile Design. CSIRO, pp 79–98

Heim A (1932) Landslides & Human Lives (Bergsturz und Menschenleben). BiTech Publishers, Vancouver, BC, Canada

Hryciw RD, Zheng J, Shetler K (2016) Particle Roundness and Sphericity from Images of Assemblies by Chart Estimates and Computer Methods. Journal of Geotechnical and Geoenvironmental Engineering 142:. https://doi.org/10.1061/(ASCE)GT.1943-5606.0001485

Hungr O (1995) A model for the runout analysis of rapid flow slides, debris flows, and avalanches. Canadian Geotechnical Journal 32:610–623. https://doi.org/10.1139/t95-063

Hungr O, Dawson RF, Kent A, et al (2002) Rapid flow slides of coal-mine waste in British Columbia, Canada. pp 191–208

Hungr O, Evans SG (2004) Entrainment of debris in rock avalanches: An analysis of a long run-out mechanism. GSA Bulletin 116:1240–1252. https://doi.org/10.1130/B25362.1

Hungr O, McDougall S (2009) Two numerical models for landslide dynamic analysis. Comput Geosci 35:978–992. https://doi.org/10.1016/j.cageo.2007.12.003

Indraratna B (1994) The effect of normal stress-friction angle relationship on the stability analysis of a rockfill dam. Geotechnical & Geological Engineering 12:113–121. https://doi.org/10.1007/BF00429769

Indraratna B, Ionescu D, Christie HD (1998) Shear Behavior of Railway Ballast Based on Large-Scale Triaxial Tests. Journal of Geotechnical and Geoenvironmental Engineering 124:439–449. https://doi.org/10.1061/(ASCE)1090-0241(1998)124:5(439)

Indraratna B, Wijewardena LSS, Balasubramaniam AS (1993) Large-scale triaxial testing of grey wacke rockfill. Géotechnique 43:37–51. https://doi.org/10.1680/geot.1993.43.1.37

Kemeny J (1994) Practical technique for determining the size distribution of blasted benches, waste dumps and heap leach sites. Min Eng 46:1281–1284

Kent PE (1966) The Transport Mechanism in Catastrophic Rock Falls. J Geol 74:79–83. https://doi.org/10.1086/627142

Kong D, Saroglou C, Wu F, et al (2021) Development and application of UAV-SfM photogrammetry for quantitative characterization of rock mass discontinuities. International Journal of Rock Mechanics and Mining Sciences 141:104729. https://doi.org/10.1016/j.ijrmms.2021.104729

Legros F (2002) The mobility of long-runout landslides. Eng Geol 63:301–331. https://doi.org/10.1016/S0013-7952(01)00090-4

Leps TM (1970) Review of Shearing Strength of Rockfill. Journal of the Soil Mechanics and Foundations Division 96:1159–1170. https://doi.org/10.1061/JSFEAQ.0001433

Li G, Liu Y-J, Dano C, Hicher P-Y (2015) Grading-Dependent Behavior of Granular Materials: From Discrete to Continuous Modeling. J Eng Mech 141:. https://doi.org/10.1061/(ASCE)EM.1943-7889.0000866

Linero Molina S, Contreras LF, Dixon J (2021) Estimation of shear strength of very coarse mine waste. In: SSIM 2021: Second International Slope Stability in Mining. Australian Centre for Geomechanics, Perth, pp 341–354

Marsal RJ (1967) Large Scale Testing of Rockfill Materials. Journal of the Soil Mechanics and Foundations Division 93:27–43. https://doi.org/10.1061/JSFEAQ.0000958

Marschi ND, Chan CK, Seed HB (1972) Evaluation of Properties of Rockfill Materials. Journal of the Soil Mechanics and Foundations Division 98:95–114. https://doi.org/10.1061/JSFEAQ.0001735

McDougall S (2017) 2014 Canadian Geotechnical Colloquium: Landslide runout analysis — current practice and challenges. Canadian Geotechnical Journal 54:605–620. https://doi.org/10.1139/cgj-2016-0104

Newland PL, Allely BH (1957) Volume Changes in Drained Triaxial Tests on Granular Materials. Géotechnique 7:17–34. https://doi.org/10.1680/geot.1957.7.1.17

Nicoletti PG, Sorriso-Valvo M (1991) Geomorphic controls of the shape and mobility of rock avalanches. Geol Soc Am Bull 103:1365–1373. https://doi.org/10.1130/0016-7606(1991)103<1365:GCOTSA>2.3.CO;2

Ovalle C, Dano C (2020) Effects of particle size–strength and size–shape correlations on parallel grading scaling. Géotechnique Letters 10:191–197. https://doi.org/10.1680/jgele.19.00095

Ovalle C, Frossard E, Dano C, et al (2014) The effect of size on the strength of coarse rock aggregates and large rockfill samples through experimental data. Acta Mech 225:2199–2216. https://doi.org/10.1007/s00707-014-1127-z

Perla R, Cheng TT, McClung DM (1980) A Two Parameter Model of Snow Avalanche Motion. Journal of Glaciology 26:197–207. https://doi.org/10.3189/S002214300001073X

Qiu P, Pabst T (2023) Characterization of particle size segregation and heterogeneity along the slopes of a waste rock pile using image analysis. Environ Earth Sci 82:573. https://doi.org/10.1007/s12665-023-11229-y

Sanchidrián JA, Segarra P, López LM (2006) A Practical Procedure for the Measurement of Fragmentation by Blasting by Image Analysis. Rock Mech Rock Eng 39:359–382. https://doi.org/10.1007/s00603-005-0073-4

Sanchidrián JA, Segarra P, Ouchterlony F, López LM (2009) On the accuracy of fragment size measurement by image analysis in combination with some distribution functions. Rock Mech Rock Eng 42:95–116. https://doi.org/10.1007/s00603-007-0161-8

Sassa Kyoji and Wang G hui (2005) Mechanism of landslide-triggered debris flows: Liquefaction phenomena due to the undrained loading of torrent deposits. In: Debris-flow Hazards and Related Phenomena. Springer Berlin Heidelberg, Berlin, Heidelberg, pp 81–104

Scheidegger AE (1973) On the prediction of the reach and velocity of catastrophic landslides. Rock Mech Rock Eng 5:231–236. https://doi.org/10.1007/BF01301796

Shin H, Santamarina JC (2013) Role of Particle Angularity on the Mechanical Behavior of Granular Mixtures. Journal of Geotechnical and Geoenvironmental Engineering 139:353–355. https://doi.org/10.1061/(ASCE)GT.1943-5606.0000768

Tang ZC, Jiao YY, Wong LNY, Wang XC (2016) Choosing Appropriate Parameters for Developing Empirical Shear Strength Criterion of Rock Joint: Review and New Insights. Rock Mech Rock Eng 49:4479–4490. https://doi.org/10.1007/s00603-016-1014-0

Turcotte DL (1986) Fractals and fragmentation. J Geophys Res 91:1921. https://doi.org/10.1029/JB091iB02p01921

Valenzuela L, Bard E, Campana J, Anabalon M (2008) High Waste Rock Dumps — Challenges and Developments. In: Proceedings of the First International Seminar on the Management of Rock Dumps, Stockpiles and Heap Leach Pads. Australian Centre for Geomechanics, Perth, pp 65–78

Voellmy A (1955) Uber die Zerstorungskraft von Lawinen. Bauzeitung 73:159–165

Westoby MJ, Brasington J, Glasser NF, et al (2012) 'Structure-from-Motion' photogrammetry: A low-cost, effective tool for geoscience applications. Geomorphology 179:300–314. https://doi.org/10.1016/j.geomorph.2012.08.021

Xu Y (2018) Shear strength of granular materials based on fractal fragmentation of particles. Powder Technol 333:1–8. https://doi.org/10.1016/j.powtec.2018.03.001

Xu Y, Feng X, Zhu H, Chu F (2015) Fractal model for rockfill shear strength based on particle fragmentation. Granul Matter 17:753–761. https://doi.org/10.1007/s10035-015-0591-z

Xu Y, Xu Y (2021) Numerical simulation of direct shear test of rockfill based on particle breaking. Acta Geotech 16:3133–3144. https://doi.org/10.1007/s11440-021-01172-2

Yan WM, Dong J (2011) Effect of Particle Grading on the Response of an Idealized Granular Assemblage. International Journal of Geomechanics 11:276–285. https://doi.org/10.1061/(ASCE)GM.1943-5622.0000085

Yang G, Jiang Y, Nimbalkar S, et al (2019) Influence of Particle Size Distribution on the Critical State of Rockfill. Advances in Civil Engineering 2019:1–7. https://doi.org/10.1155/2019/8963971

Yu H, Ng K, Grana D, et al (2020) A generalized power-law criterion for rocks based on Mohr failure theory. International Journal of Rock Mechanics and Mining Sciences 128:104274. https://doi.org/10.1016/j.ijrmms.2020.104274

ORIGINAL PAPERS

RES TERRAE
Publications in Geosciences, University of Oulu, Oulun yliopiston geotieteiden julkaisuja.
Ser. A, Contributions.

Ser. A ISSN 0358-2477 (print)
Ser. A ISSN 2489-7957 (online)
Ser. A, No. 54 ISBN 978-952-62-5024-3 (print)
Ser. A, No. 54 ISBN 978-952-62-5025-0 (online)